

MEASUREMENT OF ISOBARIC ANALOGUE RESONANCES OF ^{47}Ar
WITH THE ACTIVE-TARGET TIME PROJECTION CHAMBER

By

Joshua William Bradt

A DISSERTATION

Submitted to
Michigan State University
in partial fulfillment of the requirements
for the degree of

Physics – Doctor of Philosophy

2017

ABSTRACT

MEASUREMENT OF ISOBARIC ANALOGUE RESONANCES OF ^{47}Ar WITH THE ACTIVE-TARGET TIME PROJECTION CHAMBER

By

Joshua William Bradt

While the nuclear shell model accurately describes the structure of nuclei near stability, the structure of unstable, neutron-rich nuclei is still an area of active research. One region of interest is the set of nuclei near $N = 28$. The shell model suggests that these nuclei should be approximately spherical due to the shell gap predicted by their magic number of neutrons; however, experiments have shown that the nuclei in this region rapidly become deformed as protons are removed from the spherical ^{48}Ca . This makes ^{46}Ar a particularly interesting system as it lies in a transition region between ^{48}Ca and lighter isotones that are known to be deformed.

An experiment was performed at the National Superconducting Cyclotron Laboratory (NSCL) to measure resonant proton scattering on ^{46}Ar . The resonances observed in this reaction correspond to unbound levels in the ^{47}K intermediate state nucleus which are isobaric analogues of states in the ^{47}Ar nucleus. By measuring the spectroscopic factors of these states in ^{47}Ar , we gain information about the single-particle structure of this system, which is directly related to the size of the $N = 28$ shell gap. Four resonances were observed: one corresponding to the ground state in ^{47}Ar , one corresponding to its first excited $1/2^-$ state, and two corresponding to $1/2^+$ states in either ^{47}Ar or the intermediate state nucleus. However, only a limited amount of information about these states could be recovered due to the low experimental statistics and limited angular resolution caused by pileup rejection and the inability to accurately reconstruct the beam particle track.

In addition to the nuclear physics motivations, this experiment served as the radioactive beam commissioning for the Active-Target Time Projection Chamber (AT-TPC). The AT-TPC is a new gas-filled charged particle detector built at the NSCL to measure low-energy radioactive beams from the ReA3 facility. Since the gas inside the detector serves as both the tracking medium and the scattering target, reactions are measured over a continuous range of energies with near- 4π solid angle coverage. This experiment demonstrated that tracks recorded by the AT-TPC can be reconstructed to a good resolution, and it established the feasibility of performing similar experiments with this detector in the future.

ACKNOWLEDGEMENTS

Although claiming that this work did not occur in a vacuum would be, at best, abuse of a metaphor, it is certainly true that I could not have completed this thesis, let alone the years of work that came before it, without the help of many others. First and foremost, I'd like to thank my advisor, Daniel Bazin, for his endless patience and encouragement, and for giving me the freedom to experiment and solve problems in my own way. Additionally, I am grateful to the entire AT-TPC group, which has made me feel welcome from my first day; I truly could not have asked for a better group of people to work with. In particular, I'd like to thank Wolfgang Mittig, Yassid Ayyad, and Michelle Kuchera for their help, feedback, and advice throughout what sometimes seemed like a long and hopeless analysis process.

It would quite literally be impossible to finish graduate school without the help of my guidance committee, so I would like to thank Daniel Bazin, Morten Hjorth-Jensen, Wolfgang Mittig, Kirsten Tollefson, and Remco Zegers for their advice and for taking the time out of their busy schedules to serve on my committee. Additionally, I'd like to thank the staff of the NSCL for their role in this experiment, and the MSU Institute for Cyber-Enabled Research for providing computing resources and technical support.

This whole experience would have been a lot more difficult and certainly a lot less fun without the kind, supportive, and welcoming body of graduate students at MSU. I will truly miss all of you, but there are a few people in particular that I'd like to mention. I'd like to thank Wei Jia Ong for conversations both deep and superficial, for many cups of coffee, and for tolerating my puns. Also, thanks to Amy Lovell for commiserating about Michigan drivers, providing baking advice, and playing no small part in me passing my subject exams. I'd like to thank my officemates for tolerating the choice words I've addressed to my computer many times in the last four years, and particularly I am grateful to Chris Izzo and Charlie Loelius for many intriguing conversations about everything from pop culture to politics to geography. Finally, I must thank the other graduate students from the AT-TPC group, including Lisa Carpenter and Nate Watwood, for their company and for keeping me sane through long meetings and even longer shifts.

Last but certainly not least, I thank my parents for their endless love and support throughout my life, for encouraging me to always do my best, and for helping me keep things in perspective when I struggled. I know that wherever life takes me from here, I will always be able to count on your support, and that means more than I could ever put into words.

TABLE OF CONTENTS

LIST OF TABLES	vii
LIST OF FIGURES	ix
LIST OF ALGORITHMS	xviii
CHAPTER 1 INTRODUCTION	1
1.1 Nuclear physics background	1
1.1.1 Magic numbers and the nuclear shell model	1
1.1.2 Single-particle states	2
1.1.3 Isobaric analogue states	4
1.1.4 Elastic scattering in quantum mechanics	5
1.1.5 The optical potential	6
1.1.6 Resonances and the R matrix theory	7
1.1.7 Isobaric analogue resonances	9
1.1.8 Calculating the resonance energy	11
1.2 Experimental motivation	11
1.2.1 The disappearing $N = 28$ shell gap	11
1.2.2 Previous studies of ^{47}Ar	13
1.2.3 Resonant proton scattering in inverse kinematics	16
1.2.4 Commissioning of the AT-TPC	17
1.3 Summary	18
CHAPTER 2 THE ACTIVE-TARGET TIME PROJECTION CHAMBER	19
2.1 Background	19
2.1.1 Time projection chambers	19
2.1.2 Active targets	20
2.2 Structure of the AT-TPC	21
2.2.1 Inner and outer gas volumes	21
2.2.2 Electric and magnetic fields	22
2.2.3 Sensor plane	23
2.3 Tilting the detector	25
2.4 Electronics	26
2.5 Data acquisition	27
2.5.1 Structure of the DAQ system	27
CHAPTER 3 ANALYZING AT-TPC DATA	31
3.1 Baseline correction	31
3.2 Track reconstruction	32
3.3 Noise removal	35
3.3.1 Hough transform for lines	35
3.3.2 Hough transform for circles	38
3.3.3 Removing correlated noise	39
3.3.4 Removing uncorrelated noise	40
3.4 Modeling tracks and fits	43

3.4.1	Track representation and generation	43
3.4.2	Simulated diffusion and track projection	44
3.4.3	The objective function	45
3.4.4	Finding initial parameter values for optimization	46
3.5	The Monte Carlo optimizer	47
3.5.1	Description of algorithm	47
3.5.2	Checking convergence	48
3.6	Alternative fitting algorithms	49
3.6.1	Gradient-based methods	50
3.6.2	Compass search	51
3.6.3	Nelder-Mead simplex algorithm	52
3.6.4	Simulated annealing	53
3.6.5	Neural networks	54
3.6.6	Kalman filter	55
3.7	Vertex energy reconstruction	55
3.7.1	Using the vertex position	56
3.7.2	Using kinematics	56
CHAPTER 4	SIMULATIONS	58
4.1	Overview of the simulation process	58
4.1.1	Parameter generation	58
4.1.1.1	Uniform distribution	59
4.1.1.2	Simulated scattering distribution	61
4.1.2	Tracking and event generation	64
4.1.3	Simulating the trigger	65
4.1.3.1	Generating channel-level trigger signals	66
4.1.3.2	Generating CoBo-level multiplicity signals	67
4.1.3.3	Generating global triggers	68
4.1.4	Cleaning and minimization	68
4.1.5	Post-processing and cuts	68
4.2	Simulated acceptance	69
4.3	Simulated resolution	86
4.4	R matrix simulation	89
CHAPTER 5	EXPERIMENT	93
5.1	Beam production	93
5.2	Detection setup	96
5.2.1	AT-TPC setup	96
5.2.2	Ion chamber and secondary DAQ	97
5.2.3	Trigger	98
5.2.4	Excluding beam events	99
5.3	Analysis and results	99
5.3.1	Correlating VME and GET events	99
5.3.2	Merging GET data files	102
5.3.3	Beam particle identification	103
5.3.4	Noise removal	104
5.3.5	Beam tracks	105
5.3.6	Track fitting	105

5.3.7	Proton parameter distributions	107
5.3.8	Vertex energy reconstructions	107
5.3.9	Cross sections and excitation functions	117
5.3.10	Alternative analysis method	121
5.3.11	Results	126
5.3.12	Statistical testing	130
5.4	Discussion	131
5.4.1	Comparison to previous measurements	131
5.4.2	Statistical significance	134
CHAPTER 6	CONCLUSION	136
6.1	Summary	136
6.2	Future outlook	137
BIBLIOGRAPHY	139

LIST OF TABLES

Table 1.1: First few levels in ^{47}Ar identified by Gaudefroy et al. [16, Table 1].	14
Table 3.1: Monte Carlo fit parameters I , T , and R and initial parameter space widths σ used in the $^{46}\text{Ar}(\text{p}, \text{p}')$ measurement.	49
Table 4.1: Expected resonance properties calculated from the results of Gaudefroy et al. [18] using the procedure from Section 1.1.8. The resonance energy E_R is given in MeV, and the resonance width Γ_p , as calculated by DSIGMAIV, is given in keV. L is the orbital angular momentum, J is the total angular momentum, Π is the parity, and S is the spectroscopic factor.	62
Table 4.2: Global optical model [29] parameters used in the simulation. V_r , R_r , and a_r are the depth, radius, and diffuseness parameters for a real-valued Woods-Saxon potential, while V_i , R_i , and a_i are the corresponding parameters for an imaginary Woods-Saxon potential. The depth is given in MeV, and the radius and diffuseness are given in fm. The Coulomb radius used was 1.27 fm.	62
Table 4.3: Trigger conditions used in the experiment. As noted in the text, the unusually large number of excluded pads in set 2 was due to a user error.	69
Table 4.4: Results of fitting the distributions of parameter and energy deviations from Figs. 4.19 and 4.21. The Laplace and Gaussian distributions are defined in Eqs. (4.22) and (4.23), respectively. The units listed apply to both the centroid and width parameters. The full width at half-maximum (FWHM) was defined as $2\sigma\sqrt{2\log(2)}$ for the Gaussian distributions and $2b\log(2)$ for the Laplace distributions.	87
Table 5.1: Parameter values used while analyzing the $^{46}\text{Ar}(\text{p}, \text{p}')$ data. The vectorial values are given in the beam coordinate system of Fig. 3.2.	106
Table 5.2: Properties of the resonances shown in Fig. 5.26. Energies and widths are given in keV/u. $E_{\text{Ar}}^{\text{CM}}$ is the energy of the corresponding level in the analogue nucleus calculated assuming $\Delta E_C - S_n = 2807(30)$ keV, from the literature values of those parameters; E_x is the excitation energy calculated from the resonance assuming $\Delta E_C - S_n = 2680(20)$ keV, the energy of the ground state resonance; S refers to the spectroscopic factor; Γ is the total resonance width; Γ_p is the proton single-particle width; and Γ_\downarrow is the spreading width arising from mixing with the $T_<$ states. For quantities with two uncertainties, the first value is the systematic uncertainty and the second is statistical. .	127
Table 5.3: Renormalization factors applied to spectroscopic factors from DSIGMAIV.	129
Table 5.4: Calculated values of the resonance integral from Eq. (5.17) and the relative uncertainty $\delta I/I$ it contributes to the spectroscopic factor for a variation of 10 keV in Γ_\downarrow	129
Table 5.5: Straggling at the resonance locations.	130

Table 5.6: Statistical significance of the proposed resonances. The first three lines show the results of the *F*-test applied to the three individual resonances. The last line shows the result of the test applied to the data as a whole. 131

Table 5.7: Literature values of the measured excitation energies and spectroscopic factors. The SDPF, SDPF-U, and SDPF-MU values are from shell model calculations performed by the authors of the referenced papers. 133

LIST OF FIGURES

Figure 1.1: Chart of the nuclides. Neutron number increases along the horizontal axis, and proton number increases along the vertical axis. The color corresponds to the log of the half-life, with lighter colors indicating a longer half-life. Stable nuclei are colored black.	2
Figure 1.2: The first few levels of the nuclear shell model (level spacings are not drawn to scale). The number in parentheses next to each level indicates the number of nucleons that fit in that level. The shell gaps are shown with dotted lines. The boxed number to the left of each shell gap line is the number of nucleons that fit below that shell closure. These are the first few magic numbers.	3
Figure 1.3: Three isobaric nuclei with isospin projections $T_z = -1, 0$, and $+1$ from left to right. Sets of isobaric analogue states are indicated with dashed lines. The ground states of the ${}^6\text{He}$ and ${}^6\text{Be}$ spectra are printed higher than that of ${}^6\text{Li}$ to make the correspondence more apparent. Energies are given in keV. (Data taken from [38].)	5
Figure 1.4: A high-resolution measurement of the excitation function from ${}^{40}\text{Ar}(\text{p}, \text{p}')$. The bottom plot shows a theoretical fit to the data near 2.45 MeV. Spin-parity assignments were made based on the shape of the resonances, and it is apparent that the $1/2^+$ and $3/2^-$ resonances are split into several fine-structure components. (Figure reproduced from [22, Fig. 19.13], which was adapted from [7].)	10
Figure 1.5: Calculating the resonance energy of the isobaric analogue state labeled “IAS”. In this figure, S_n is the neutron separation energy, δ is the difference between the neutron and proton masses, ΔE_c is the Coulomb energy of the last proton, and E_r is the resonance energy. The ground state of ${}^{47}\text{K}$ is located far below the bottom of the figure and is not shown. The energy separations are not drawn to scale.	10
Figure 1.6: Trends in $E(2_1^+)$ and $B(E2)$ near the $N = 20$ and $N = 28$ magic numbers. (Reproduced from [49].)	12
Figure 1.7: Energy spectrum of $d({}^{46}\text{Ar}, {}^{47}\text{Ar})\text{p}$ observed by Gaudefroy et al. [16]. Subplot (a) shows the spectrum with background curves from carbon-induced reactions only (labeled “C”) and from carbon-induced reactions and deuteron breakup (labeled “C + d”). Subplot (b) shows the background-subtracted spectrum fit with 9 Gaussian curves. Subplot (c) shows the spectrum of events where protons were in coincidence with the ${}^{47}\text{Ar}$ nucleus. (Reproduced from [16, Fig. 1].)	14
Figure 1.8: A comparison of neutron single-particle energies in ${}^{49}\text{Ca}$ and ${}^{47}\text{Ar}$ from Gaudefroy et al. [16]. The splitting of the $1p$ orbitals is reduced in ${}^{47}\text{Ar}$ compared to ${}^{49}\text{Ca}$. (Reproduced from [16, Fig. 3].)	15
Figure 1.9: Energy levels identified by Bhattacharyya et al. [6]. (Adapted from [6, Fig. 3].)	16

Figure 1.10: γ -ray spectrum measured by Gade et al. [15]. The results from each reaction are shown separately, and levels indicated in gray were not observed using a given reaction. (Reproduced from [15, Fig. 3].)	16
Figure 2.1: Principle of operation of a TPC. A uniform electric field is created between the anode and the cathode. This field transports the ionization electrons produced by a charged particle towards the anode, where they are amplified and collected.	19
Figure 2.2: A schematic view of the AT-TPC. The outer shielding volume was made transparent in this image to make the details of the inner volume more visible. Beam enters the detector through the beam duct at the right-hand side of the image and moves toward the sensor plane on the left. Some components of the GET electronics are shown mounted on the downstream end of the detector (see Section 2.4).	21
Figure 2.3: A photograph of the inner volume wall with the rings of the inner field cage installed. The outer field cage rings have a larger diameter, but are otherwise identical and are installed on the outer surface of the cylinder.	22
Figure 2.4: Layout of the pad plane. The inset shows a closer view of one corner of the hexagonal inner region. This region of half-scale pads provides finer resolution near the reaction vertex, which will generally occur near the central axis of the detector.	24
Figure 2.5: Principle of operation of a Micromegas. The electric field magnitudes shown are nominal: the field in the region above the mesh may vary from roughly 10^3 V/m to 10^5 V/m.	24
Figure 2.6: Illustration of pileup separation due to the tilt angle. The leftmost track is elastic α - α scattering, and the rightmost track is another α particle that entered the detector during the event. Without the tilt angle, the two beam tracks would be collinear, making them more difficult to separate.	25
Figure 2.7: A schematic view of the GET electronics system. Only one AsAd is shown for clarity, but 40 AsAds are used to instrument the AT-TPC.	26
Figure 2.8: A photograph of the fully instrumented AT-TPC mounted inside its solenoid magnet. The 40 AsAds are mounted on the downstream end flange surrounded by copper shielding. Individual cables connect each AsAd to its controlling CoBo, and a separate set of cables connects each to its power supply.	28
Figure 2.9: Structure of the DAQ system. Only two worker nodes are shown, but there are ten in the actual system.	29
Figure 3.1: Subtracting the baseline from a single signal. The top plot shows the raw signal and the calculated baseline. The bottom plot shows the difference between the two.	32

Figure 3.2: Coordinate systems used in the analysis. After calibration, the recorded tracks are in the detector coordinate system (a). This system has its origin in the center of the sensor plane at $z = 0$ with the z axis pointing upstream toward the beam entrance window. The beam coordinate system (b) is related to the detector coordinate system by a rotation through angle τ about the beam entrance window, where τ is the detector tilt angle. In this system, the beam moves along the $-w$ axis. Note that both of these coordinate systems are left-handed.	33
Figure 3.3: Event 99-30 from the ^{46}Ar data set, a particularly noisy event, before cleaning. There are some correlated noise structures present at the bottom of the uv projection and the left of the wv projection, and there is uncorrelated noise throughout the event.	36
Figure 3.4: Parameterizing a straight line in two dimensions using a normal line drawn to the origin.	37
Figure 3.5: Transforming points into the Hough space. The left-hand plot shows three points A , B , and C in the normal coordinate space with lines drawn between them. These points map to sinusoidal curves in the Hough space, as shown in the right-hand plot. Lines in the normal system become points in the Hough space, so a line that passes through two points in the normal space is the intersection of two curves in the Hough space.	37
Figure 3.6: Finding the center of a circle using the Hough transform.	38
Figure 3.7: Cleaning an event with the Hough transforms. Plot (a) shows the data from Fig. 3.3 in the $\rho\phi$ vs w space with the found lines. The colored points are classified as data, while the empty points are noise. Plot (b) shows the Hough space calculated for this data. The maximum angular slice is shown between the two white lines, and the 1D projection of this slice is shown on the right with the peak locations marked.	41
Figure 3.8: Final results of the noise removal process on the event shown in Fig. 3.3. The blue points were kept, and the semi-transparent red points were removed as noise. Some noise is still present after cleaning, but much of it was removed.	42
Figure 3.9: Template used to simulate diffusion. The charge q from the initial point is distributed among the diffused points. The central point gets $0.4q$ units of charge, and the outer points each get $0.6q/8$ units of charge. This is based on a two-dimensional normal distribution.	44
Figure 3.10: Samples drawn by the Monte Carlo algorithm while fitting one event. The horizontal axes represent the sample number, while the vertical axes represent the value of each of the 6 variables. x , y , and z are given in meters, E is in MeV, and θ and ϕ are in radians. Each 500-sample iteration of the code is visible as a large-scale block in this plot.	48

Figure 3.11: Results of the Monte Carlo convergence study. Subplots represent different numbers of points T per iteration. Within each plot, rows represent the reduction factor R , and columns represent the number of iterations I . The number in each cell represents the percentage of fits in which the optimizer converged to the correct minimum, subject to a tolerance of 10 mm in each dimension for the vertex position, 100 keV for the initial proton energy, 5° for the azimuthal angle, and 2° for the scattering angle. The fit was run 1000 times on the same simulated track for each set of parameters.	49
Figure 3.12: Simulated two-dimensional error surface and a one-dimensional slice through that surface. These were generated from a simulated $^{46}\text{Ar}(\text{p},\text{p}')$ scattering event by varying the scattered proton's initial energy and scattering angle, calculating the objective function at each point. 400 points were simulated in each dimension. On the surface plot, the horizontal axis represents energy in MeV, the vertical axis represents the energy component of the objective function, and the axis going into the page represents the scattering angle in radians.	50
Figure 3.13: An illustration of the points tested in the Nelder-Mead simplex method. The vertex v_2 is reflected across the point c using four different values of the multiplicative factor α , leading to the four possible new vertices, shown in purple, yellow, blue, and green. (Reproduced from [28, Fig. 4.2(b)].)	52
Figure 3.14: Steps taken by a vertex during simplex collapse, a failure mode of the Nelder-Mead algorithm. (Reproduced from [35, Fig. 2.1].)	53
Figure 4.1: Illustration of coordinate calculation for uniform distributions. The meanings of the variables are given in Section 4.1.1.1. Note that this is a projection into the zy plane, and the true three-dimensional orientation also depends on azimuthal angles ϕ and ϕ_B and vertex location x_0	59
Figure 4.2: Results of DSIGMAIV calculation in the region of interest.	62
Figure 4.3: Schematic of a channel in the GET electronics, showing the trigger threshold circuit. (Reproduced from [3].)	66
Figure 4.4: Trigger exclusion and low-gain regions used in the simulation and in the experiment. Only pads in the light and dark gray regions contribute to the trigger.	70
Figure 4.5: Distributions of the χ^2 values for the simulated events in the first three sets of runs. Events that fell outside of the shaded region between the two vertical black lines on the histogram were thrown away. The events that were kept had $\chi_{\text{pos}}^2 < 1.0$ and $\chi_{\text{en}}^2 < 1.0$. This plot does not include events for which the fitter returned an error.	71
Figure 4.6: Distributions of χ^2 values for the final two sets of runs. See the caption of Fig. 4.5 for details.	72

Figure 4.7: Simulated acceptance of the trigger and analysis as a function of the track parameters for trigger parameter set 0. The trigger and analysis cuts were applied independently to the simulated events, leading to six classes of events. Events are grouped into “trigger” and “no trigger” groups depending on whether they would have triggered the electronics in a real experiment. These groups are then subdivided into “good fit” and “bad fit” groups depending on whether they pass the χ^2 cuts. Events in the “fit failed” groups caused an error in the Monte Carlo algorithm. Only events in the “trigger, good fit” group would have been recorded and correctly reconstructed in the experiment. The six groups are stacked in these histograms, so the contour of the top of each plot reflects the shape of the total distribution.	73
Figure 4.8: Simulated acceptance of the trigger and analysis for trigger parameter set 2. The large trigger exclusion region used in these runs prevented events outside of a very small angular and energy domain from being accepted.	74
Figure 4.9: Simulated acceptance of the trigger and analysis for trigger parameter set 3.	75
Figure 4.10: Simulated acceptance of the trigger and analysis for trigger parameter set 4.	76
Figure 4.11: Simulated acceptance of the trigger and analysis for trigger parameter set 5. The acceptance was reduced for these runs due to the exclusion of CoBos 4 and 9 from the trigger. This is most visible in the distribution with respect to the azimuthal angle.	77
Figure 4.12: Efficiencies of the AT-TPC trigger, the analysis χ^2 cuts, and the total of the two for the first three sets of parameters, plotted as functions of the ^{46}Ar energy at the reaction vertex and the scattering angle in the center of mass frame. The bins used were 5° wide in the angular dimension and 50 keV wide in the energy dimension.	79
Figure 4.13: Efficiencies of the AT-TPC trigger, the analysis χ^2 cuts, and the total of the two for the last two sets of parameters. See the caption of Fig. 4.12 for details.	80
Figure 4.14: Efficiencies for parameter set 0 as a function of ^{46}Ar vertex energy at several scattering angles. The error bars shown are $\pm\sigma_{\epsilon,i}$ as defined in Eq. (4.21). The bins used in this plot are the same as those used in the 2D histograms in Figs. 4.12 and 4.13.	81
Figure 4.15: Efficiencies for parameter set 2 as a function of ^{46}Ar vertex energy at several scattering angles.	82
Figure 4.16: Efficiencies for parameter set 3 as a function of ^{46}Ar vertex energy at several scattering angles.	83
Figure 4.17: Efficiencies for parameter set 4 as a function of ^{46}Ar vertex energy at several scattering angles.	84
Figure 4.18: Efficiencies for parameter set 5 as a function of ^{46}Ar vertex energy at several scattering angles.	85

Figure 4.19: Simulated resolution of the AT-TPC. These six plots show the error in the reconstruction of each of the six track parameters, defined as the reconstructed value minus the correct value. The results of the fits to these distributions are given in Table 4.4. . .	87
Figure 4.20: Illustration of relationship between uncertainty in vertex location and error in azimuthal angle. The reconstructed vertex is marked with an orange square, while the actual vertex location is marked with a blue circle. The red curve represents the proton track. The tangent lines at these two locations have very different slopes.	88
Figure 4.21: Simulated resolution of the two energy reconstruction techniques from Section 3.7. The widths of the distributions are given in Table 4.4. ΔE_{kin} and ΔE_{pos} are defined as the difference between the energies as calculated from the reconstructed parameters and the known correct parameters. For the rightmost plot of $E_{\text{kin}} - E_{\text{pos}}$, both values were found from the reconstructed parameters. The difference between the two energies for the known correct parameters is not shown since those two values are identical. Note that the horizontal scale is different on the center plot.	89
Figure 4.22: Distributions of the objective function components for simulated events drawn from the R matrix calculation results. Each distribution was cut at 1.0, discarding all events with a larger value of χ^2 . This is the same cut that was used for the flat distribution (see Figs. 4.5 and 4.6).	89
Figure 4.23: Two-dimensional histogram of results from the R matrix-based simulation. The two expected resonance locations are marked on the vertical axis at 2.696 MeV/u and 3.875 MeV/u. The two individual bright bins at 80° and 85° are artifacts from dividing by the very small number of counts in those bins.	90
Figure 4.24: Excitation functions derived from the R matrix simulation. The expected locations of the two resonances are shown with vertical orange lines.	92
Figure 5.1: A diagram of the NSCL beamline, with some regions of the facility labeled. The beam starts at the ion sources (label 1) and ends at the AT-TPC (label 14). (Reproduced from http://nscl.msu.edu/public/virtual-tour.html).	94
Figure 5.2: The A1900 fragment separator and the coupled cyclotrons. (Reproduced from [36].) . .	94
Figure 5.3: Timing of events recorded by the GET electronics. Particles arrived in bunches at a rate of approximately 2 Hz. Note that this only shows events that triggered the electronics; in reality, many more nuclei arrived in each bunch.	95
Figure 5.4: A signal from the ion chamber (see Section 5.2.2) from an event where four particles entered the detector.	96

Figure 5.5: Plots of various signals in a spark-like event. The top left plot shows the individual signals in the GET electronics, and the top right plot shows the sum of these signals. The bottom left plot contains the signal from the ion chamber, and the bottom right plot shows the signal from the Micromegas mesh. The gray regions indicate domains in which there is no data. The time buckets in the two DAQ systems are of the same width, but are offset by 100 due to the trigger delay.	100
Figure 5.6: Plots of (x, y, z) positions corresponding to peak locations in a spark-like event. The majority of the channels in the inner region of the pad plane fired at approximately the same time.	100
Figure 5.7: A raw ion chamber signal produced by an ^{46}Ar nucleus. The passage of the nucleus through the chamber is indicated by the large negative peak around $t = 160$. The ADC used to record this signal was 12 bits, but it also had an overflow bit that made it effectively record 13 bits per sample for a maximum digitized value of 8192.	103
Figure 5.8: Distribution of peak heights in the ion chamber. The center of the ^{46}Ar peak is indicated by the dashed vertical line, and the boundaries of the cut applied around this peak are shown with solid lines.	108
Figure 5.9: A recorded beam track from the ^{46}Ar experiment. The top panel shows the traces from the low-gain region of the sensor plane, which is where the beam track is projected onto the pads. The signals have an unusual shape which is much different from the signals generated by the proton tracks. The inset illustrates the failure of the baseline restoration for one track. In the lower panel, the red squares correspond to the reconstructed beam track, which is quite sparse.	109
Figure 5.10: Distributions of the objective function components from fitting experimental data. The position component was cut at 14, while the energy component was cut at 10. Events with larger values for either of these components were discarded.	110
Figure 5.11: Distribution of reconstructed proton vertex energies from the experiment. Note that the vertical axis uses a logarithmic scale.	110
Figure 5.12: Distribution of reconstructed scattering angles in the center-of-mass frame.	111
Figure 5.13: Distribution of vertex positions in the detector. Plot (a) shows the overall distribution of vertex positions in the plane transverse to the beam. Plot (b) shows that the radius of this distribution increases for smaller z , or for vertex positions further from the beam entrance window.	112
Figure 5.14: ^{46}Ar vertex energies as reconstructed from the vertex position (top) and from kinematics (bottom). The reconstruction methods are detailed in Section 3.7.	113
Figure 5.15: A comparison of the two vertex energy reconstructions. The line $y = x$ is plotted for reference.	114

Figure 5.16: Positional vertex energy recalibration. The 2D histogram shows values of $E_p / \cos^2(\theta_{\text{lab}})$, and the two curves show values of $4E_{\text{Ar}}$. The original calibration is shown with a dashed red curve, and the corrected calibration is shown with a solid cyan curve. The error band on the corrected calibration shows the interval $1.065 \leq \alpha \leq 1.115$, where the best value is in the center at $\alpha = 1.09$. Events with $\theta_{\text{lab}} > 65^\circ$ were eliminated from this plot to reduce the spread at higher energies caused by $\cos^2(\theta_{\text{lab}})$ approaching 0.	116
Figure 5.17: Derivatives of kinematic lines at a few proton energies. The vertex energy changes very rapidly as a function of scattering angle as the scattering angle approaches 90° in the laboratory frame.	116
Figure 5.18: Results of a fit to the edge of the positional vertex energy distribution. The fit was performed with the function defined in Eq. (5.4), yielding parameters $\mu = 4.11 \text{ MeV/u}$, $\sigma = 19.7 \text{ keV/u}$, $A = 694$, and $b = 1.98$. The bins in the energy dimension were 10 keV/u wide, and the error bars shown are $\pm \sqrt{N}$.	117
Figure 5.19: Two-dimensional histogram showing measured counts binned as a function of ${}^{46}\text{Ar}$ vertex energy in the laboratory frame and scattering angle in the center-of-mass frame.	118
Figure 5.20: Unnormalized excitation functions as a function of ${}^{46}\text{Ar}$ vertex energy in the laboratory frame, shown at a variety of center-of-mass scattering angles. The error bars shown are $\pm \sqrt{N}$, where N is the number of counts in a given bin.	119
Figure 5.21: Simulated total efficiencies for parameter set 3 (as defined in Table 4.3) with kernel ridge regression fit. Similar fits were performed for the efficiencies generated for the other parameter sets.	122
Figure 5.22: Excitation functions in the region of interest for ${}^{46}\text{Ar}(p, p')$ calculated from experimental results. The results of an R matrix calculation performed with DSIGMAIV is also shown for comparison. The parameters used in this calculation are given in Section 5.3.10.	123
Figure 5.23: Experimental counts summed over all scattering angles and fit with a quadratic function. The fit function was $y(x) = -263(12)x^2 + 1687(74)x - 1207(108)$, where the numbers in parentheses are the standard errors of the fit coefficients. A 1σ error band is shown around the fit using shading.	124
Figure 5.24: Weighted total excitation function defined in Eq. (5.11) calculated for both the full R matrix simulation (labeled “Full calculation”) and a calculation with no resonances (labeled “Baseline”).	125
Figure 5.25: Effect of convolving the R matrix calculation with a Gaussian. The resonances in the convolved version are wider and have significantly smaller amplitudes.	126
Figure 5.26: Comparison of data to R matrix calculation.	127

Figure 5.27: Results of energy straggling calculation with TRIM [57]. The orange line is a linear fit to the data with slope $-3.12(35)$ keV/MeV and intercept $16.2(10)$ keV. The shaded orange band is a 1σ error band. 130

Figure 5.28: Comparison between experimental results and literature values. Filled shapes indicate experimentally measured values, while empty shapes indicate shell model calculations. 133

LIST OF ALGORITHMS

Algorithm 1:	Hough space binning method	38
Algorithm 2:	Counting nearest neighbors inside a radius	42
Algorithm 3:	Basic compass search algorithm [28]	51
Algorithm 4:	Basic simulated annealing	54

CHAPTER 1

INTRODUCTION

One of the primary goals of nuclear physics research is to understand the structure of the nucleus. While the introduction of the nuclear shell model helped explain the structure of stable nuclei, the exotic, neutron-rich nuclei produced by modern radioactive beam facilities continually present new challenges to our understanding of nuclear structure far from stability. In these neutron-rich nuclei, the predictions made by the shell model based on stable nuclei begin to break down, leading to changes in single-particle levels and shell gaps.

This thesis describes an experiment that was performed to study the structure of ^{47}Ar , an isotope with 18 protons and 29 neutrons that lies in a region of particular interest for studies of shell evolution. This introductory chapter begins with a brief review of some relevant concepts from nuclear physics. The motivations behind the experiment are then described in detail.

1.1 Nuclear physics background

Individual nuclei are characterized by the number of neutrons and protons they contain. A group of nuclei with the same number of protons Z are called *isotopes*, while a group with the same number of neutrons N are called *isotones*. Nuclei with the same mass $A = Z + N$ are called *isobars*. The full set of known nuclei is often displayed in a chart like the one in Fig. 1.1. There, vertical lines group isotones, horizontal lines group isotopes, and lines parallel to the line $Z = -N$ group isobars.

1.1.1 Magic numbers and the nuclear shell model

Although several models have been proposed to describe the structure of the nucleus, the best model currently known is the nuclear shell model. The shell model was first developed in 1949 [9] by physicists including Maria Goeppert Mayer, J. Hans D. Jensen, and Eugene Wigner—who later shared the 1963 Nobel Prize in Physics for their work—to explain the existence of the so-called *magic numbers* of protons and neutrons shared by many of the most stable nuclei. The key feature of this model was the proposal of a shell structure for nucleons (protons and neutrons) analogous to that of electrons in atomic orbitals.

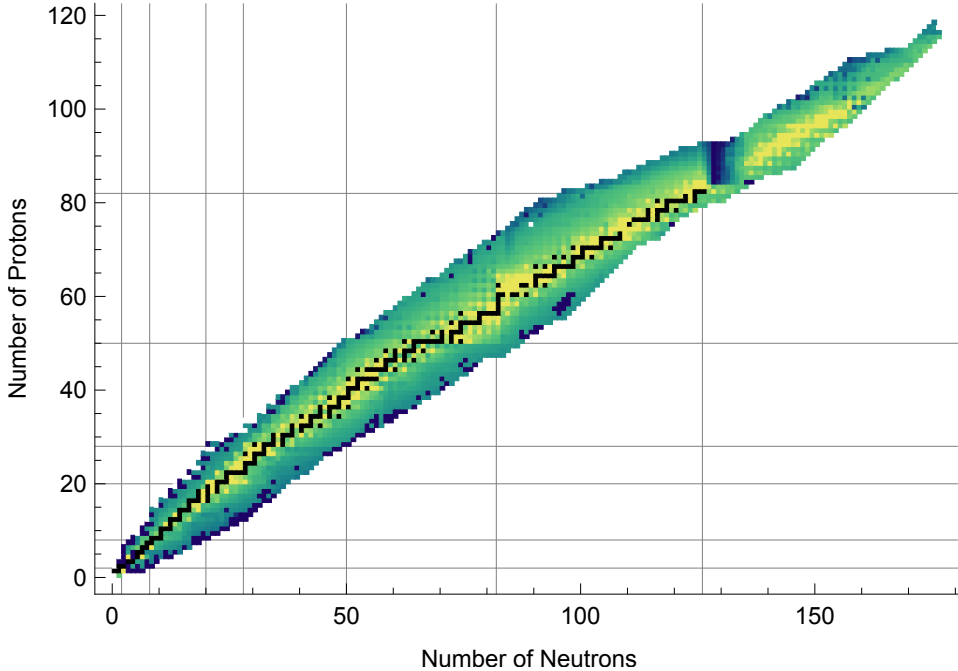


Figure 1.1: Chart of the nuclides. Neutron number increases along the horizontal axis, and proton number increases along the vertical axis. The color corresponds to the log of the half-life, with lighter colors indicating a longer half-life. Stable nuclei are colored black.

A few of the lowest-energy shells are shown in Fig. 1.2. The left-hand column shows the shells predicted by assuming that nucleons are bound by a harmonic oscillator potential. However, to reproduce many of the experimentally observed magic numbers (particularly those at higher N or Z), the model must be extended to include a spin-orbit interaction [49]. This produces the set of levels shown on the right-hand side of the figure. For example, the neutron shell gap at $N = 28$ arises due to spin-orbit splitting of the $1f$ oscillator shell that pushes the $1f_{7/2}$ level to a somewhat lower energy than the $1f_{5/2}$ level and the two levels derived from the $1p$ shell, which are all grouped together at a higher energy.

1.1.2 Single-particle states

The simple picture of the shell model presented above is derived for a single particle bound in a simple potential well, like that of a harmonic oscillator or Woods–Saxon function. However, the energy levels of actual nucleons are much more complex and depend on interactions with all of the other nucleons in the system. Therefore, the energy levels measured experimentally are not equivalent to the single-particle energy levels predicted by theory. Instead, the single-particle energies can be defined as a weighted sum

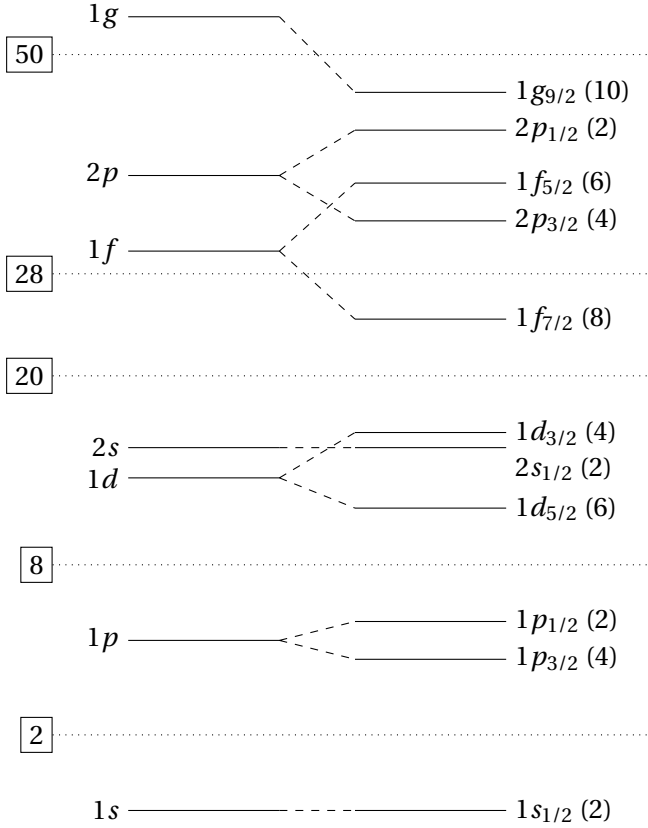


Figure 1.2: The first few levels of the nuclear shell model (level spacings are not drawn to scale). The number in parentheses next to each level indicates the number of nucleons that fit in that level. The shell gaps are shown with dotted lines. The boxed number to the left of each shell gap line is the number of nucleons that fit below that shell closure. These are the first few magic numbers.

of the actual energy levels: [2]

$$\epsilon_\alpha = \sum_i S(\alpha, i) E_i. \quad (1.1)$$

In this sum, the single-particle energy ϵ_α of particle α is related to the experimental energy levels E_i having the same spin and parity as the single-particle state. The weighting factors $S(\alpha, i)$ are the spectroscopic factors, which can be thought of as the probability of finding the particle α in the given single-particle state.

A more thorough theoretical treatment of the notion introduced in Eq. (1.1) is given by Baranger [2]. They define a single-nucleon Hamiltonian W by

$$\langle \alpha | W | \beta \rangle = \sum_n \langle \psi_0 | a_\alpha | \chi_n \rangle (E_n - E_0) \langle \chi_n | a_\beta^\dagger | \psi_0 \rangle + \sum_N \langle \psi_0 | a_\beta^\dagger | \chi_N \rangle (E_0 - E_N) \langle \chi_N | a_\alpha | \psi_0 \rangle. \quad (1.2)$$

The matrix elements in this sum connect the ground state $|\psi_0\rangle$ (with energy E_0) of a nucleus with mass number A to the set of states $|\chi_n\rangle$ (with energy E_n) in the adjacent $A+1$ “particle” nucleus and the set

of states $|\chi_N\rangle$ (with energy E_N) in the $A - 1$ “hole” nucleus. $|\beta\rangle$ and $|\alpha\rangle$ are two single-particle states with corresponding creation and annihilation operators a_β^\dagger and a_α . Baranger [2] points out that if these states are assumed to be eigenstates of W , then W must be diagonal, so Eq. (1.2) reduces to

$$\epsilon_\alpha \equiv \langle \alpha | W | \alpha \rangle = \sum_n |\langle \psi_0 | a_\alpha | \chi_n \rangle|^2 (E_n - E_0) + \sum_N |\langle \chi_N | a_\alpha | \psi_0 \rangle|^2 (E_0 - E_N). \quad (1.3)$$

They then identify $|\langle \psi_0 | a_\alpha | \chi_n \rangle|^2$ with the spectroscopic factor and $(E_n - E_0)$ with the energy E_i from above, assuming the reference state $|\psi_0\rangle$ is the ground state.

1.1.3 Isobaric analogue states

Many measurements of nuclear spectra have shown that families of isobaric nuclei, or nuclei with the same mass number A but different charges Z , tend to share sets of common energy levels. This occurs because the neutron and proton have very similar masses and behave approximately identically under the strong nuclear force, leaving charge as the main difference between them. If Coulomb repulsion is neglected, the proton and neutron can then be considered as two states of the same particle.

Formally, this symmetry is described using the isospin \mathbf{t} , a vector quantity that behaves identically to ordinary spin vectors. Protons are defined¹ as having isospin projection $t_z = -1/2$, while neutrons have $t_z = +1/2$. The total isospin \mathbf{T} of a nucleus is the vector sum of the isospins of its constituent nucleons, and the total isospin projection, which distinguishes individual members of the isobaric multiplet, can be altered by defining a set of isospin raising and lowering operators much like those used for spin and orbital angular momentum.

Much like how a magnetic field splits degenerate electron orbitals into distinguishable levels based on the projection of their total angular momentum, the presence of the Coulomb force inside the nucleus creates multiplets of states with the same total isospin but different isospin projections. The rest of the quantum numbers of these states are the same, so they have very similar wave functions.

Figure 1.3 shows an example of isobaric analogue states in three nuclei with $A = 6$. Two isospin triplets ($T = 1$) are visible, connecting sets of 0^+ and 2^+ states. The remaining, unique states in ${}^6\text{Li}$ are isospin singlets ($T = 0$).

¹Although this sign convention is commonly used in nuclear physics, other fields use the opposite convention.

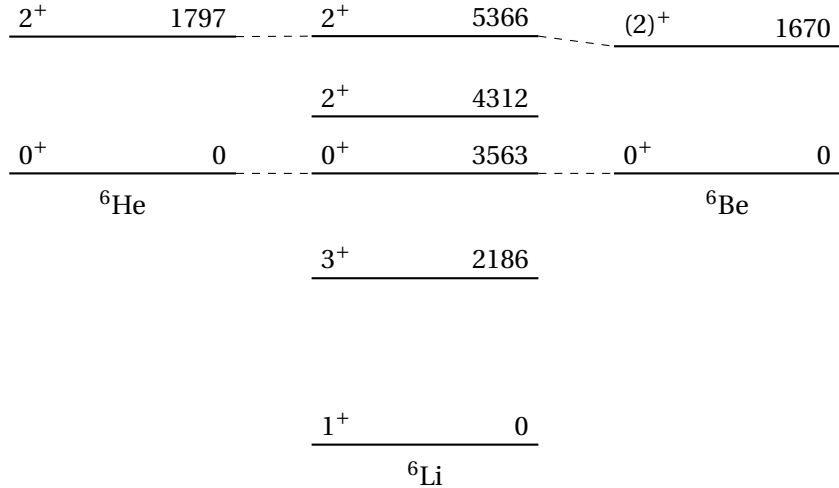


Figure 1.3: Three isobaric nuclei with isospin projections $T_z = -1, 0$, and $+1$ from left to right. Sets of isobaric analogue states are indicated with dashed lines. The ground states of the ${}^6\text{He}$ and ${}^6\text{Be}$ spectra are printed higher than that of ${}^6\text{Li}$ to make the correspondence more apparent. Energies are given in keV. (Data taken from [38].)

1.1.4 Elastic scattering in quantum mechanics

The quantum mechanical description of the elastic scattering of nuclei off a potential $V(\mathbf{r})$ depends on the solution of the time-independent Schrödinger equation [22]

$$\nabla^2 \psi + \frac{2m}{\hbar^2} [E - V(\mathbf{r})] \psi = 0. \quad (1.4)$$

In spherical coordinates, the solution to this equation must approach

$$\psi(\mathbf{r}) \xrightarrow{r \rightarrow \infty} e^{ikz} + \frac{e^{ikr}}{r} f(\theta) \quad (1.5)$$

at large distances from the scattering center at the origin [22]. The first component of this expression represents an unscattered plane wave with wavenumber k moving along the same direction z as the incoming particle, and the second component represents a spherical wave propagating outward from the scattering center as a function of radius r . Assuming azimuthal symmetry, the factor $f(\theta)$ defines what proportion of the incoming wave was scattered as a function of the scattering angle θ , so the elastic scattering cross section can be written as [22]

$$\frac{d\sigma}{d\Omega} = |f(\theta)|^2. \quad (1.6)$$

Equation (1.4) is commonly solved by expanding ψ over partial waves with discrete values of angular

momentum L :

$$\psi(r, \theta) = \sum_{L=0}^{\infty} \frac{u_L(r)}{r} P_L(\cos \theta). \quad (1.7)$$

Here, $u_L(r)$ is the radial component of the wave function, and the $P_L(\cos \theta)$ are the Legendre polynomials. Applying boundary conditions leads to the following solution for $f(\theta)$: [22]

$$f(\theta) = \frac{1}{2ik} \sum_{L=0}^{\infty} (2L+1) \left(e^{2i\delta_L} - 1 \right) P_L(\cos \theta). \quad (1.8)$$

Here, k is the wavenumber, and δ_L is called the phase shift, which contains all of the physical information about the scattering [22]. The phase shift is often used to define the scattering or S matrix element

$$S_L = e^{2i\delta_L}. \quad (1.9)$$

1.1.5 The optical potential

One commonly used model for the nuclear potential is the *optical model*. This model represents the nuclear potential as a complex quantity with a real component that produces scattering and an imaginary component that absorbs incoming flux [22]. The absorptive component accounts for non-elastic processes in the interaction [22]. This is known as an “optical” model since it was created by analogy to the scattering of light in a semi-opaque medium, where the proportion of light absorbed by the medium can be quantified using the imaginary part of a complex index of refraction [22].

An optical model is typically formulated using the Woods-Saxon potential

$$V(r) = -\frac{V_0}{1 + \exp\left(\frac{r-R}{a}\right)}, \quad (1.10)$$

where V_0 is the *depth* of the potential well, R is its *radius*, and a is its *diffuseness*, a measure of how quickly the function rises [51]. Both the real and imaginary parts of the optical potential have the form shown in Eq. (1.10), but they may have different parameters.

The nuclear potential is parameterized in terms of several Woods-Saxon potentials. There is generally a real and imaginary volume potential term, and an imaginary surface term is often included as well [51]. Finally, a spin-orbit term may be added to account for the coupling between the spin of the nucleus and its angular momentum [51].

The potential described above only contains a contribution from the strong nuclear force, which acts at short ranges. Scattered charged particles, such as protons, will also experience a long-range Coulomb

force due to the nuclear charge. This contributes the following term to the total potential: [51]

$$V_{\text{Coul.}}(r) = Z_{\text{proj.}} Z e^2 \times \begin{cases} \left(\frac{3}{2} - \frac{r^2}{2R_{\text{Coul.}}^2}\right) \frac{1}{R_{\text{Coul.}}} & r \leq R_{\text{Coul.}} \\ \frac{1}{r} & r \geq R_{\text{Coul.}} \end{cases} \quad (1.11)$$

This potential term depends on the charge $Z_{\text{proj.}} e$ of the projectile, the charge Ze of the nucleus, and the Coulomb radius $R_{\text{Coul.}}$, which is typically proportional to $A^{1/3}$ in a nucleus with mass number A [51].

In total, this leaves us with a model of the scattering potential that depends on 12 or more free parameters which are found by fitting the model to experimental data. Fitting the model to data from a single nucleus at a single energy produces a *local* optical potential, and these local parameterizations will generally describe the data best [51]. However, the model can also be fit to data from a range of nearby nuclei over a range of energies to produce a *global* optical potential with parameters that vary slowly as functions of A and energy. These global potentials tend to fit scattering data worse than a local potential for the nucleus being studied, but they have the benefit of allowing interpolation or extrapolation to nuclei for which a reliable set of data does not yet exist [51].

1.1.6 Resonances and the R matrix theory

During a low-energy nuclear reaction, it is possible for the projectile and target nuclei to temporarily form a short-lived, intermediate-state compound nucleus whose decay products correspond to the exit channel of the reaction. This compound nucleus may be formed in any of a large number of unbound energy levels which correspond to resonances in the measured excitation function, or isolated regions of the excitation function where the cross section departs significantly from the baseline value. As the density of states increases with increasing excitation energies, these resonances eventually merge into a continuous distribution at high energies [22].

Resonances typically occur in one reaction channel and one partial wave, giving them well-defined values of orbital angular momentum L and total angular momentum J . For a spin-0 particle, the cross section near an isolated resonance of this type at energy E_0 with width Γ is described with the Breit–Wigner formula [22]

$$\frac{d\sigma}{d\Omega}(E, \theta) = \frac{(2L+1)^2}{4k^2} \frac{\Gamma^2}{(E - E_0)^2 + \frac{1}{4}\Gamma^2} P_L^2(\cos \theta), \quad (1.12)$$

as a function of energy E and scattering angle θ , with wavenumber k .

Resonances in measured elastic scattering cross sections can be fit using the phenomenological R matrix theory. In the formulation used by Descouvemont and Baye [11], the R matrix for an isolated resonance in a single partial wave with orbital angular momentum ℓ is given by

$$R_\ell(E) = \frac{\gamma_r^2}{E_r - E}. \quad (1.13)$$

In this equation, E_r and γ_r are the *formal* resonance energy and reduced width. These can be calculated from the observed resonance energy E_R and width Γ_R as follows. The formal reduced width γ_r can be calculated from the observed reduced width γ_R using the equation

$$\gamma_r^2 = \frac{\gamma_R^2}{1 - \gamma_R^2 S'_\ell(E_R)}. \quad (1.14)$$

The observed reduced width is found from the observed resonance width Γ_R :

$$\gamma_R^2 = \frac{\Gamma_R}{2P_\ell(E_R)}. \quad (1.15)$$

The formal resonance energy E_r can be calculated in a similar way:

$$E_r = E_R + \gamma_r^2 S_\ell(E_R). \quad (1.16)$$

In Eqs. (1.14) to (1.16) above, S_ℓ is called the *shift factor*, and S'_ℓ is its derivative. P_ℓ is the *penetration factor* and should not be confused with the Legendre polynomials. The penetration factor and shift factor are defined as [11]

$$P_\ell(E) = \frac{ka}{F_\ell^2(ka) + G_\ell^2(ka)} \quad (1.17)$$

$$S_\ell(E) = P_\ell(E) [F_\ell(ka)F'_\ell(ka) + G_\ell(ka)G'_\ell(ka)] \quad (1.18)$$

where F_ℓ and G_ℓ are the regular and irregular Coulomb functions, F'_ℓ and G'_ℓ are their derivatives, k is the wavenumber, and a is the *channel radius*, a somewhat arbitrary boundary chosen such that for $r > a$, the scattering potential is approximately the Coulomb potential.

More practically, the R matrix theory can be used to calculate the collision matrix $U_{cc'}$ between channels c and c' . In the Breit–Wigner approximation, this is

$$U_{cc'}(E) = e^{i(\phi_c + \phi'_{c'})} \left[\delta_{cc'} + \frac{i\sqrt{\Gamma_c(E)\Gamma'_{c'}(E)}}{E_R - E - i\Gamma(E)/2} \right], \quad (1.19)$$

where ϕ_c is the hard-sphere phase shift in this channel [11]. This can then be used to find the elastic scattering cross section

$$\frac{d\sigma}{d\Omega} = \frac{1}{(2I_1+1)(2I_2+1)} \sum_{M_1 M_2} \sum_{M'_1 M'_2} \left| f_C(\Omega) \delta_{M'_1 M_1} \delta_{M'_2 M_2} + f_{c' M'_1 M'_2}^{(c M_1 M_2)}(\Omega) \right|^2 \quad (1.20)$$

with Coulomb scattering amplitude $f_C(\Omega)$ and elastic scattering amplitude [11]

$$\begin{aligned} f_{c' M'_1 M'_2}^{(c M_1 M_2)}(\Omega) = & i \frac{\sqrt{\pi}}{k} \sum_{J\pi} \sum_{I\ell} \sum_{I'\ell'} \sqrt{2\ell+1} e^{i(\sigma_\ell + \sigma_{\ell'})} (I_1 I_2 M_1 M_2 | IM) \\ & \times (I\ell M 0 | JM) (I'_1 I'_2 M'_1 M'_2 | I'M') (I'\ell' M' M - M' | JM) \\ & \times \left(\delta_{c' c} \delta_{I'I} \delta_{\ell'\ell} - U_{c' I'\ell', c I\ell}^{J\pi} \right) Y_{\ell'}^{M-M'}(\Omega). \end{aligned} \quad (1.21)$$

In these equations, I_i for $i = 1, 2$ are the spins of the two colliding particles, ℓ is the orbital angular momentum of the system, J is the total angular momentum of the many-body system, M is the projection of the total angular momentum, and π is the total parity of the system. More detail about the R matrix theory can be found in the review article by Descouvemont and Baye [11].

1.1.7 Isobaric analogue resonances

In some proton-adding or neutron-removing [22] reactions, isospin coupling between the target and the projectile allows the excitation of higher-isospin states in the compound nucleus. For a target nucleus beginning in a state with isospin T , these higher-isospin states have isospin $T_> \equiv T + \frac{1}{2}$. Each $T_>$ state is the isobaric analogue of states in other nuclei with the same mass number A but different isospin projection T_z ; therefore, a measurement of the properties of the resonance in the compound nucleus allows the properties of the analogous states in the other isobars of the multiplet to be deduced.

These $T_>$ isobaric analogue resonances coexist with a potentially large number of $T_< \equiv T - \frac{1}{2}$ resonances corresponding to unbound states of the compound nucleus itself. If the density of the $T_<$ states is large, the $T_>$ states may begin to mix weakly with $T_<$ states that have the same spin and parity [22]. This splits the $T_>$ resonance into several components, creating fine structure in the excitation function as seen in Fig. 1.4. However, if the density of $T_<$ states is very high (or the resolution is lower), the individual components will not be resolvable, and the mixing will instead present itself as a broadening of the $T_>$ resonance [22].

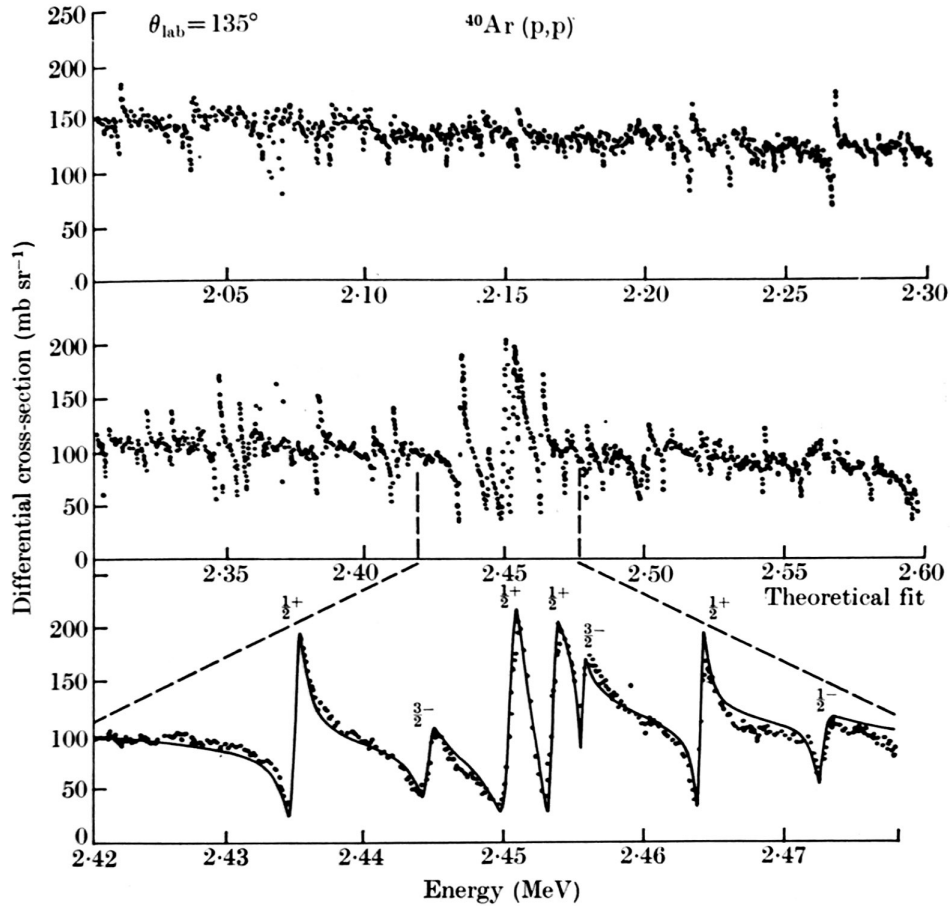


Figure 1.4: A high-resolution measurement of the excitation function from ${}^{40}\text{Ar}(p, p')$. The bottom plot shows a theoretical fit to the data near 2.45 MeV. Spin-parity assignments were made based on the shape of the resonances, and it is apparent that the $1/2^+$ and $3/2^-$ resonances are split into several fine-structure components. (Figure reproduced from [22, Fig. 19.13], which was adapted from [7].)

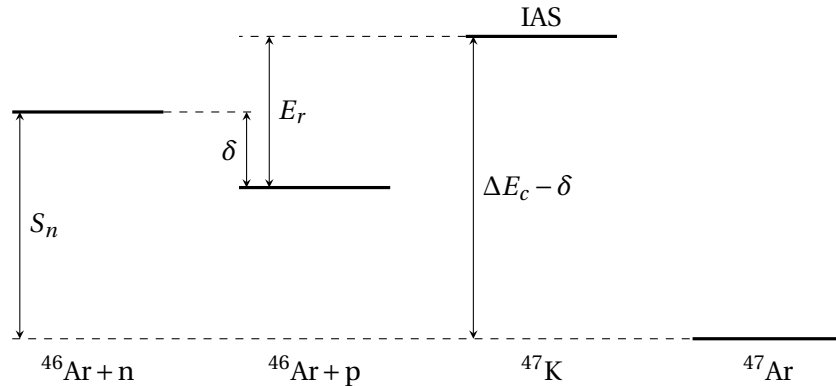


Figure 1.5: Calculating the resonance energy of the isobaric analogue state labeled “IAS”. In this figure, S_n is the neutron separation energy, δ is the difference between the neutron and proton masses, ΔE_c is the Coulomb energy of the last proton, and E_r is the resonance energy. The ground state of ${}^{47}\text{K}$ is located far below the bottom of the figure and is not shown. The energy separations are not drawn to scale.

1.1.8 Calculating the resonance energy

The expected resonance energies can be calculated by comparing the isobaric analogue state to similar systems. Consider, for example, the state in ^{47}Ar shown on the right-hand side of Fig. 1.5. If we assume that the strong nuclear force binds protons and neutrons equally, then the energy difference between the state in ^{47}Ar and its analogue state in ^{47}K must be $\Delta E_c - \delta$, where ΔE_c is the Coulomb energy of the last proton in ^{47}K , and $\delta = m_n - m_p$ is the mass difference between the proton and the neutron.

A similar comparison can be made between the bound ^{47}Ar nucleus and the unbound $^{46}\text{Ar} + \text{n}$ system; in this case, the energy difference is simply the neutron separation energy S_n . This unbound system has an energy that is higher than the unbound $^{46}\text{Ar} + \text{p}$ system where the resonance occurs by an offset of δ .

Putting these pieces together, the energy of the proton emitted when the compound nucleus decays from the isobaric analogue state is the difference in energy between the isobaric analogue state in ^{47}K and the energy of the unbound $^{46}\text{Ar} + \text{p}$ system. This is

$$E_r = (\Delta E_c - \delta) - S_n + \delta = \Delta E_c - S_n. \quad (1.22)$$

Values of ΔE_c can be determined empirically or by simulation; values of S_n are typically found from mass measurements and can be looked up in standard references.

1.2 Experimental motivation

The experiment described in this thesis served several purposes. From the perspective of nuclear physics, the results are interesting because they can contribute to the understanding of the breakdown of the magic numbers near the $N = 28$ shell closure. From a practical perspective, the experiment also served to commission the Active-Target Time Projection Chamber (AT-TPC) with radioactive beams and to test the analysis methods developed for AT-TPC data. These motivations are each described further in this section.

1.2.1 The disappearing $N = 28$ shell gap

While the shell model and magic numbers describe stable and near-stable isotopes relatively well, the shell gaps defined by the magic numbers begin to change in nuclei that lie further from stability. An

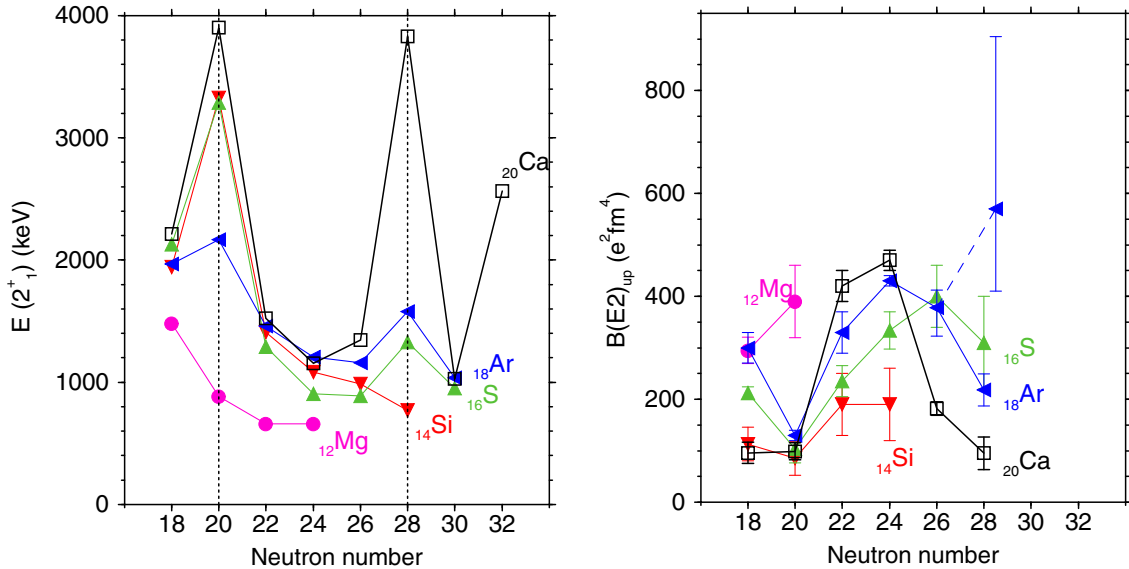


Figure 1.6: Trends in $E(2_1^+)$ and $B(E2)$ near the $N = 20$ and $N = 28$ magic numbers. (Reproduced from [49].)

example of this is predicted in the $N = 28$ isotones, where a reduction of the previously mentioned spin-orbit splitting of the $1f$ states could move the $1f_{5/2}$ level close enough in energy to the $2p_{3/2}$ level to induce a strong electric quadrupole transition strength between the levels [18]. This would be indicative of the onset of nuclear deformation, particularly of quadrupole nature [18], and the emergence of collective behavior and excitations in these nuclei [18, 49].

Several experiments have indicated that the $N = 28$ shell gap disappears as the number of protons decreases from ^{48}Ca . One piece of evidence cited by Sorlin and Porquet [49] is the evolution of the energy of the first 2^+ excited states $E(2_1^+)$ in these isotones as a function of Z . Magic nuclei that follow the shell model would be expected to have large values of $E(2_1^+)$ due to the large shell gap just above their highest-lying single-particle states. This is observed, for instance, in the $N = 20$ isotones, where $E(2_1^+)$ has a strong peak in the doubly magic ^{40}Ca that decays very slowly through ^{38}Ar , ^{36}S , and ^{34}Si before disappearing in ^{32}Mg (see the left-hand plot in Fig. 1.6). Sorlin and Porquet [49] cite this as evidence of an $N = 20$ shell closure that remains strong with decreasing Z until $Z = 14$. In the $N = 28$ isotones, on the other hand, the strong peak in ^{48}Ca is already greatly attenuated at ^{44}S and completely gone by ^{42}Si . This indicates that the $N = 28$ shell closure vanishes much more rapidly with decreasing Z [49].

A second piece of evidence for the departure from standard shell-model behavior is the reduced electric quadrupole transition strength $B(E2; 0_1^+ \rightarrow 2_1^+)$ in these nuclei. This transition strength is expected

to be weak in spherical nuclei due to the large shell gap. As was the case with values of $E(2_1^+)$, this is largely true for the $N = 20$ isotones, which all have a strong minimum for $B(E2)$ except for ^{32}Mg [49]. The $N = 28$ isotones, on the other hand, have widely varying values of $B(E2)$, and the value for ^{46}Ar is not even well-determined since different experimental techniques have yielded incompatible results [49]. This is shown in the right-hand plot of Fig. 1.6.

These measurements, along with β -decay and Coulomb excitation studies, have indicated that nuclear deformation develops smoothly as one removes protons from the spherical, doubly magic ^{48}Ca [49]. In particular, Sorlin and Porquet [49] note that prolate-spherical shape coexistence has been observed in ^{44}S , ^{42}Si is known to be oblate, and ^{40}Mg is predicted to be prolate. This leaves ^{46}Ar in an interesting shape transition region between the deformed ^{44}S and the spherical ^{48}Ca .

In addition to yielding information about nuclear shape in this region, studies of ^{46}Ar and ^{47}Ar can also provide important information about single-particle structure near the $N = 28$ shell gap. Because ^{46}Ar has a closed neutron shell, the shell model predicts that the valence neutron in ^{47}Ar should occupy the next available orbital, which is $2p_{3/2}$. Therefore, reactions populating the ground state and first excited state of ^{47}Ar should exhibit strong p -wave components, as revealed in their spectroscopic factors. Additionally, measurements of the energy gap between the ground state of ^{47}Ar and its $1/2^-$ first excited state provide information about the magnitude of the spin-orbit splitting of the $2p$ harmonic oscillator shell which, as mentioned previously, is expected to shrink as the $N = 28$ shell gap vanishes.

1.2.2 Previous studies of ^{47}Ar

The first [18] experiment to investigate the structure of ^{47}Ar was performed in 2006 by Gaudemar et al. [16, 18]. They populated excited states in ^{47}Ar via the $d(^{46}\text{Ar}, ^{47}\text{Ar})p$ one-neutron transfer reaction with a 10 MeV/u beam of ^{46}Ar generated by the SPIRAL facility at GANIL. The spectrum of ^{47}Ar (shown in Fig. 1.7) was reconstructed from the energies and scattering angles of the outgoing protons, which were measured using position-sensitive silicon telescopes at backward angles between 110° and 170° . By comparison to shell model and distorted-wave Born approximation (DWBA) calculations, they were able to make angular momentum and parity assignments to the ground state and first few excited states (see Table 1.1). In addition, they assigned a neutron single-particle state of $p_{3/2}$ for the ground state and tentatively assigned arrangements of $p_{1/2}$ and $f_{7/2}$ to the first two excited states at 1130 keV and 1740 keV,

E [keV]	ℓ	J^π	$(2J+1)C^2S$
0	1	$3/2^-$	2.44(20)
1130(75)	1	$1/2^-$	1.62(12)
1740(95)	3	$7/2^-$	1.36(16)
2655(80)	3,(4)	$5/2^-$	1.32(18)
3335(80)	3,(4)	$5/2^-$	2.58(18)

Table 1.1: First few levels in ^{47}Ar identified by Gaudefroy et al. [16, Table 1].

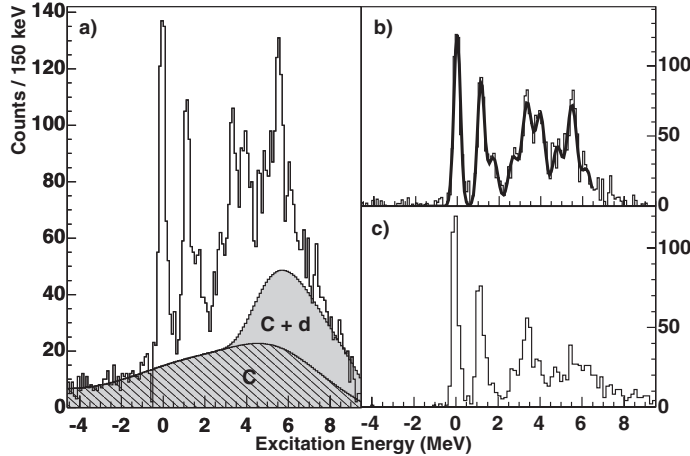


Figure 1.7: Energy spectrum of $d(^{46}\text{Ar}, ^{47}\text{Ar})p$ observed by Gaudefroy et al. [16]. Subplot (a) shows the spectrum with background curves from carbon-induced reactions only (labeled "C") and from carbon-induced reactions and deuteron breakup (labeled "C + d"). Subplot (b) shows the background-subtracted spectrum fit with 9 Gaussian curves. Subplot (c) shows the spectrum of events where protons were in coincidence with the ^{47}Ar nucleus. (Reproduced from [16, Fig. 1].)

respectively [18]. Finally, they calculated spectroscopic factors for each measured state using a variety of different optical potentials.

Using the measured energy levels, Gaudefroy et al. [16] calculated single-particle energies for the $p\ f$ shell states. They concluded that the spin-orbit splitting between the $2p$ levels in ^{47}Ar was reduced by 890(120) keV as compared to ^{49}Ca , and the splitting between the $1f$ levels was reduced by 875(130) keV (see Fig. 1.8). This produces a reduction in the $N = 28$ shell gap of 330(90) keV. This result is controversial, however, and was disputed in a comment published by Signoracci and Brown [48]. They pointed out that when computing the single-particle energies, Gaudefroy et al. [16] neglected to include hole states in the weighted sum. Correcting this leads to a much smaller change in the p -state spin-orbit splitting of 10(130) keV [48]. In response to this comment, Gaudefroy et al. recalculated their values and published a smaller value of 207 keV for the reduction in the spin-orbit splitting of the p states [17].

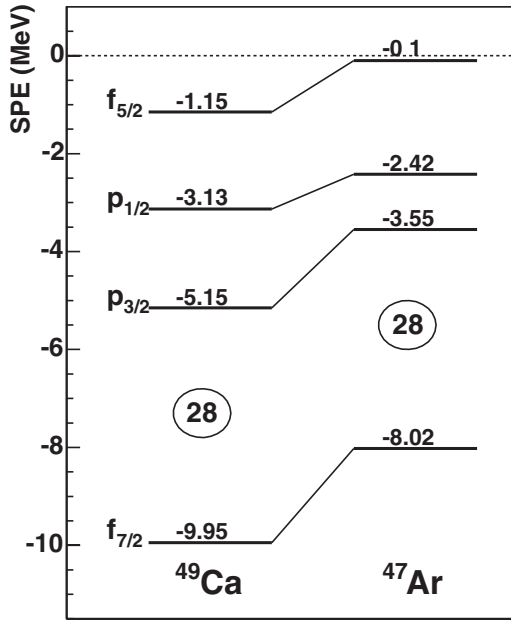


Figure 1.8: A comparison of neutron single-particle energies in ^{49}Ca and ^{47}Ar from Gaudefroy et al. [16]. The splitting of the $1p$ orbitals is reduced in ^{47}Ar compared to ^{49}Ca . (Reproduced from [16, Fig. 3].)

A second experiment performed by Bhattacharyya et al. [6] in 2008 measured the γ -ray spectrum of $^{47,48}\text{Ar}$ produced by deep inelastic transfer reactions between a ^{238}U beam and a ^{48}Ca target. Their results largely agreed with the previous measurement by Gaudefroy et al. [18], although as the reaction mechanism was different, they populated a slightly different set of states. The levels identified in their paper are shown in Fig. 1.9. Of particular interest is the new $5/2^-$ state at 1234(4) keV which is very close to the $1/2^-$ first excited state. This was not observed by Gaudefroy et al. [16], and based on the resolution of the peaks in Fig. 1.7, it would not have been possible for them to separate it from the $1/2^-$ state.

Most recently, a thorough study of the levels in ^{47}Ar was presented by Gade et al. [15] in 2016. They measured the γ -ray spectrum of ^{47}Ar at the NSCL using two different reactions. The first part of the experiment used the GRETINA array and the S800 spectrograph to measure the single-neutron pickup reaction $^{12}\text{C}(\text{Ar}, \gamma)X$. The second part measured the reaction $^9\text{Be}(\text{Ar}, \gamma)X$, or the removal of one proton from the ground state of ^{48}K , using the SeGA array. These two measurements complemented each other by populating different sets of excited states in the ^{47}Ar reaction product, leading to the two spectra shown in Fig. 1.10. Between the two measurements, the authors observed all bound states of the ^{47}Ar nucleus that were known at the time of writing except for the $1/2^-$ state at 1130 keV found by Gaudefroy

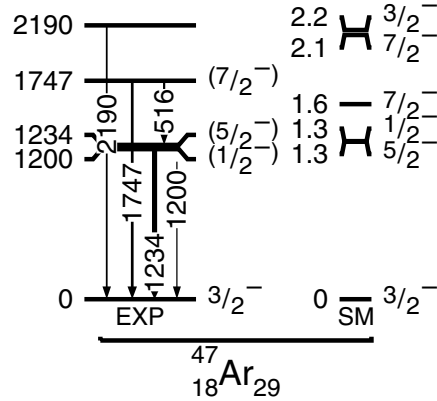


Figure 1.9: Energy levels identified by Bhattacharyya et al. [6]. (Adapted from [6, Fig. 3].)

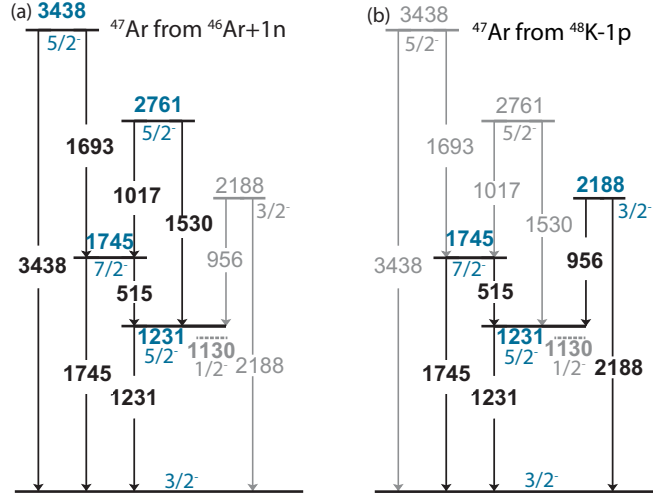


Figure 1.10: γ -ray spectrum measured by Gade et al. [15]. The results from each reaction are shown separately, and levels indicated in gray were not observed using a given reaction. (Reproduced from [15, Fig. 3].)

et al. [18], which could not be populated due to orbital angular momentum constraints.

1.2.3 Resonant proton scattering in inverse kinematics

The resonant proton scattering method described in Section 1.1.7 was used very successfully in the past in direct kinematics experiments. One particularly relevant example is the measurement of $^{40}\text{Ar}(p, p')$ done by Scott et al. [47] in 1968. They bombarded a sealed ^{nat}Ar gas target with a beam of protons from a 5.5 MeV Van de Graaff accelerator. The resulting excitation functions were measured to a high resolution of approximately 3 keV, revealing the fine structure resonance components described in Section 1.1.7;

the gross structure of the resonances was recovered by averaging the data over approximately 25 keV.

Part of the reason these direct kinematics experiments were so successful was due to the characteristics of the proton beams they used. Being nothing more than ^1H , proton primary beams can be produced quite easily and with very high intensity as compared to radioactive secondary beams produced by fragmentation. Furthermore, by virtue of being a primary beam, the incoming proton energies can be controlled very precisely, producing a very small uncertainty in the reaction energy. The combination of fine energy resolution and excellent statistics generally leads to impressive results, as seen in Scott et al. [47].

A natural question, then, is whether this technique can be successfully extended to the modern domain of inverse kinematics experiments which tend to feature a low-intensity beam with a slightly broader energy profile. Some resonant proton scattering experiments have been performed in inverse kinematics, but the technique has not yet been used with heavier radioactive beams in a device like the AT-TPC. This experiment thus also serves as a test of the feasibility of this sort of measurement in this detector.

1.2.4 Commissioning of the AT-TPC

In addition to the nuclear physics goals, the experiment described in this thesis was designed to commission the AT-TPC for use with radioactive beams. The AT-TPC is a newly built time projection chamber with an active-target design that uses the detector gas as a scattering target. This allows reactions to occur anywhere within the active volume of the detector, thereby increasing efficiency and allowing multiple reaction energies to be measured at once. The AT-TPC is described in detail in Chapter 2.

Prior to this experiment, the AT-TPC was used to measure α - α elastic scattering at energies less than 4 MeV/u. The scattering angles measured in this experiment were reconstructed to a resolution of approximately 1°. Immediately prior to the ^{46}Ar experiment, $^{40}\text{Ar}(\text{p}, \text{p}')$ elastic scattering was measured with a stable ^{40}Ar beam in hopes of reproducing the results of Scott et al. [47], but an unforeseen issue with gas contamination made this dataset more difficult to analyze. Therefore, this dataset will be processed at a later time.

1.3 Summary

The remainder of this document describes an experiment that was performed to measure the reaction $^{46}\text{Ar}(\text{p}, \text{p}')$ in inverse kinematics with the AT-TPC. As described above, this was done with the dual purposes of commissioning the AT-TPC with radioactive beams and furthering the understanding of the disappearance of the $N = 28$ shell closure. First, the AT-TPC and its instrumentation are described in detail in Chapter 2. The methods used to analyze AT-TPC data are then defined in Chapter 3. These analysis methods are applied in both Chapter 4, which describes simulations of the experiment and the detector's efficiency, and Chapter 5, which presents the setup of the experiment, its data processing scheme, and its results. Finally, a summary is given in Chapter 6 along with some notes about improvements currently being made to the AT-TPC and its instrumentation.

CHAPTER 2

THE ACTIVE-TARGET TIME PROJECTION CHAMBER

As mentioned previously in Section 1.2.4, one of the goals of the experiment described in this document was the commissioning of the Active-Target Time Projection Chamber (AT-TPC), a new detector that was designed to measure reactions involving low-energy radioactive beams. This chapter begins with a brief background on time projection chambers, while the remaining sections are devoted to a description of the AT-TPC and the equipment used to instrument it during the experiment.

2.1 Background

2.1.1 Time projection chambers

The time projection chamber (TPC) is a type of gas-filled charged particle detector originally invented by Nygren [42] in the 1970s. A TPC consists of a gas-filled vessel equipped with an anode and a cathode capable of producing a moderate electric field. When a charged particle passes through the gas-filled volume, it ionizes some of the atoms that compose the gas, leaving behind a trail of free electrons. The electric field pushes these electrons toward the anode of the chamber, which is typically equipped with some sort of position-sensitive amplification and readout device to count the number of electrons that strike it. This process is illustrated in Fig. 2.1.

The position-sensitive readout plane gives two-dimensional information about the track; the third

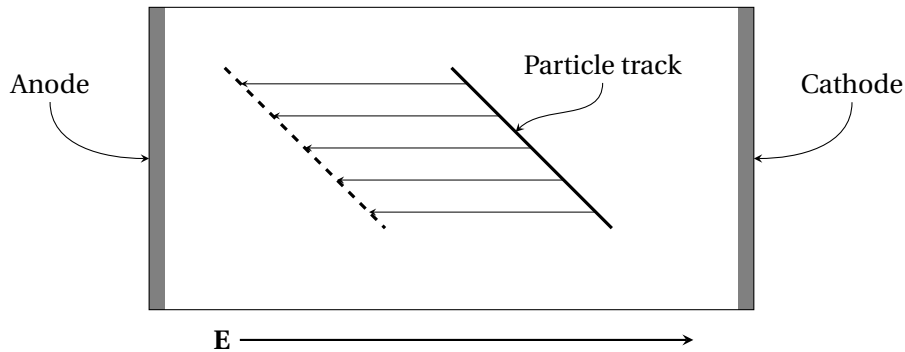


Figure 2.1: Principle of operation of a TPC. A uniform electric field is created between the anode and the cathode. This field transports the ionization electrons produced by a charged particle towards the anode, where they are amplified and collected.

dimension is reconstructed from the timing of the recorded signals. This is possible because the electrons drift at a constant velocity in the detector [32], so the position along the drift direction is directly proportional to the drift time. This is the origin of the “time projection” portion of the detector’s name.

2.1.2 Active targets

The TPC was originally designed as an evolution of bubble chambers for tracking particles in high-energy experiments [32, 42]. To observe nuclear reactions inside a TPC, a sample of target material must be installed within the detector. This sample is traditionally a thin foil of target material or a small amount of target material evaporated onto a thin substrate, but the target can also be the TPC gas itself, creating a so-called *active target* [4]. This design has been used successfully in several recently constructed detectors for nuclear physics applications, some examples of which are described by Beceiro-Novo et al. [4].

The active target design provides a number of advantages over a solid target. The main benefit is that it allows the detection of reactions at low energy with a solid angle coverage close to 4π and without compromising the target thickness, as opposed to a passive target where the thickness has to be reduced enough for the reaction products to escape. Because reactions can occur anywhere within the detector’s active volume, they can be measured over a continuous, broad range of energies as the beam slows down within the gas volume. Since the reaction products emerge from within the tracking medium itself, very low energies can be measured, and the vertex of the reaction can be reconstructed on an event-by-event basis, allowing excitation functions to be measured with a single beam energy.

The active target design imposes some constraints on the choice of gas for the TPC. Not only does the gas have to provide good electron amplification and transport, but it also must contain the target nucleus of interest and, ideally, few other nuclei. For example, the proton scattering experiment described in this thesis required a gas containing hydrogen nuclei. The best gas choice would therefore be pure hydrogen as it has no other nuclei for the beam to scatter off of. However, the electron amplification properties of hydrogen make it hard to work with. Instead, we chose to use isobutane (C_4H_{10}). While isobutane provides better electron amplification, it also requires us to filter out scattering off of carbon nuclei during the analysis.

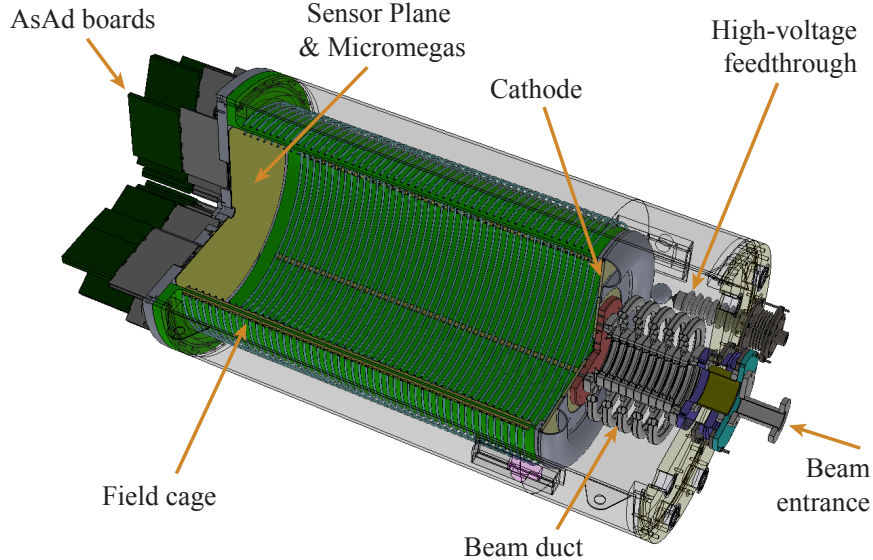


Figure 2.2: A schematic view of the AT-TPC. The outer shielding volume was made transparent in this image to make the details of the inner volume more visible. Beam enters the detector through the beam duct at the right-hand side of the image and moves toward the sensor plane on the left. Some components of the GET electronics are shown mounted on the downstream end of the detector (see Section 2.4).

2.2 Structure of the AT-TPC

The AT-TPC is a newly constructed time projection chamber that uses the active target design described above. Figure 2.2 shows a cutaway view of the detector and all its components. The structure of the TPC is described briefly in this section. A more thorough description of the detector's design can be found in an article published by Suzuki et al. [50] describing a half-scale prototype of the AT-TPC.

2.2.1 Inner and outer gas volumes

The active volume of the AT-TPC is formed by an open-ended cylinder of epoxy-coated fiberglass with length 1 m and radius 28 cm. The upstream end of the volume is sealed with a stainless steel cathode, which has at its center a thin foil window through which the beam enters the detector. The downstream end is closed by an aluminum flange which supports the sensor plane that serves as the anode. This inner volume is filled with the gas that serves as a target.

Surrounding the inner volume is a larger, concentric shielding volume contained by a cylindrical aluminum pressure vessel. The purpose of the shielding volume is to isolate the high electric potential of the cathode from the environment and to prevent arcing. Therefore, the shielding volume is filled with

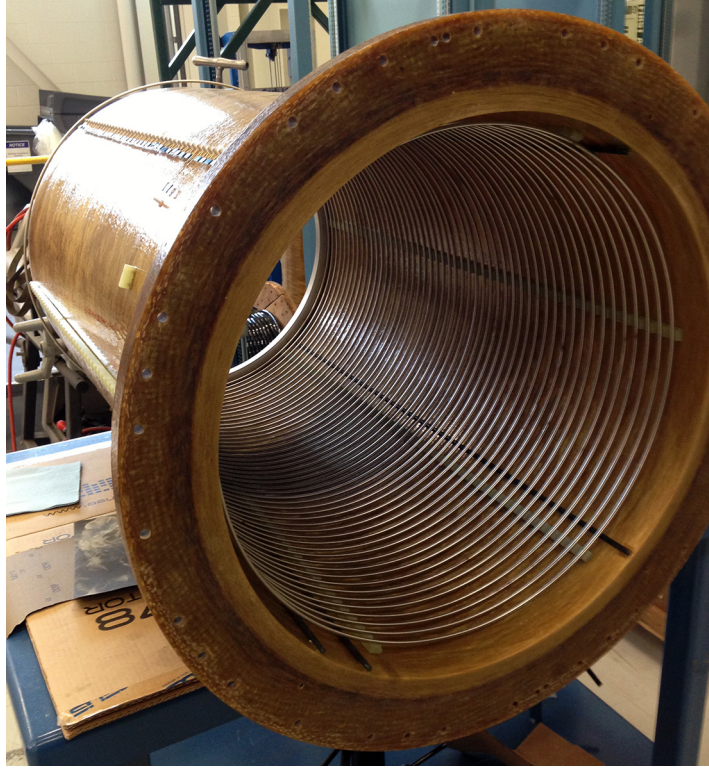


Figure 2.3: A photograph of the inner volume wall with the rings of the inner field cage installed. The outer field cage rings have a larger diameter, but are otherwise identical and are installed on the outer surface of the cylinder.

an inert gas with a high dielectric constant, like nitrogen. The pressure of the shielding volume is kept slightly lower than the pressure in the active volume to ensure that if there were a small leak between the two volumes, the inner volume would not be contaminated with a foreign gas that could affect the electron drift velocity.

2.2.2 Electric and magnetic fields

The active volume contains a uniform electric field which is produced by applying a potential difference between the cathode at its upstream end and the anode at its downstream end. To ensure that the electric field is uniform, the walls of the inner volume are surrounded inside and out by a field cage consisting of concentric ring-shaped electrodes connected by a resistor chain (see Fig. 2.3). The resistor chain gradually steps down the voltage between each ring, ensuring electric field uniformity throughout the volume.

In addition to the electric field, particles in the AT-TPC experience a magnetic field from the large-bore solenoidal magnet that the detector is mounted inside of. This magnet was originally designed for

use in a medical magnetic resonance imaging (MRI) machine, and it is capable of producing a field of up to around 2 T. The AT-TPC is mounted on rails in the center of the magnet. The longitudinal magnetic field bends the trajectories of the emitted charged particles in order to better determine their energies. Another benefit is the ability to track particles over longer paths, and for those that stop in the gas volume, measure their total range.

2.2.3 Sensor plane

Ionization electrons produced inside the AT-TPC are read out by a sensor plane mounted on the anode end of the detector. The sensor plane (or “pad plane”) consists of a circular printed circuit board of radius 27.5 cm covered with 10240 triangular gold-plated conductive pads. The pads are arranged in a hexagonal inner region of small pads with height 0.5 cm surrounded by an outer region of large pads with height 1.0 cm. This layout is shown in Fig. 2.4.

The triangular pad shape was chosen to maximize the spatial resolution of the detector. When a charged particle track crosses a series of adjacent triangular pads, the amount of charge deposited on each pad is staggered. This staggering pattern changes significantly with even a small change in the orientation of a track, leading to a greater sensitivity and an improved angular resolution.

Electron amplification is provided by a Micromegas [19] device installed on the sensor plane. The Micromegas (from “micro-mesh gaseous structure” [27]) consists of a very fine conductive mesh supported approximately 100 μm above the sensor plane by insulating posts. The mesh is biased with respect to the electrodes to create a relatively large electric field between the mesh and the pads. This effectively divides the detector into two regions: a large *drift region* above the mesh and a small *multiplication region* below the mesh. When a charged particle passes through the detector, it ionizes the gas in the drift region. The relatively low electric field in the drift region then transports the electrons toward the mesh. Once the electrons pass through the mesh and enter the multiplication region, the much larger electric field there causes electron avalanches to form, effectively amplifying the single-electron signals to something that can be measured by the electronics. This process is illustrated in Fig. 2.5.

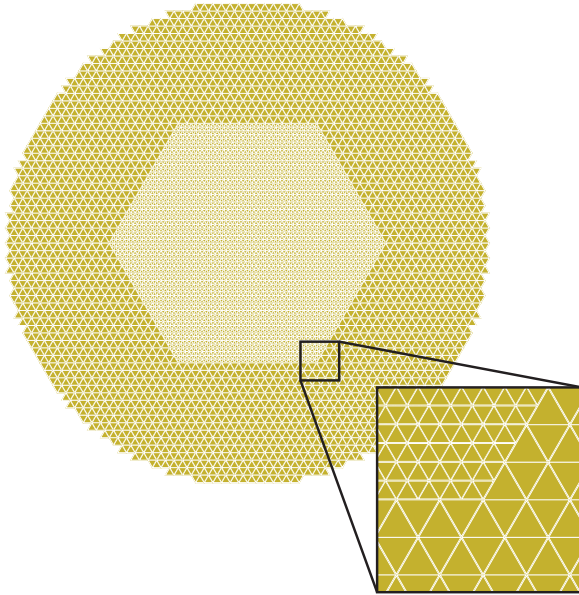


Figure 2.4: Layout of the pad plane. The inset shows a closer view of one corner of the hexagonal inner region. This region of half-scale pads provides finer resolution near the reaction vertex, which will generally occur near the central axis of the detector.

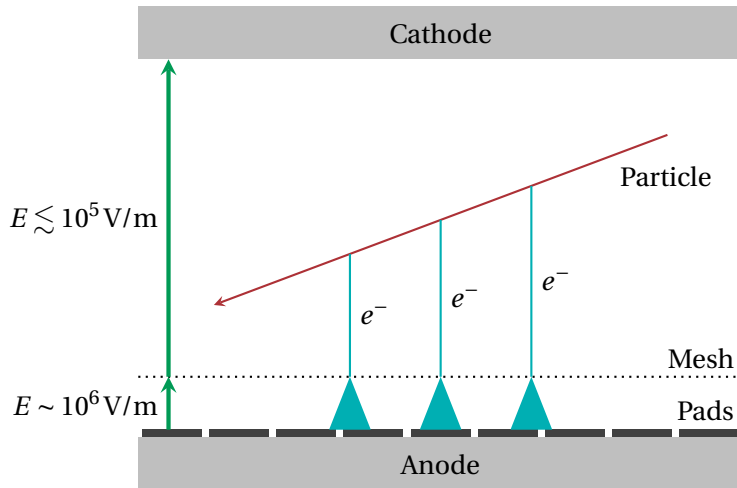


Figure 2.5: Principle of operation of a Micromegas. The electric field magnitudes shown are nominal: the field in the region above the mesh may vary from roughly 10^3 V/m to 10^5 V/m.

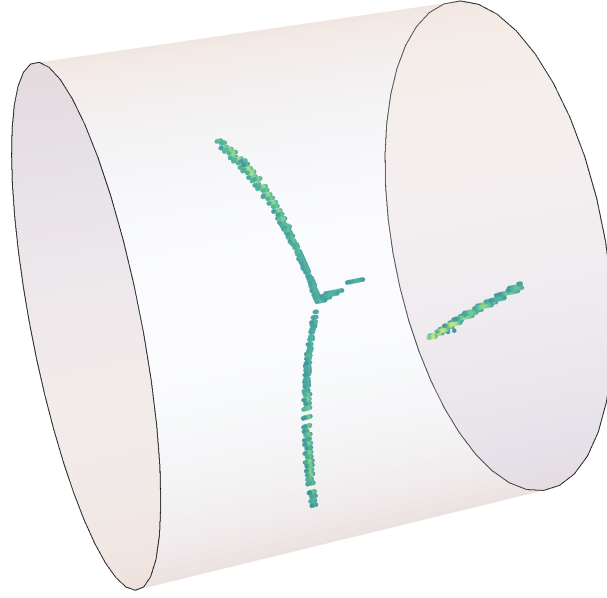


Figure 2.6: Illustration of pileup separation due to the tilt angle. The leftmost track is elastic α - α scattering, and the rightmost track is another α particle that entered the detector during the event. Without the tilt angle, the two beam tracks would be collinear, making them more difficult to separate.

2.3 Tilting the detector

The AT-TPC is normally coaxially centered within the bore of the magnet, but the detector's support carriage has a small jack that allows the anode end of the detector to be raised up to approximately 6° with respect to the axis. Tilting the detector can be advantageous for two reasons. First, the tilt angle projects tracks at very forward angles onto more than one pad, improving measurements at these small scattering angles. Second, it allows some separation of pileup events since earlier beam tracks drift away from the cathode before later ones arrive (see Fig. 2.6).

While tilting the detector solves some problems, it also creates a few complications for the analysis. When tilted, the electric and magnetic fields in the TPC are no longer parallel, but are instead separated by a small angle. This causes the drift electrons to be deflected by a small amount in a direction transverse to the electric field. This has to be corrected for during the track reconstruction process, which will be described in Section 3.2.

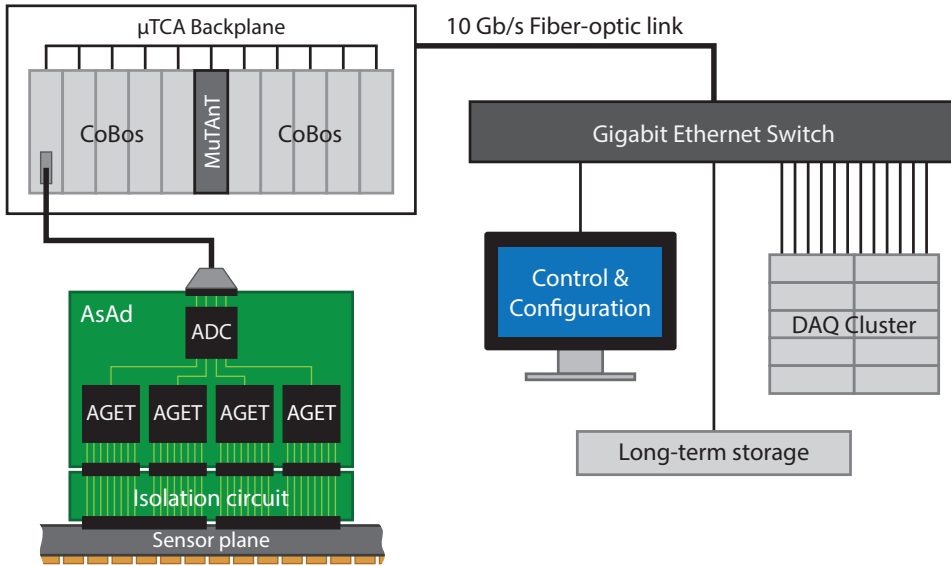


Figure 2.7: A schematic view of the GET electronics system. Only one AsAd is shown for clarity, but 40 AsAd boards are used to instrument the AT-TPC.

2.4 Electronics

The AT-TPC is instrumented with digital electronics developed by the Generic Electronics for TPCs (GET) collaboration [44]. This equipment provides a fully digital data acquisition system capable of digitizing and recording the full trace for each of the 10240 channels in the detector.

The electronics hardware is divided into a hierarchy of several modules (see Fig. 2.7). At the lowest level of the hierarchy is a custom application-specific integrated circuit (ASIC) called the AGET (ASIC for GET). This chip samples and shapes the signals and compares them to a threshold to generate a channel-level trigger. The AGET amplifies the incoming signal with a variable-gain charge-sensitive preamplifier and performs pole-zero correction. It then stores samples of the analog signal in a switched capacitor array (SCA) which acts as a circular buffer [1, 3]. Each AGET can read out 64 physics channels from the detector in addition to 4 fixed-pattern noise channels. The fixed-pattern noise channels are structurally identical to the physics channels, but without inputs [1, 3]. This allows the data to be corrected for low-frequency electronic noise.

The AGETs are mounted in groups of four on AsAd (ASIC Support and Analog to Digital conversion) boards. In addition to the four AGETs, each AsAd board houses a four-channel, 12-bit ADC. When a trigger is issued, the ADC digitizes the sample outputs from each AGET chip and transmits them via a serial

link [3]. Between triggers, the ADC digitizes and transmits the multiplicity signal from each AGET. The input end of each AsAd board is attached to an isolation circuit, and this assembly is then mounted on the downstream end of the TPC and connected directly to the sensor plane (see Fig. 2.8). This design was chosen to minimize the distance that analog signals must travel before being digitized, reducing the capacitance and potential for noise in the data.

The top level of the GET electronics hierarchy is the CoBo (**C**oncentration **B**oard). Each of the AT-TPC's 10 CoBos is connected to four AsAd boards. When a trigger is issued, the CoBo collects the data from these boards, applies an event time stamp, and builds the event [3]. It then sends the event over a 10 Gb/s fiber-optic link to a network switch to be distributed to a cluster of computers for storage.

To keep the CoBos synchronized and generate a global trigger, an additional board called the MuTAnT (**M**ultiplicity, **T**rigger, **A**nd **T**ime) distributes a global time stamp and manages clock synchronization across the system [3]. The MuTAnT board is designed to collect all of the running multiplicities and hit patterns from the CoBos and combine them in various ways to generate a global trigger. The most straightforward method consists of simply summing the multiplicities to generate a trigger when a global threshold is reached. This is referred to as a Level 1 trigger. Other more complex trigger decisions can be used that involve matching a predefined pattern of hit channels (a Level 2 trigger). The choice of which channels contribute to the global multiplicity trigger is set independently for each CoBo; this process will be described in Section 5.2.3.

2.5 Data acquisition

Due to the very large number of channels and high data rate, the AT-TPC requires custom software for data acquisition. The AT-TPC DAQ is a multi-level, distributed system with a controlling master node overseeing a set of 10 worker nodes, one per CoBo. A schematic of the system is shown in Fig. 2.9.

2.5.1 Structure of the DAQ system

Since the DAQ computers must be located next to the AT-TPC in the experimental vault, the DAQ system was designed as a web application that can be opened in a browser on a client computer elsewhere in the laboratory. The core of the software is written in Python 3 using the popular Django web application

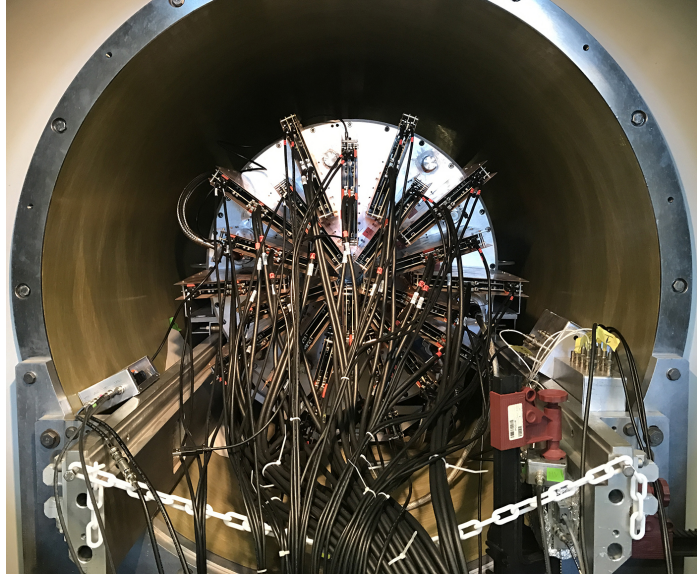


Figure 2.8: A photograph of the fully instrumented AT-TPC mounted inside its solenoid magnet. The 40 AsAd^s are mounted on the downstream end flange surrounded by copper shielding. Individual cables connect each AsAd to its controlling CoBo, and a separate set of cables connects each to its power supply.

framework and the Celery asynchronous task queue. The site is supported by a PostgreSQL database that stores the internal configuration of the system.

The processes for the web servers controlling the DAQ interface are run inside a set of Docker containers. Docker is a containerization platform that allows programs and their associated dependencies to execute independently and without knowing about the rest of the system [12]. This is possible through the use of containers, which are functionally similar to virtual machines but with the key distinction that a container does not contain a full guest operating system. Instead, containers use the Linux kernel of the underlying host's operating system while still providing filesystem isolation and an independent set of system libraries to the contained code. This saves disk space compared to a full virtual machine, but more importantly, code inside a container runs at native speed as it does not have to work through a hypervisor layer. Additionally, since each container has its own full set of system libraries, containerized applications are platform-independent and can run on any operating system that uses the Linux kernel (support is also available for Windows and macOS through a lightweight Linux virtual machine).

In addition to the web application, there are ten separate worker nodes for the DAQ, one for each CoBo. Each of these runs on its own computer. The main reason for running so many independent systems is throughput: with a theoretical maximum¹ data rate of approximately 21 MB/event, the AT-TPC

¹Experimental data rates are much lower since we do not read out channels that were not above threshold.

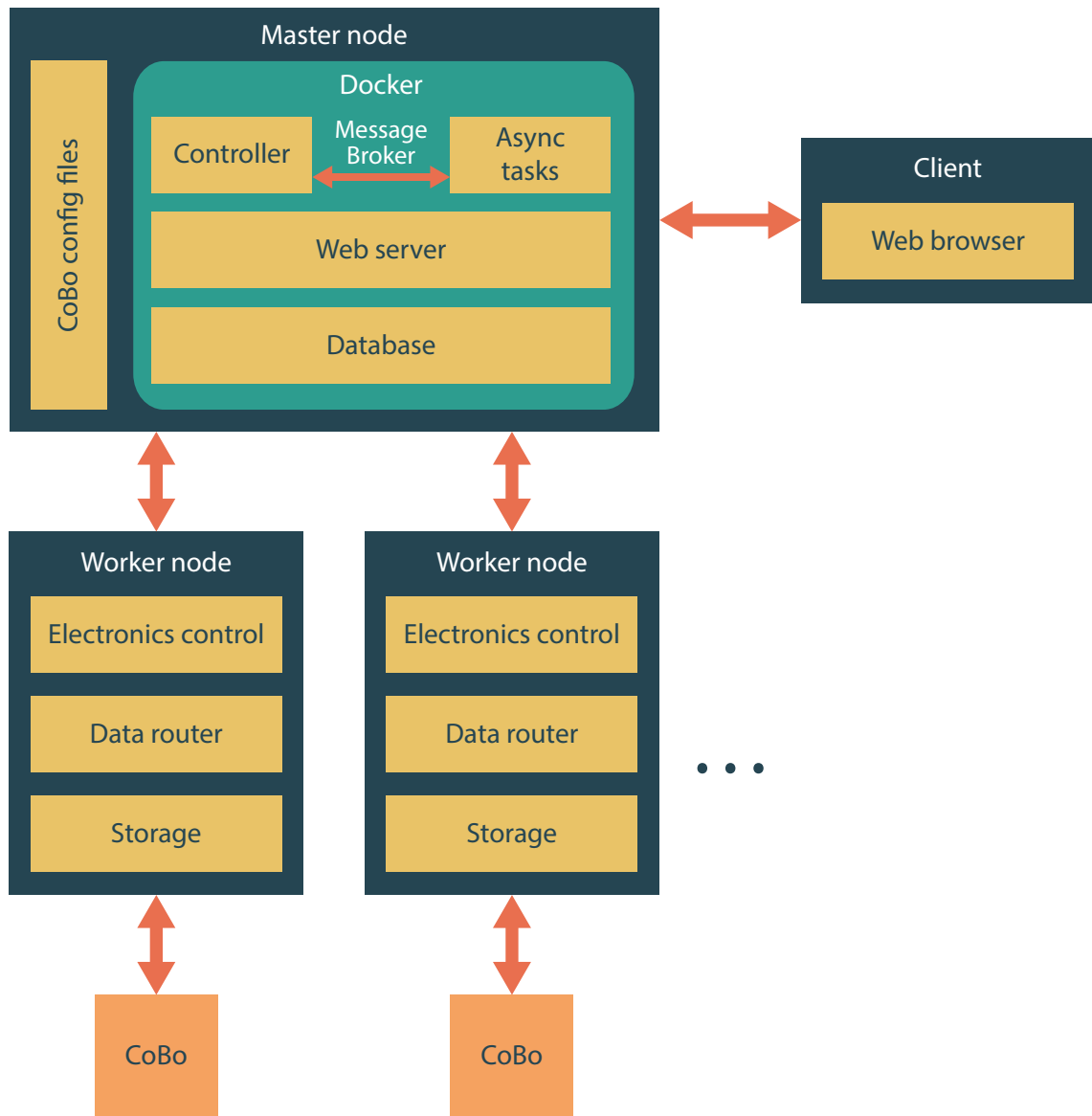


Figure 2.9: Structure of the DAQ system. Only two worker nodes are shown, but there are ten in the actual system.

could easily saturate the throughput of a single mechanical hard drive at an event rate as low as 10 Hz. Using a parallel set of 10 computers allows the rate to be 10 times higher.

Each worker node runs a set of two programs provided by the Institut de recherche sur les lois fondamentales de l'Univers (IRFU) in Saclay, France. The first program, the Electronics Control Core (ECC) server, is responsible for controlling the CoBo. It can configure the CoBo and its connected AsAd boards using a configuration file and start and stop data taking. The second program, the data router, receives the data stream from the CoBo and records it to a file on the local hard disk. At the end of the experiment, the data files from the ten computers are collected and merged together.

CHAPTER 3

ANALYZING AT-TPC DATA

Extracting physics results from the data recorded by the AT-TPC requires a complex, multi-step analysis process. This process involves correcting the electronics signals for baseline fluctuations, reconstructing three-dimensional tracks, separating the tracks from noise, and fitting the tracks using a Monte Carlo algorithm. This chapter contains a general description of the steps of the analysis process and the reasoning behind its design. Specifics of the analysis performed on the ^{46}Ar data are given later in Chapter 5.

3.1 Baseline correction

The signals recorded by the AT-TPC in the $^{46}\text{Ar}(\text{p}, \text{p}')$ experiment feature large-scale baseline fluctuations corresponding to the time that the beam particle was present in the chamber. This happened because the ^{46}Ar nucleus, which is much more ionizing than the protons that the AT-TPC was tuned to measure, deposited enough charge onto the pads it activated on the sensor plane to induce a negative signal in all other pads via capacitive coupling through the mesh. Fortunately, this effect is easy to correct in software. The correction is done using a Fourier transform and a low-pass filter.

One definition of the Fourier transform of a function $f(t)$ is¹

$$\hat{f}(\nu) = \mathcal{F}[f(t)] = \int_{-\infty}^{\infty} f(t) e^{-2\pi i \nu t} dt. \quad (3.1)$$

To correct for the baseline fluctuation, we first calculate the Fourier transform $\hat{f}(\nu)$ of the signal. Then, we multiply $\hat{f}(\nu)$ by $\text{sinc}(\nu/a)$ where

$$\text{sinc } x \equiv \frac{\sin(\pi x)}{\pi x}, \quad (3.2)$$

and a is a constant scaling factor. Finally, we find the inverse Fourier transform of this product. This gives an approximation for the baseline of the signal which can then be subtracted away (see Fig. 3.1).

The sinc function was chosen in order to take advantage of the Convolution Theorem. This theorem states that

$$\mathcal{F}^{-1}[\hat{f}(\nu)\hat{g}(\nu)] = (f * g)(t) = \int_{-\infty}^{\infty} f(\tau)g(t - \tau)d\tau, \quad (3.3)$$

¹This is perhaps not the most common definition in physics, but it is the definition used by the Fast Fourier Transform library used in the analysis [25].

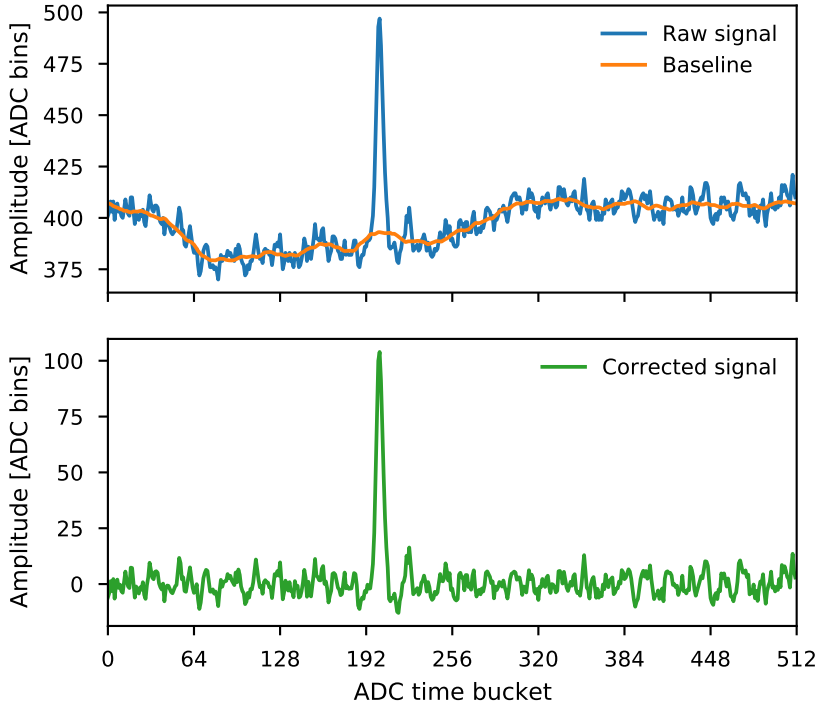


Figure 3.1: Subtracting the baseline from a single signal. The top plot shows the raw signal and the calculated baseline. The bottom plot shows the difference between the two.

where $(f * g)(t)$ denotes the convolution of $f(t)$ and $g(t)$ [31]. Therefore multiplying the transformed signal by $\text{sinc}(v/a)$ and then inverting the transformation is equivalent to convolving the original signal with the inverse transformation of $\text{sinc}(v/a)$. Conveniently, that inverse is

$$\mathcal{F}^{-1}[\text{sinc}(v)] = \text{rect}(t) \equiv \begin{cases} 1, & -\frac{1}{2} < t < \frac{1}{2} \\ 0, & \text{elsewhere,} \end{cases} \quad (3.4)$$

a rectangular window function. This whole procedure is therefore equivalent to convolution with a rectangular window, or a moving average. The Fourier transform was used instead of a simple moving average due to the high speed of modern Fast Fourier Transform (FFT) libraries.

3.2 Track reconstruction

After baseline correction, the next step of the analysis process is to reconstruct three-dimensional tracks from the signals. This entails converting the time-domain signals to a set of discrete points (x_i, y_i, z_i) in three-dimensional space with associated peak amplitudes a_i . The simplest way to do this is to assume

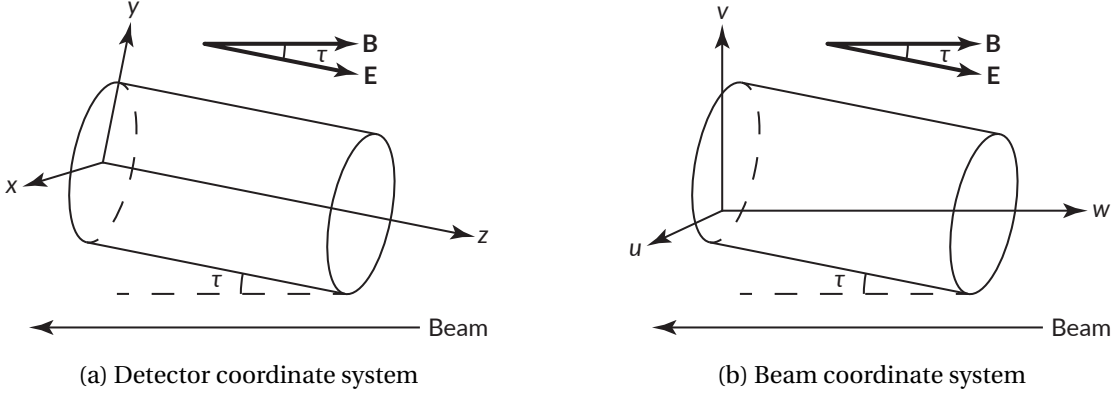


Figure 3.2: Coordinate systems used in the analysis. After calibration, the recorded tracks are in the detector coordinate system (a). This system has its origin in the center of the sensor plane at $z = 0$ with the z axis pointing upstream toward the beam entrance window. The beam coordinate system (b) is related to the detector coordinate system by a rotation through angle τ about the beam entrance window, where τ is the detector tilt angle. In this system, the beam moves along the $-w$ axis. Note that both of these coordinate systems are left-handed.

that each pad is activated only once in a particular event. Then the raw (x, y) coordinates for a particular channel are assumed to be the centroid of the corresponding triangular pad, and the uncalibrated z position is the location of the center of gravity of the peak in the ADC signal. The amplitude of the signal is calculated by subtracting an averaged baseline from the maximum of the peak. This averaged baseline is the mean of the signal in time buckets $N - 20$ through $N - 15$, where N is the location of the maximum of the peak.

At the end of this process, we have a set of 4-tuples (x_i, y_i, z_i, a_i) that describe the position and energy loss of a tracked particle in the detector coordinate system (Fig. 3.2a) at a given moment in time; however, the units of these quantities are not all the same. Since the x and y positions are calculated from the pad plane, they are in distance units, but the z position is still an ADC time bucket index, which is a time unit. A calibration is therefore required to make all of these values compatible with each other.

The calibration is simplest when the electric and magnetic fields are parallel or when there is no magnetic field. In this case, the primary electrons produced in the TPC drift along the electric field lines, which point along the z axis in the detector. Therefore the track's projection onto the pad plane is orthogonal, which implies that the x and y coordinates recovered from this projection equal the true coordinates of the particle track, and the only thing that needs to be calibrated is the z position. Since the uncalibrated z value is in time units, it can be converted to distance units using the electron drift velocity

v_d and the ADC clock frequency ν :

$$z = \frac{v_d z_0}{\nu}. \quad (3.5)$$

The calibration is more complex when the magnetic field is nonzero and the detector is tilted. In this case, the electric and magnetic fields are neither parallel nor perpendicular, so the Lorentz force experienced by the drifting electrons will have components in the transverse x and y directions in addition to the primary z component. This causes the electrons' trajectories to be deflected in the x and y directions, which means that all three coordinates need to be calibrated. This can be done by using a vectorial drift velocity instead of the scalar one used above.

Following the derivation presented by Lohse and Witzeling [32], the motion of an electron with mass m and charge e can be modeled with a Langevin equation of the form

$$m \frac{d\mathbf{v}}{dt} = e(\mathbf{E} + \mathbf{v} \times \mathbf{B}) - \frac{m}{\tau} \mathbf{v}, \quad (3.6)$$

where \mathbf{E} and \mathbf{B} are the electric and magnetic field vectors, \mathbf{v} is the electron's velocity, and τ is the mean time between collisions. This equation admits a steady-state solution

$$\mathbf{v}_D = \frac{\mu E}{1 + \omega^2 \tau^2} [\hat{\mathbf{E}} + \omega \tau (\hat{\mathbf{E}} \times \hat{\mathbf{B}}) + \omega^2 \tau^2 (\hat{\mathbf{E}} \cdot \hat{\mathbf{B}}) \hat{\mathbf{B}}]. \quad (3.7)$$

Here, \mathbf{v}_D is the drift velocity vector, $\omega = eB/m$ is the cyclotron frequency, $\tau = mv_D/eE$ is the mean time between collisions, and $\mu = e\tau/m$ is the electron mobility in the gas. In the detector coordinate system $(\hat{x}, \hat{y}, \hat{z})$ shown in Fig. 3.2a, the electric and magnetic fields are

$$\mathbf{E} = E \hat{z}$$

$$\mathbf{B} = B [\sin(\theta_t) \hat{y} + \cos(\theta_t) \hat{z}]$$

for a tilt angle θ_t , so Eq. (3.7) can be simplified to yield the following components:

$$v_x = \frac{\mu E}{1 + \omega^2 \tau^2} (\omega \tau \sin \theta_t) \quad (3.8)$$

$$v_y = \frac{\mu E}{1 + \omega^2 \tau^2} (\omega^2 \tau^2 \sin \theta_t \cos \theta_t) \quad (3.9)$$

$$v_z = \frac{\mu E}{1 + \omega^2 \tau^2} (1 + \omega^2 \tau^2 \cos^2 \theta_t). \quad (3.10)$$

Since we assumed a constant drift velocity magnitude, the amount of deflection in the x and y directions is proportional to the drift time. Therefore, the data can be calibrated with the equations

$$x = x_0 - \frac{v_x z_0}{v} \quad (3.11)$$

$$y = y_0 - \frac{v_y z_0}{v} \quad (3.12)$$

$$z = \frac{v_z z_0}{v}, \quad (3.13)$$

where v_x , v_y , and v_z are the three components of the drift velocity vector given in Eqs. (3.8) to (3.10).

The final step of track reconstruction is to transform the data from the detector coordinate system xyz of Fig. 3.2a to the beam coordinate system uvw of Fig. 3.2b. The beam is parallel to the w axis in the latter frame, which simplifies the fitting algorithms. This transformation is given by

$$\begin{pmatrix} u \\ v \\ w \end{pmatrix} = \begin{pmatrix} 1 & 0 & 0 \\ 0 & \cos\theta_t & \sin\theta_t \\ 0 & -\sin\theta_t & \cos\theta_t \end{pmatrix} \begin{pmatrix} x \\ y \\ z \end{pmatrix} + \begin{pmatrix} 0 \\ (1 \text{ m}) \tan\theta_t \\ 0 \end{pmatrix}. \quad (3.14)$$

The extra factor added to the v component corrects the vertical offset introduced by rotating about the x axis at $z = 0$ rather than at the beam origin window.

3.3 Noise removal

The reconstructed tracks generally contain some noise points and structures that need to be removed to prevent fits from diverging. There are generally two types of noise present in the events: uncorrelated, random points from channels that were triggered by electronic noise, and correlated structures of points created by cross-talk in the electronics. An example event with both types of noise is shown in Fig. 3.3. The noise is removed by two algorithms that are run in series on each event. First, correlated noise is removed using a method based on the Hough transform [13], and then uncorrelated noise is removed using a nearest-neighbor algorithm. This section begins with a description of the Hough transform algorithm for straight lines and for circles, and then the noise removal algorithms are defined.

3.3.1 Hough transform for lines

The Hough transform is a feature recognition algorithm commonly used in computer vision applications to detect straight lines and simple curves in images [13]. It works by transforming image points into a

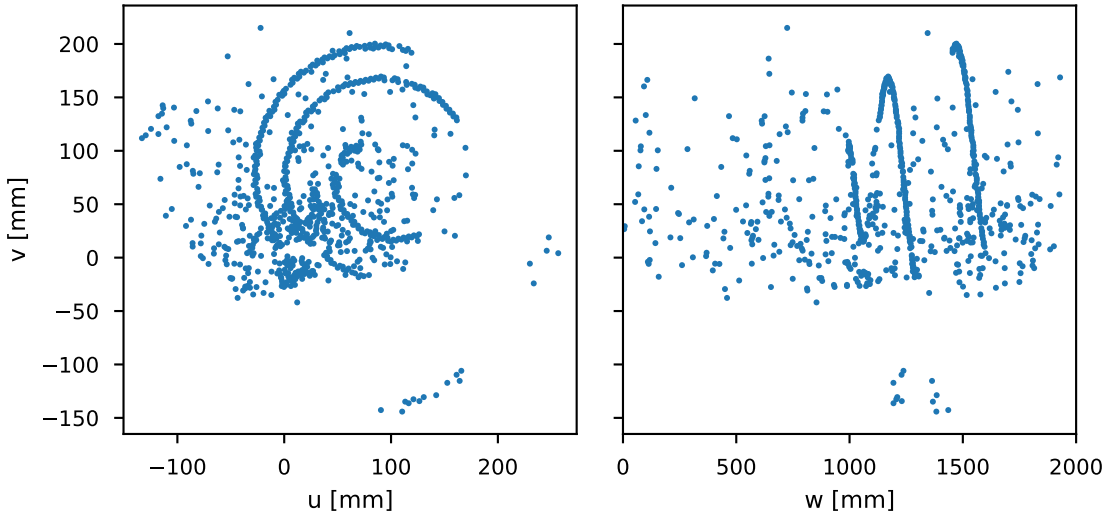


Figure 3.3: Event 99-30 from the ^{46}Ar data set, a particularly noisy event, before cleaning. There are some correlated noise structures present at the bottom of the uv projection and the left of the wv projection, and there is uncorrelated noise throughout the event.

parameter space where the desired image features map onto single points. The features can then be identified by using a peak-finding algorithm in the parameter space.

One way to parameterize a line is in terms of the normal line drawn from it to the origin. This parameterization is given by [13]

$$R = x \cos \theta + y \sin \theta, \quad (3.15)$$

where R is the length of the normal line, and θ is the angle between the normal line and the x axis. This is illustrated in Fig. 3.4. This parameterization implies that each point in the (x, y) system (the *coordinate space*) maps onto a sinusoidal curve $R(\theta)$ in the (θ, R) system (the *Hough space*). Similarly, each line in the coordinate space has a unique parameterization (θ, R) , mapping it onto a single point in the Hough space. Therefore, sets of collinear points in the coordinate space can be found by looking for intersecting curves in the Hough space, as shown in Fig. 3.5.

This process is described more concretely in Algorithm 1. The algorithm computes a discrete set of points (θ_i, R_i) in the Hough space corresponding to the sinusoidal curve generated from each data point. Each of these points is then mapped to the corresponding bin in a two-dimensional accumulator array, which is incremented by 1. After processing each point, lines in the original data are found by looking for peaks in the accumulator array. A large number of collinear points creates a set of sinusoids that intersect at one point, causing the corresponding accumulator bin to hold a large value.

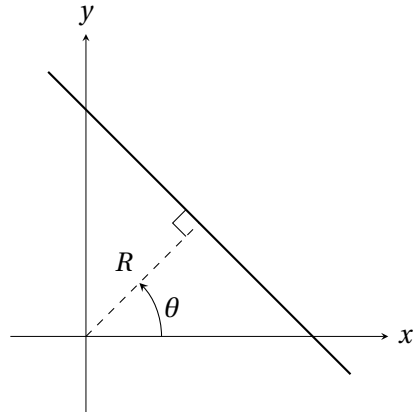


Figure 3.4: Parameterizing a straight line in two dimensions using a normal line drawn to the origin.

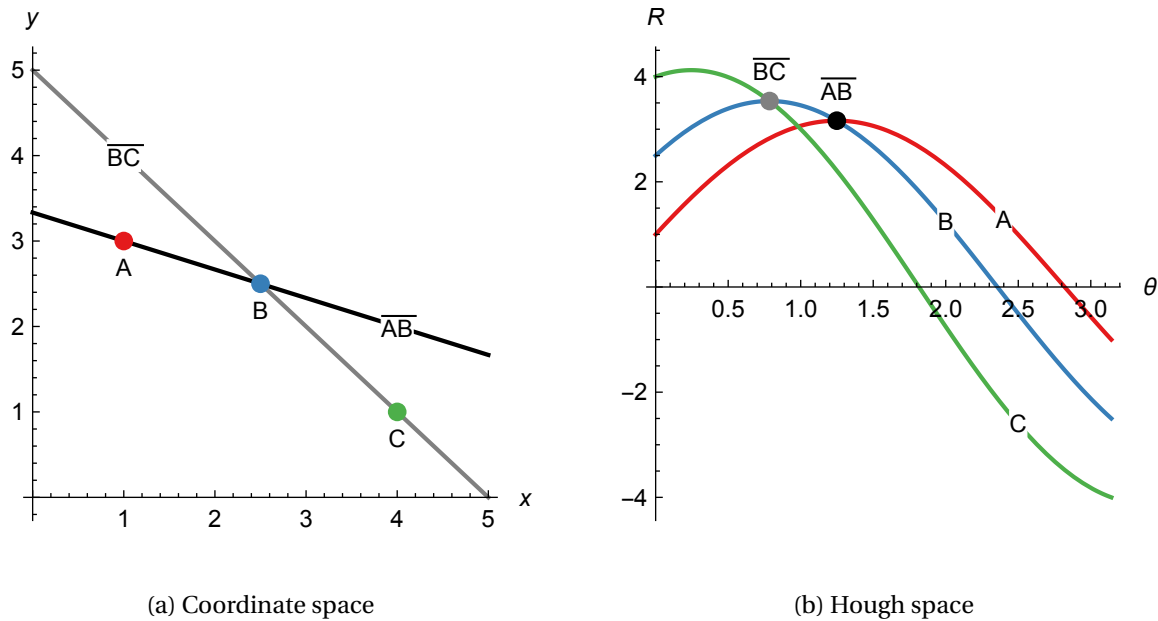


Figure 3.5: Transforming points into the Hough space. The left-hand plot shows three points A , B , and C in the normal coordinate space with lines drawn between them. These points map to sinusoidal curves in the Hough space, as shown in the right-hand plot. Lines in the normal system become points in the Hough space, so a line that passes through two points in the normal space is the intersection of two curves in the Hough space.

Algorithm 1 Hough space binning method

Given: an $N_{\text{bins}} \times N_{\text{bins}}$ accumulator array A , a set of (x, y) data points D , and a maximum bin value M ,
function HOUGHBINS(A, N_{bins}, D, M)
 for $i \in \{0, 1, \dots, N_{\text{bins}} - 1\}$ **do** $\triangleright i$ is the θ bin index
 $\theta \leftarrow i\pi/N_{\text{bins}}$
 for $(x, y) \in D$ **do**
 $R \leftarrow x \cos \theta + y \sin \theta$
 $j \leftarrow \lfloor (R + M)N_{\text{bins}} / (2M) \rfloor$ $\triangleright j$ is the R bin index
 $A_{ij} \leftarrow A_{ij} + 1$ \triangleright Increment the Hough space accumulator array
 end for
 end for
 return A
end function

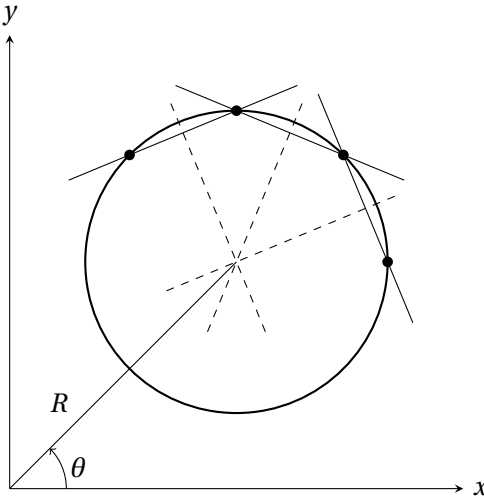


Figure 3.6: Finding the center of a circle using the Hough transform.

3.3.2 Hough transform for circles

Although the process described in Section 3.3.1 is specific to finding lines, a similar process can be used to find circles in an image. This procedure was originally described by Illingworth and Kittler [23], but the formulation shown in this section was taken from Heinze [21].

Consider a set of points lying along a circle. If a line is drawn between any two of the points, a second line can be drawn perpendicular to the first line and passing through its midpoint. This second line will always pass through the center of the circle. Therefore, given a set of points, we can find the center of curvature by finding the point where all of these perpendicular bisectors intersect (see Fig. 3.6). We can do this using the Hough transform.

Given two points on the circle (x_0, y_0) and (x_1, y_1) , the midpoint between the two points is

$$x_m = \frac{x_0 + x_1}{2}; \quad y_m = \frac{y_0 + y_1}{2}. \quad (3.16)$$

The slope of the perpendicular bisector to the line between these two points is

$$m = \frac{x_1 - x_0}{y_0 - y_1}, \quad (3.17)$$

and the y -intercept is

$$b = y_m - mx_m. \quad (3.18)$$

These can be plugged into the formula for a line $y = mx + b$ and simplified to give

$$y = \frac{x_1 - x_0}{y_0 - y_1} x + \frac{(y_1^2 - y_0^2) + (x_1^2 - x_0^2)}{2(y_1 - y_0)}. \quad (3.19)$$

This describes the set of possible locations of the center of the circle. To make the calculation easier, we can transform this to polar coordinates:

$$x = R \cos(\theta) \quad (3.20)$$

$$y = R \sin(\theta). \quad (3.21)$$

Then, we can rewrite Eq. (3.19) as

$$R = \frac{(x_1^2 - x_0^2) + (y_1^2 - y_0^2)}{2[(x_1 - x_0) \cos \theta + (y_1 - y_0) \sin \theta]}. \quad (3.22)$$

This equation can then replace the line $R \leftarrow x \cos \theta + y \sin \theta$ in Algorithm 1 to make a Hough transform function that finds the center of a circle of points.

3.3.3 Removing correlated noise

The two Hough transform algorithms described above are used to remove correlated noise points from the recorded events. This process proceeds as follows:

1. Find the coordinates (u_c, v_c) of the center of curvature of the event using the Hough transform for circles (Section 3.3.2).

2. Calculate the arc length coordinate for each data point as a function of w . The arc length coordinate for each point is defined as

$$s = \rho\phi \quad (3.23)$$

where

$$\rho = \sqrt{(u - u_c)^2 + (v - v_c)^2} \quad \text{and} \quad \phi = \tan^{-1}\left(\frac{v - v_c}{u - u_c}\right). \quad (3.24)$$

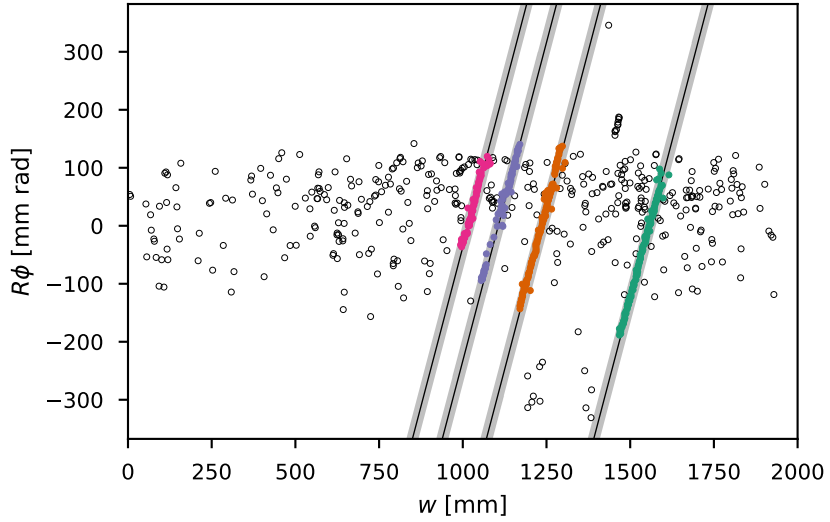
This parameterization is used because the arc length swept by the particle increases monotonically as a function of w due to the constant polar angle θ of the particle's momentum vector.

3. Perform the Hough transform for lines (Section 3.3.1) on the $\rho\phi$ vs. w projection of the data.
4. Extract the top five peaks from the Hough space and average their angle values together to find the angle of maximum activation in the Hough space. (This takes advantage of the fact that the lines we are searching for in the $\rho\phi$ vs. w space should be parallel.) Take an angular slice of the Hough space around this maximum value and look for peaks in the 1D projection of this slice onto the R axis. These peaks correspond to individual lines in the original space.
5. Determine which of the lines each data point is closest to. If a point is more than some threshold distance from any line, it is discarded as noise.
6. Finally, check how many points are assigned to each line. If any line has less than some threshold number of points, the points assigned to that line are discarded as noise.

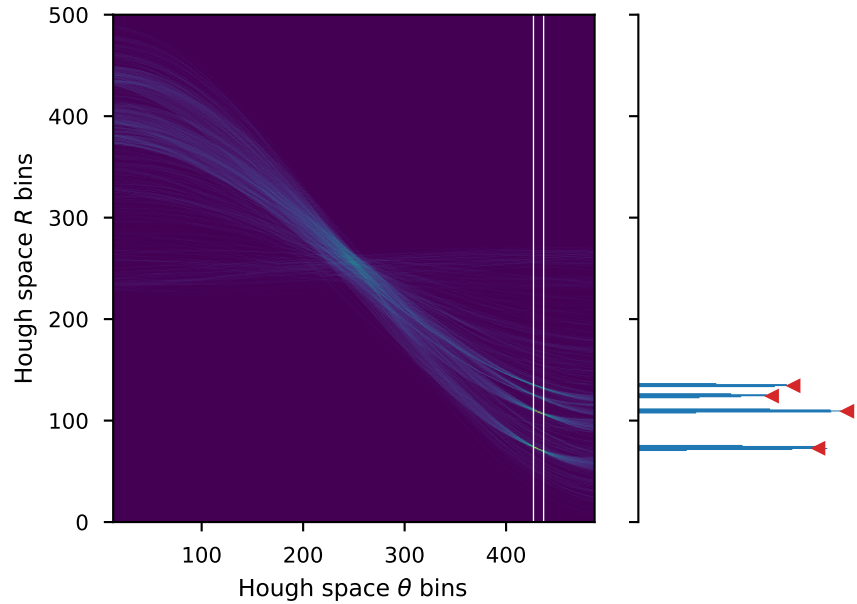
The results of this process for one event are shown in Fig. 3.7.

3.3.4 Removing uncorrelated noise

Random, uncorrelated noise points that are left after the Hough transform-based cleaning are removed by counting the number of neighbors each point has and eliminating points with too few neighbors inside a given radius. We use a naïve algorithm to find the neighbor counts which simply calculates the pairwise distance between each unique set of points in the data set and increments a counter if the distance is small enough. This is shown in detail in Algorithm 2. This method is probably not the most efficient choice, but it runs fast enough for our purposes.



(a) Classification of data points



(b) Hough space with angular slice

Figure 3.7: Cleaning an event with the Hough transforms. Plot (a) shows the data from Fig. 3.3 in the $\rho\phi$ vs w space with the found lines. The colored points are classified as data, while the empty points are noise. Plot (b) shows the Hough space calculated for this data. The maximum angular slice is shown between the two white lines, and the 1D projection of this slice is shown on the right with the peak locations marked.

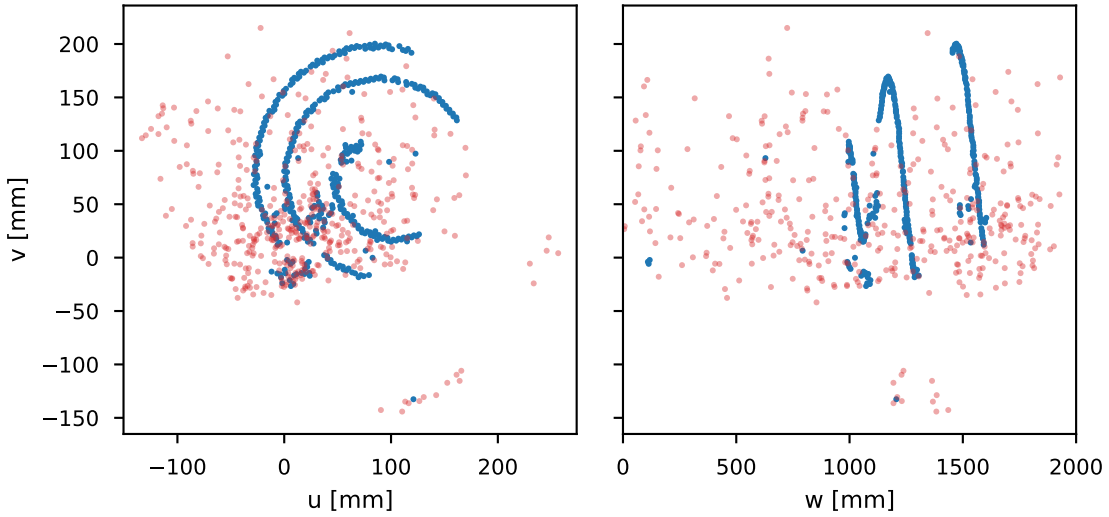


Figure 3.8: Final results of the noise removal process on the event shown in Fig. 3.3. The blue points were kept, and the semi-transparent red points were removed as noise. Some noise is still present after cleaning, but much of it was removed.

After running both noise removal procedures, much of the noise in the event is removed (see Fig. 3.8). The remaining noise is often focused in the first or last few time buckets of the event, and can sometimes be removed with a simple cut. Regardless, the level of noise remaining after this process seems to be small enough that it does not affect the Monte Carlo fits too much.

Algorithm 2 Counting nearest neighbors inside a radius

Given data $X \in \mathbb{R}^{N \times M}$, with number of data points N and number of dimensions M , and maximum neighborhood radius r_{\max} ,

function NEIGHBORCOUNT(X, r_{\max})

let $A \in \mathbb{Z}^N$ contain the neighbor counts initialized to -1 to negate self-counting

for $i \in \{0, 1, \dots, N - 1\}$ do

for $j \in \{0, 1, \dots, i - 1\}$ do

$r^2 \leftarrow \sum_{k=0}^{M-1} (X_{ik} - X_{jk})^2$

if $r^2 < r_{\max}^2$ then

$A_i \leftarrow A_i + 1$

end if

end if

end for

end for

return A

end function

3.4 Modeling tracks and fits

The result of the noise removal process is a set of data points that describe the track as a series of three-dimensional locations with associated signal amplitudes. A model must be fit to this track in order to extract physical observables like the scattering angle or the energy of the beam particle at the vertex. This fit is performed using a Monte Carlo-based optimization algorithm, which will be discussed at the end of this section.

Note that in the remainder of this chapter, the coordinates of the particle will be referred to using the variables x , y , and z rather than u , v , and w . Regardless of the notation, this should be understood as a position in the beam coordinate system shown in Fig. 3.2b.

3.4.1 Track representation and generation

Particle tracks in the AT-TPC can be uniquely described by a set of six parameters that define the initial state of the tracked particle. These parameters are the particle's initial position (x_0, y_0, z_0) , its initial kinetic energy E_0 , and the azimuthal angle ϕ_0 and polar angle θ_0 defining the orientation of its initial momentum vector in spherical coordinates. The azimuthal angle is measured with respect to the x axis of the detector, and the polar angle is measured with respect to the z axis.

Given this set of parameters, a particle track can be modeled by simulating the motion of the particle in the TPC under ideal conditions. The simulation is iterative, beginning with the set of initial coordinates described above. At each time step, it updates the position, momentum, and energy of the particle after applying the Lorentz force. The updated energy is used to calculate the amount of energy lost to interactions with gas atoms or molecules during that time step, and this energy loss is subtracted from the updated energy. Finally, if the particle's energy has reached zero, the simulation is stopped.

Ideally, it would be more convenient to model tracks with a mathematical function rather than a simulation; however, the nature of the AT-TPC makes this impossible. The particle tracks that the detector produces are essentially helical, but the radius of curvature of the helices decreases in a complex way that depends on the energy loss function, a Bragg curve. This prevents us from using an analytic function to describe the tracks.

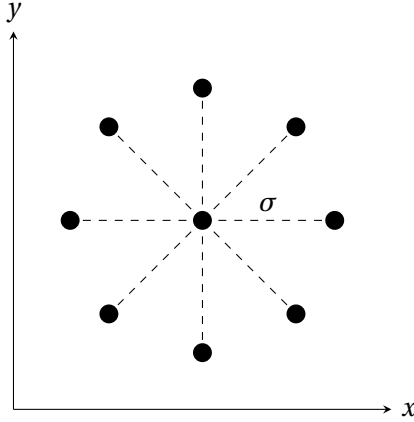


Figure 3.9: Template used to simulate diffusion. The charge q from the initial point is distributed among the diffused points. The central point gets $0.4q$ units of charge, and the outer points each get $0.6q/8$ units of charge. This is based on a two-dimensional normal distribution.

3.4.2 Simulated diffusion and track projection

The simulated track represents the path the particle followed through the inner volume of the TPC. To perform the fit, we also need to calculate the distribution of charge deposition on the pad plane, or the *hit pattern*. This is done in two phases.

First, we simulate electron diffusion. As electrons drift toward the end of the detector, the electron cloud spreads out laterally and attains a final width of

$$\sigma = \sqrt{2Dt}, \quad (3.25)$$

where t is the total drift time (which is directly proportional to z), and D is a constant that is determined empirically [27]. Diffusion is estimated by splitting each simulated track point into nine diffused points based on the template shown in Fig. 3.9.

Each of the diffused points is then projected onto the readout plane at $z = 0$ using the inverses of Eqs. (3.11) to (3.13), which were used to calibrate the track. A fine-grained two-dimensional lookup table is used to map simulated points to channels in the electronics. The charge associated with each point is then used to simulate a pulse in the appropriate channel, and this pulse is accumulated into an event-wide signal for that channel. The pulses are generated with the equation

$$f(q, t) = A(q) \left(\frac{t}{s} \right)^3 e^{-3(t/s)} \sin\left(\frac{t}{s}\right) \quad (3.26)$$

with shaping time s and amplitude

$$A(q) = \frac{G_\mu q}{G_{\text{elec.}} N_{\text{ADC}} C_{\text{norm}}}, \quad (3.27)$$

where G_μ is the gain of the Micromegas, $G_{\text{elec.}}$ is the gain of the GET electronics, q is the amount of charge deposited by this point, N_{ADC} is the total number of ADC bins, and C_{norm} is a normalization factor given by

$$C_{\text{norm}} = \max \left[\frac{f(q, t)}{A(q)} \right] = \max \left[\left(\frac{t}{s} \right)^3 e^{-3(t/s)} \sin \left(\frac{t}{s} \right) \right] = 0.044. \quad (3.28)$$

After all of the points are simulated, the peak amplitude is found in each channel to directly compare to the experimental data.

3.4.3 The objective function

To compare data to the model, we need an objective function that describes how well the modeled track fits the data. The objective function contains three contributions: one from the particle's position, one from its energy loss, and one that helps constrain its vertex location.

The position component of the objective function is a simple least-squares comparison between the modeled track and the experimentally measured track. The modeled track's x and y components are linearly interpolated as a function of z to give continuous functions $\tilde{x}(z)$ and $\tilde{y}(z)$. These functions are then evaluated at each of the experimental track's z positions and compared to the experimental x and y values. This gives the expression

$$\chi^2_{\text{pos}} = \frac{1}{N} \sum_{i=0}^N \frac{[\tilde{x}(z_i) - x_i]^2 + [\tilde{y}(z_i) - y_i]^2}{\sigma_{\text{pos}}^2} \quad (3.29)$$

where N is the number of data points in the experimental track, and σ_{pos} is an expected deviation. We chose σ_{pos} to be 0.5 cm based on the average size of the pads.

The energy component of the objective function is produced by projecting each generated track onto the pad plane and comparing the resulting hit pattern to the experimental hit pattern. This gives a function of the form

$$\chi^2_{\text{en}} = \frac{1}{N_{\text{hit}} \text{ hit pads}} \sum \frac{\Delta A^2}{\sigma_{\text{en}}^2}. \quad (3.30)$$

Here A represents the total charge deposited in a particular pad. The estimated uncertainty σ_{en} was chosen to be 10 % of the maximum value of A present in the experimental track. The sum is taken over all pads that were hit by the experimental track, and N_{hit} is the number of such pads. Limiting the sum to pads present in the experimentally measured event helps the fit converge when parts of the track are missing since otherwise χ^2_{en} would have an unbalanced contribution from all the pads that are present in the generated track but not the experimental one.

The final component of the objective function helps constrain the reaction vertex to be near the z axis. Normally, we could fit the beam track and ensure that the beam track and the track of the scattered particle intersect, but in the ^{46}Ar data set, the beam tracks were not usable (see Section 5.3.5 for details). This can be addressed by adding the following extra term to the objective function:

$$\chi_{\text{vert}}^2 = \frac{x_0^2 + y_0^2}{\sigma_{\text{vert}}^2}. \quad (3.31)$$

This is a simple quadratic constraint on the (x, y) location of the vertex that imposes a penalty on the fit if the vertex is not near the axis. One problem with this approach is that it assumes that the beam is exactly along the z axis, which it might not be due to emittance; however, the emittance of the beam seems to be small enough that this approximation is acceptable.

The complete objective function is, then, the sum of Eqs. (3.29), (3.30), and (3.31):

$$\chi^2 = \chi_{\text{pos}}^2 + \chi_{\text{en}}^2 + \chi_{\text{vert}}^2. \quad (3.32)$$

3.4.4 Finding initial parameter values for optimization

The optimization algorithm must be given a starting point before it can begin generating candidate tracks. The starting point is found using a simple linear fit. In Section 3.3.3, we found that the arc length coordinate $s = \rho\theta$ can be plotted as a function of the z coordinate to get a straight line. This was also shown in Fig. 3.7a. This technique can also be used to get a seed for the Monte Carlo algorithm.

To find the seed, we can use the previously found center of curvature to find ρ and ϕ using the equations in Eq. (3.24). This time, however, we subtract the angular coordinate of the first point in the track to make ϕ start at 0. ρ and ϕ are then multiplied together to get the arc length coordinate s , and a line is fit to the plot of s vs z . The slope of this line defines the initial polar angle θ_0 of the track, and the intercept of the line defines the z_0 position of the reaction vertex.

The initial energy of the particle is calculated from the radius of curvature. In a magnetic field B , a charged particle with transverse velocity v , mass m and charge q will move in a circle of radius

$$\rho = \frac{mv}{Bq}. \quad (3.33)$$

This particle's kinetic energy is, of course,

$$E = \frac{1}{2}mv^2. \quad (3.34)$$

Combining these yields

$$E = \frac{B^2 \rho^2 q^2}{2m} = \frac{B^2 \rho^2 Z^2 e^2}{2Am_p}, \quad (3.35)$$

where A and Z are the mass and charge number of the particle. This can be used to find an estimate for the initial energy E_0 , assuming we know the identity of the particle.

Finally, the remaining coordinates x_0 and y_0 are assumed to be zero since the data calibration procedure places the beam along the z axis.

3.5 The Monte Carlo optimizer

3.5.1 Description of algorithm

Tracks from the AT-TPC can be fit using a simple Monte Carlo algorithm. The algorithm starts with the seed point found above. Then, it generates a large number T of candidate parameter sets from a uniform distribution over the six-dimensional $(x_0, y_0, z_0, E_0, \phi_0, \theta_0)$ parameter space. The distribution is centered on the seed point in each dimension, and the width is set to a configurable value. Each of these candidate tracks is then simulated, and the values of χ^2 are calculated using the equations in Section 3.4.3. The track with the lowest value of χ^2 is selected, and the parameter space is re-centered around this new point before being compressed in each dimension by a multiplicative reduction factor R . This process is then repeated for a fixed number of iterations I . At the end of the I iterations, the best track is accepted as the fit result. Figure 3.10 shows how the parameter space converges to a solution across the iterations of this algorithm.

From the description of this algorithm, it should be apparent that this is not the most efficient way to fit a track. For each event in the data, the computer has to essentially guess the answer $N = IT$ times and pick the best result. Fortunately, the convergence of the size of the parameter space helps the algorithm move toward a solution, and it prevents it from generating candidate tracks that are too far from the minimum. Furthermore, although generating such a large number of tracks is certainly computationally costly, modern high-performance computers and parallel programming techniques help reduce the runtime to something reasonable.

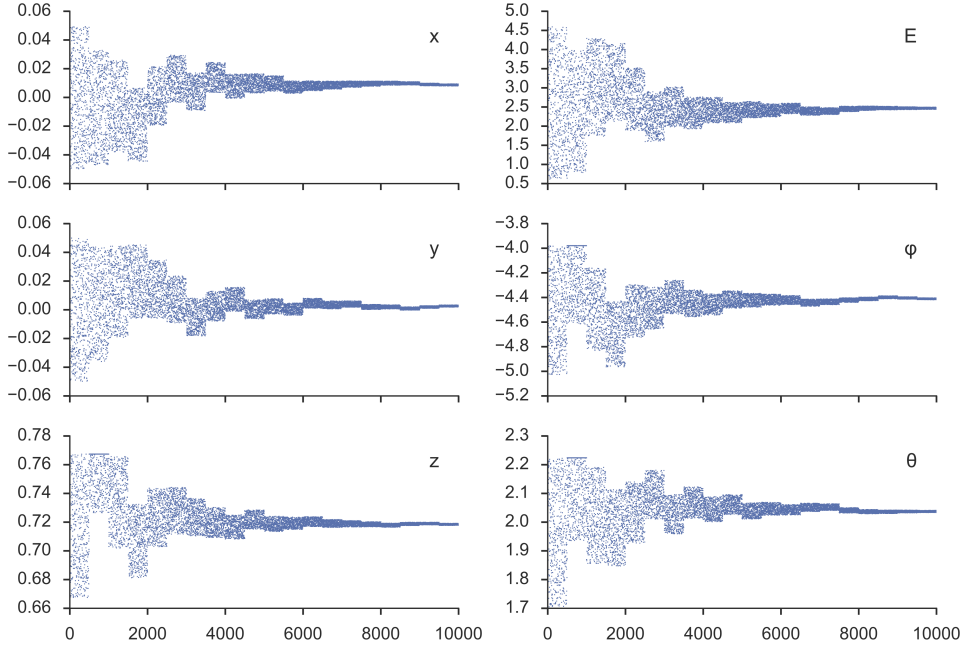


Figure 3.10: Samples drawn by the Monte Carlo algorithm while fitting one event. The horizontal axes represent the sample number, while the vertical axes represent the value of each of the 6 variables. x , y , and z are given in meters, E is in MeV, and θ and ϕ are in radians. Each 500-sample iteration of the code is visible as a large-scale block in this plot.

3.5.2 Checking convergence

The Monte Carlo algorithm described above does not include an explicit test for convergence, so the parameters of the fitter must be chosen in such a way that convergence is likely. There are three main parameters that control the convergence of the fit: the number of candidate tracks T generated per iteration, the number of iterations I , and the reduction factor R by which the parameter space is compressed after each iteration.

The values of T and R must be chosen carefully to prevent the fitter from converging to local minima. Much like in the process of simulated annealing, it is important to reduce the size of the parameter space very slowly and to sample as many points in the space as possible on each iteration. The main limitation on T is the available computing power, and the value of R must be balanced with the value of I to control the width of the parameter space at the end of the fit.

If the parameter space has a width ΔX_0 along dimension X at the beginning of the fit, the final width in that dimension will be

$$\Delta X = (\Delta X_0) R^I. \quad (3.36)$$

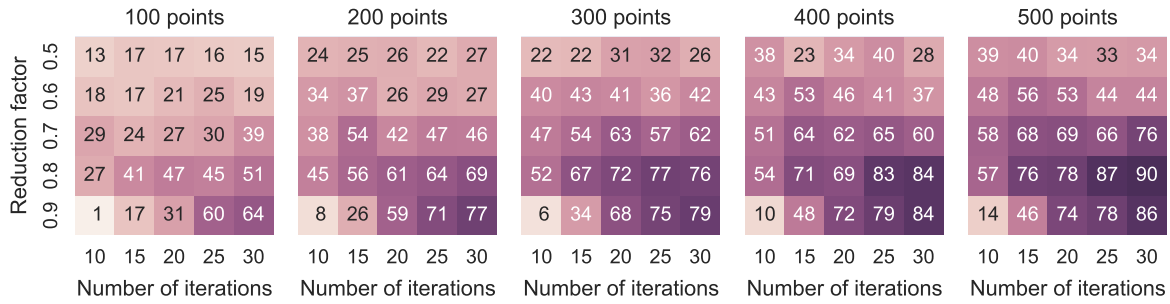


Figure 3.11: Results of the Monte Carlo convergence study. Subplots represent different numbers of points T per iteration. Within each plot, rows represent the reduction factor R , and columns represent the number of iterations I . The number in each cell represents the percentage of fits in which the optimizer converged to the correct minimum, subject to a tolerance of 10 mm in each dimension for the vertex position, 100 keV for the initial proton energy, 5° for the azimuthal angle, and 2° for the scattering angle. The fit was run 1000 times on the same simulated track for each set of parameters.

I	T	R	$\sigma_{x,y,z}$	σ_E	σ_ϕ	σ_θ
20	500	0.8	0.1 m	4.0 MeV	60°	30°

Table 3.1: Monte Carlo fit parameters I , T , and R and initial parameter space widths σ used in the $^{46}\text{Ar}(\text{p},\text{p}')$ measurement.

This gives an estimate for the uncertainty of the fit result in each dimension. This final uncertainty can be reduced by either using a larger value of I or a smaller value of R .

The values of these parameters can be optimized by fitting one event repeatedly and examining the distribution of the fit results. The fit parameters can then be varied to find the best choices. This was done for the $^{46}\text{Ar}(\text{p},\text{p}')$ data set by simulating one proton track and then fitting it 1000 times for various combinations of parameters. The results of this study are shown in Fig. 3.11, and the parameters used in the analysis are shown in Table 3.1.

3.6 Alternative fitting algorithms

Several other minimization algorithms were considered in addition to the Monte Carlo optimizer described above. Although each of these techniques has some advantages, the naïve Monte Carlo algorithm ultimately produced the best, most consistent results. For completeness, a few of the other algorithms we tried are described in this section.

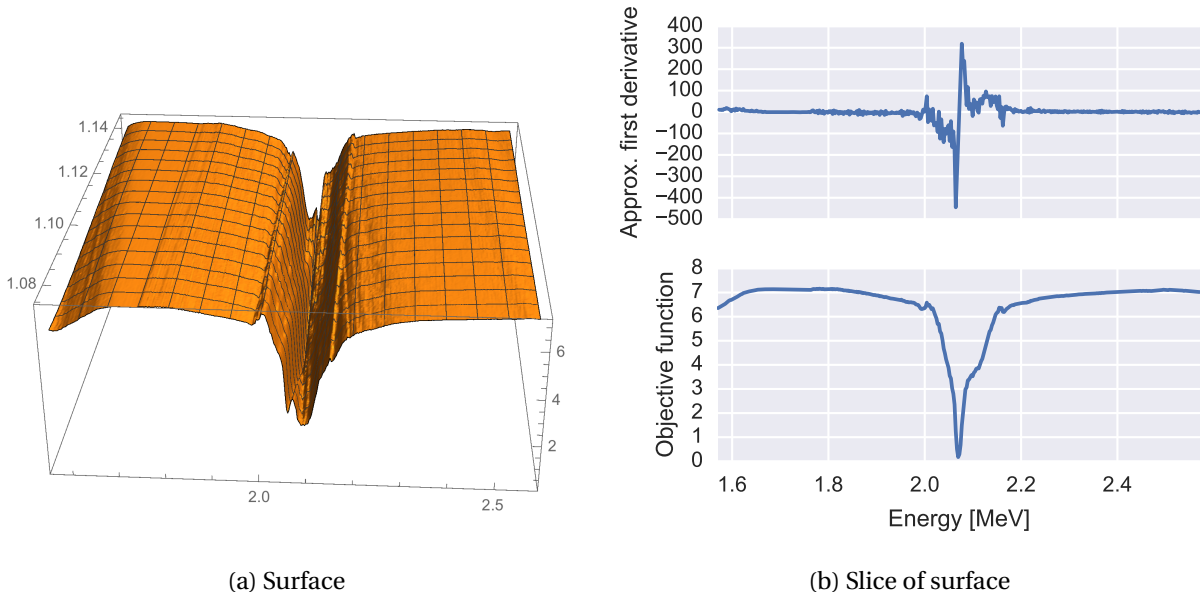


Figure 3.12: Simulated two-dimensional error surface and a one-dimensional slice through that surface. These were generated from a simulated $^{46}\text{Ar}(p, p')$ scattering event by varying the scattered proton's initial energy and scattering angle, calculating the objective function at each point. 400 points were simulated in each dimension. On the surface plot, the horizontal axis represents energy in MeV, the vertical axis represents the energy component of the objective function, and the axis going into the page represents the scattering angle in radians.

3.6.1 Gradient-based methods

The default first approach to an optimization problem is often to use a gradient-based technique. These algorithms are generally robust and computationally efficient [28], and commonly used software libraries like SciPy [25] and MINUIT [24] implement a variety of these algorithms for easy use. However, these techniques are not well-suited to the problem of fitting tracks in the AT-TPC since smooth derivatives are not available for our objective function.

As described previously, the value of the objective function for a given set of track parameters is found by simulating a track in the AT-TPC and projecting it onto the pad plane. This produces an objective function that is not smooth when examined closely, which causes derivatives calculated using the finite differences method to diverge.

Kolda et al. [28] state that *simulation-based* optimization problems like ours often produce objective functions that are nonsmooth and sometimes discontinuous. They name conditional branching (if/then/else constructs), convergence tests, adaptive algorithms, and loss of numerical precision as a few common causes of nonsmoothness in simulation-based problems. They also point out that the com-

Algorithm 3 Basic compass search algorithm [28]

Given a function $f : \mathbb{R}^n \rightarrow \mathbb{R}$, an initial guess $x_0 \in \mathbb{R}^n$, a tolerance Δ_{tol} for determining convergence, and an initial value $\Delta_0 > \Delta_{\text{tol}}$ for the step-length control parameter,

function COMPASS($f, x_0, \Delta_{\text{tol}}, \Delta_0$)

for $k = 1, 2, 3, \dots$ **do**

$D_{\oplus} \leftarrow \{\pm e_i | i = 1, 2, \dots, n\}$, the set of unit vectors spanning \mathbb{R}^n

if there exists a $d_k \in D_{\oplus}$ such that $f(x_k + \Delta_k d_k) < f(x_k)$ **then**

$x_{k+1} \leftarrow x_k + \Delta_k d_k$ ▷ Take step in best direction

$\Delta_{k+1} \leftarrow \Delta_k$ ▷ No change to step size

else

$x_{k+1} \leftarrow x_k$ ▷ No step is taken

$\Delta_{k+1} \leftarrow \frac{1}{2} \Delta_k$ ▷ Shrink step size

if $\Delta_{k+1} < \Delta_{\text{tol}}$ **then**

return x_{k+1}

end if

end if

end for

end function

plexity of the simulation code often makes it difficult or impossible to find an analytic representation of the derivative, even when automatic differentiation libraries are available.

Figure 3.12 shows the energy component of the objective function evaluated for a simulated event as a function of energy and scattering angle. The surface shown in Fig. 3.12a is quite rough when examined on a fine scale. This is more apparent in Fig. 3.12b, which shows a slice taken through the error surface at the scattering angle that corresponds to the minimum. The derivative of this slice with respect to energy, as estimated by finite differences, is very rough and contains abrupt jumps. This would cause problems for any gradient-based optimization technique.

3.6.2 Compass search

Kolda et al. [28] describe an early, basic optimization algorithm for nonsmooth functions that they call *compass search*. This technique, which is described fully in Algorithm 3, evaluates the objective function at a given initial point and then searches along a set of direction vectors for a better point. If a better point is found, the fitter moves to that point. If no better point is found, the fitter shrinks its step size to prevent it from stepping over the minimum.

One problem with this algorithm is that it is very slow to converge if the direction from the initial point to the minimum is not along one of the unit vectors e_i . In this case, the fitter will “bounce” between

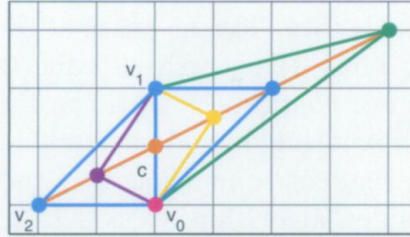


Figure 3.13: An illustration of the points tested in the Nelder-Mead simplex method. The vertex v_2 is reflected across the point c using four different values of the multiplicative factor α , leading to the four possible new vertices, shown in purple, yellow, blue, and green. (Reproduced from [28, Fig. 4.2(b)].)

two of the directions in a zig-zag pattern, evaluating the objective function, which might be computationally expensive, many more times than it needs to. This could be corrected by allowing the fitter to try a linear combination of direction vectors and add this new direction vector to the set of e_i for later iterations, but this causes the set of e_i to contain more vectors than are needed to span the parameter space \mathbb{R}^n , which also leads to inefficiency.

3.6.3 Nelder-Mead simplex algorithm

A more sophisticated option that is similar to the compass search described above is a simplex method, such as the algorithm described by Nelder and Mead [39]. In this method, rather than evaluating the objective function along a set of directions e_i from the initial point, as in the compass search, the function is evaluated at the vertices of a *simplex* of $n + 1$ points in \mathbb{R}^n . For example, in two-dimensional space \mathbb{R}^2 , the function is evaluated at the vertices of a triangle (a set of $n+1 = 3$ points). On each iteration, the vertex with the largest value of the objective function is reflected across the center of the opposite face of the simplex, $c = \frac{1}{n}(v_0 + v_1 + \dots + v_n)$ [28]. The function is then evaluated at a series of points $v_r = v_i + \alpha(c - v_n)$ for a predetermined set of values α , commonly chosen as $\alpha \in \{\frac{1}{2}, \frac{3}{2}, 2, 3\}$ [28]. The new vertex v_r with the smallest value of the objective function is then accepted if its value is less than the value of the function at the vertex with the *second-highest* value of the objective function [28]. (The second-worst vertex is chosen as the point of comparison since it will then be the worst vertex in the next step [28].)

This algorithm tends to perform better than the compass search method since it evaluates the objective function at fewer points on each iteration; however, McKinnon [35] showed that there exists a family of degenerate functions that cause the simplex to collapse along the direction of steepest descent, preventing further progress. McKinnon refers to this phenomenon as “repeated focused inside contrac-

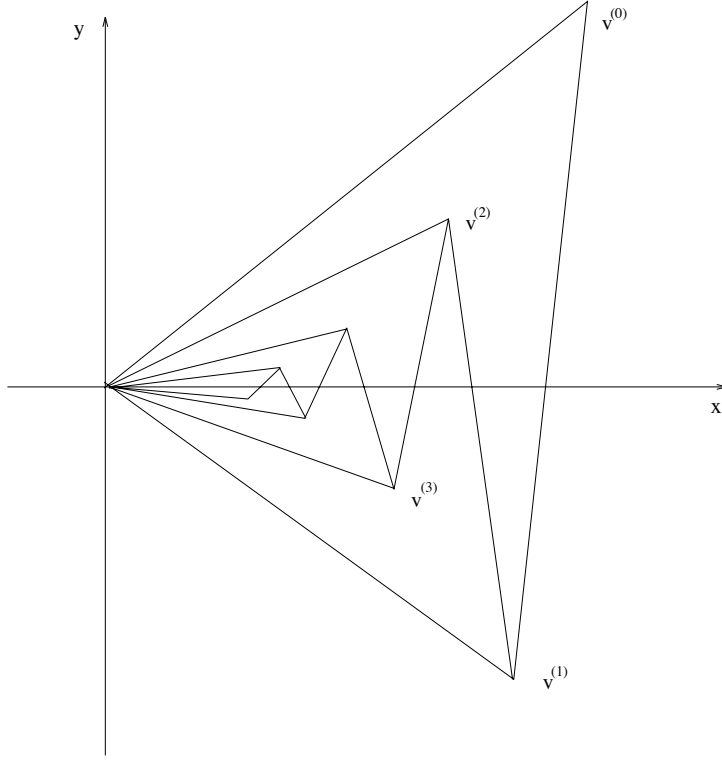


Figure 3.14: Steps taken by a vertex during simplex collapse, a failure mode of the Nelder-Mead algorithm. (Reproduced from [35, Fig. 2.1].)

tion,” or RFIC. This is illustrated in Fig. 3.14. Although our objective function does not necessarily cause this behavior, it serves to illustrate one way in which this method can fail.

3.6.4 Simulated annealing

Unlike the deterministic methods described previously in this section, simulated annealing is a stochastic optimization process. It was independently described [5] by Kirkpatrick et al. [26] in 1983 and Černý [10] in 1985. This algorithm was created by comparison with the physical process of annealing in statistical mechanics. The basic procedure consists of creating a Markov chain of candidate solutions by drawing from a random distribution and accepting the new states with a probability that depends on a “temperature” parameter, which is slowly cooled. A basic description of the algorithm, adapted from Bertsimas and Tsitsiklis [5], is given in Algorithm 4.

One thing that is immediately apparent about this algorithm is its similarity to the simple Monte Carlo algorithm described in Section 3.5.1. In each case, we look for a new point on each iteration that

Algorithm 4 Basic simulated annealing

Given a function $f : \mathbb{R}^n \rightarrow \mathbb{R}$, an initial state $x_0 \in \mathbb{R}^n$, and a decreasing set of temperatures T_i

function ANNEAL(f, x_0, T_i)

for $i=1, 2, \dots, N$ **do**

$x' \leftarrow x_{i-1} + \text{a random step in some direction}$

if $f(x') \leq f(x_{i-1})$ **then**

Accept x' as the new value x_i

else

Accept x' as the new value x_i with probability $e^{-(x'-x)/T_i}$.

Otherwise, $x_i \leftarrow x_{i-1}$.

end if

end for

return x_N

end function

satisfies a criterion that we slowly make more stringent. The only concrete differences are that in simulated annealing, the next point is chosen by taking a random step from the current point, and sometimes we accept a new point with a higher value of the function being minimized.

Computationally, this algorithm can be more efficient than the naïve Monte Carlo method since it will ideally test fewer points on each iteration. However, if the temperature parameter is too small, the algorithm might not be able to quickly find a better point than the current one, leading it to test a large number of points on each iteration. This can quickly make simulated annealing *slower* than the naïve Monte Carlo algorithm.

Ultimately, simulated annealing provided no clear benefit over the naïve algorithm for data from the AT-TPC. It did not converge reliably, and the resolution was poorer. Finally, although simulated annealing is a more efficient algorithm in principle, the predictable run time of the simple Monte Carlo method is attractive when scheduling the analysis on a high-performance computer.

3.6.5 Neural networks

Modeled after networks of neurons in the brain, an artificial neural network consists of a set of interconnected nodes where each connection is assigned a weight [8]. The weights are chosen such that when a set of inputs is applied on one side of the network, the correct outputs are produced on the other side. The network is “trained” with a large data set with known inputs and outputs by presenting the inputs one by one and adjusting the weights on each iteration. The goal is to generalize the network’s “understanding” of the problem so that it can successfully find the correct outputs for an unfamiliar set of inputs.

Neural networks were considered as a potential first step to the fitting process for AT-TPC data. However, the technique using the Hough transform and linear fits described in Section 3.4.4 does a much better job and is much simpler.

3.6.6 Kalman filter

The Kalman filter is a recursive optimization algorithm that is commonly used in diverse fields such as automated navigation, robotics, and aviation [30, 56]. It also finds applications in high-energy physics [14], making it a good candidate for fitting tracks in the AT-TPC.

A Kalman filter models a system using a state vector and a physical model. The state vector represents the state of the system at a given moment, and might include components like the position of a particle and its momentum. The physical model must be able to take the state vector and produce an estimate of the new state vector at the next moment in time. For the AT-TPC, a suitable model might include the Lorentz force and a contribution to account for the stopping power of the gas.

Rather than considering the data set as a whole, the Kalman filter fits each point individually, iterating through the data set only once. On each step, the model is used to predict the new state vector based on the state from the previous step. The measured data point is then averaged with this prediction to correct it. This averaging allows the Kalman filter to smooth out noisy data [30].

One drawback of most implementations of the Kalman filter is that they require data points that are evenly spaced in time. This is very often not the case in the AT-TPC, however, since there are frequently large gaps in the tracks recorded by the detector. This limitation ultimately prevented us from using the Kalman filter to obtain precise results.

3.7 Vertex energy reconstruction

Using the fit results, we have enough information to reconstruct the energy of the beam projectile at the reaction vertex in two different ways. This redundancy is a benefit since it provides a way to check whether the analysis is correct, and it also provides a measure of the resolution of the detector. Furthermore, any systematic deviation between the two reconstructions can be used to separate elastic and inelastic scattering events since the position of the vertex along the z axis does not depend on the kinematics.

3.7.1 Using the vertex position

The Monte Carlo result gives the location of the vertex within the detector. The energy of the beam particle at the vertex can be calculated by finding the amount of energy lost by the beam particle to the gas as it moved from the beam entrance window to the vertex.

Assuming the beam particle entered the chamber with energy E_i , the stopping power calculation from SRIM [57] gives the particle's range as a function of energy, $R(E)$. Thus, the initial range of the full-energy beam particle is

$$R_i = R(E_i). \quad (3.37)$$

The beam particle loses energy as it travels from the window to the vertex. Since R is a function of energy, we could also think of this as the particle losing range. Then, the amount of range “remaining” at the vertex is

$$R_f = R_i - (1.0 \text{ m} - z_0). \quad (3.38)$$

Finally, the inverse of the range function, R^{-1} , can be used to find the energy of a particle with range R_f :

$$E_f = R^{-1}(R_f). \quad (3.39)$$

This final energy E_f is the energy of the beam particle at the reaction vertex.

3.7.2 Using kinematics

After fitting the tracks, the initial energy and scattering angle of the recoil particle are known. Assuming that this particle was at rest before it interacted with the projectile, we have enough information to reconstruct the vertex energy using kinematics.

In the laboratory frame, the target nucleus has four-momentum $P_t^{\text{lab}} = (m_t, 0, 0, 0)$. In the center-of-mass frame, its four-momentum is $P_t^{\text{CM}} = (E_t, -p_{\text{CM}}, 0, 0)$. These four-vectors can be used to find the components of the Lorentz boost matrix from the center-of-mass frame to the lab frame. The results are

$$\cosh \chi = \frac{\sqrt{p_{\text{CM}}^2 + m_t^2}}{m_t} \quad (3.40)$$

$$\sinh \chi = \frac{p_{\text{CM}}}{m_t}, \quad (3.41)$$

where $\chi \equiv \tanh^{-1}(\nu/c)$ is the rapidity. The Lorentz transform can then be applied to the recoil particle to find p_{CM} . The lab energy of the recoil particle is

$$E_r^{\text{lab}} = E_r^{\text{CM}} \cosh \chi - p_{\text{CM}} \cos \theta_{\text{CM}} \sinh \chi. \quad (3.42)$$

If we plug in Eqs. (3.40) and (3.41), assume elastic scattering, and solve for p_{CM}^2 , we find

$$p_{\text{CM}}^2 = \frac{m_t E_r^{\text{lab}} - m_t^2}{1 - \cos \theta_{\text{CM}}}. \quad (3.43)$$

Finally, the kinetic energy of the beam particle T_b can be found using the relativistic invariant

$$s = \left(\sum_i P_i \right)^2 \quad (3.44)$$

for four-momenta P_i . We can find this invariant for the two frames, set them equal to each other, and solve for T_b to find

$$T_b = \frac{1}{2m_t} \left[\left(\sqrt{m_b^2 + p_{\text{CM}}^2} + \sqrt{m_t^2 + p_{\text{CM}}^2} \right)^2 - (m_t + m_b)^2 \right], \quad (3.45)$$

where m_t is the mass of the target and m_b is the mass of the beam.

CHAPTER 4

SIMULATIONS

In order to understand the behavior of the AT-TPC and establish expectations for experimental results, we simulated several sets of data under the same conditions as the experiment. The purpose of this was to model the resolution of the detector as well as the efficiency of the trigger and analysis methods. By modifying the number of simulated events, we can also determine how many events are needed in an experiment to be able to resolve resonances and measure their strengths.

The simulations discussed in this chapter were performed using software that is based on the same libraries as those used for analyzing AT-TPC data. Specifically, the simulated particle tracks were generated using the same functions that are used to generate candidate tracks in the Monte Carlo algorithm, so the simulated tracks use the same energy loss data, Lorentz force calculations, calibrations, and pad plane projection functions as the analysis process. Therefore any differences between the simulations and the data should only be due to features of the data or effects neglected in the model, and not due to discrepancies between the simulation and analysis codes.

This chapter begins with an overview of the simulation process. Following that are the results of several simulations that were performed.

4.1 Overview of the simulation process

Although several simulations with slightly different parameters and settings were performed, the simulation process was largely the same for each of them. This process is described in general terms in this section; any deviations from this procedure for specific simulations are outlined in later sections.

4.1.1 Parameter generation

The first step of the simulation is to create a set of simulated track parameters. This can be done in a number of different ways depending on the goals of a particular simulation.

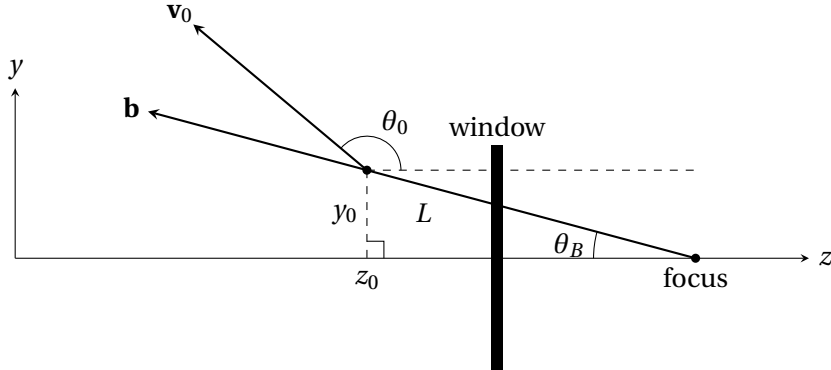


Figure 4.1: Illustration of coordinate calculation for uniform distributions. The meanings of the variables are given in Section 4.1.1.1. Note that this is a projection into the zy plane, and the true three-dimensional orientation also depends on azimuthal angles ϕ_0 and ϕ_B and vertex location x_0 .

4.1.1.1 Uniform distribution

The first set of simulations was performed using parameters drawn from flat distributions. This is useful for modeling the efficiency of the detector since it uniformly populates the parameter space of the tracks, making it easy to see what angles and energies are cut by the trigger or by the analysis. Flat distributions were generated as follows:

1. Pick z_0 from a uniform distribution between 0 mm and 1000 mm, which are the locations of the sensor plane and the beam entrance window, respectively.
2. Generate a random beam vector \mathbf{b} by selecting the beam azimuthal angle ϕ_B and beam polar angle θ_B such that the result will be uniformly distributed over a portion of the unit sphere. The azimuthal angle was allowed to vary uniformly over $[0, 2\pi)$, and the polar angle varied between 0° and 2° , where 0° is parallel to the beam axis. This beam vector helps simulate the effect of the emittance of the beam.
3. Use the beam vector to calculate the values of x_0 and y_0 at the vertex location z_0 . Assume that the beam tracks originate at a focus 14 cm upstream of the beam entrance window. The location of this focus was chosen such that a particle leaving it at the maximum beam polar angle of 2° would make it through the beam entrance window, which had a diameter of 10 mm.
4. Generate the azimuthal and polar angles describing the outgoing proton's initial velocity vector \mathbf{v}_0 with respect to the beam track. Select the azimuthal angle from a uniform distribution over $[0, 2\pi]$

and the polar angle from a uniform distribution over $[\pi/2, \pi]$. The polar angle is greater than $\pi/2$ since the beam is moving in the $-\hat{z}$ direction.

5. Transform the two angles from the previous step to find angles with respect to the coordinate axes rather than the beam track. This transformation corresponds to a rigid-body rotation, and it is done with Euler angles. This yields the proton track's initial azimuthal angle ϕ_0 and polar angle θ_0 .
6. Find the length L of the beam track between the entrance window and the reaction vertex. Use this to calculate the ^{46}Ar vertex energy with the procedure from Section 3.7.1. Calculate the proton energy E_0 using the kinematics formulas below. If the proton energy is less than 0.5 MeV, discard the event as it will almost certainly be fit poorly.

The relationships between the different quantities described above are illustrated in Fig. 4.1.

The initial energy of the proton is calculated from the ^{46}Ar vertex energy using kinematics formulas. To derive these equations, first consider a generic scattering process $B(A, D)C$ where beam particle A has kinetic energy T and target B is at rest. Let C be the target-like recoil particle and D be the beam-like projectile. Since we are interested in finding the proton energy, we will need to calculate the energy of particle C . In the center-of-mass frame, this is

$$E_C^{\text{CM}} = \sqrt{(p'_{\text{CM}})^2 + m_C^2}, \quad (4.1)$$

where p'_{CM} is the outgoing momentum in the center-of-mass frame. This momentum is

$$p'_{\text{CM}} = \sqrt{\frac{(s - m_C^2 - m_D^2)^2 - 4m_C^2 m_D^2}{4s}} \quad (4.2)$$

where s is the square of the total incoming four-momentum

$$s = (P_A + P_B)^2 = (m_A + m_B)^2 + 2m_B T, \quad (4.3)$$

which is a relativistic invariant.

Similarly, in the lab frame, the energy of particle C is

$$E_C = \sqrt{p_C^2 + m_C^2}. \quad (4.4)$$

The lab momentum p_C can be found by equating the components of the lab and center-of-mass momenta that are transverse to the Lorentz boost between the two frames:

$$p_C = \frac{p'_{\text{CM}} \sin \theta_{\text{CM}}}{\sin \theta_C}. \quad (4.5)$$

Since the lab scattering angle θ_C is known, this leaves the center-of-mass angle θ_{CM} to be determined. This can also be found by equating components of the two momenta, yielding

$$\sin \theta_{CM} = \frac{\sin \theta_C (E_C^{CM} \cos \theta_C \sinh \chi + \alpha)}{p'_{CM} (\cosh^2 \chi - \cos^2 \theta_C \sinh^2 \chi)} \quad (4.6)$$

where

$$\alpha \equiv \sqrt{\cosh^2 \chi \left((E_C^{CM})^2 + m_C^2 (-\cosh^2 \chi + \cos^2 \theta_C \sinh^2 \chi) \right)}.$$

In these equations, χ is the rapidity of the boost from the center-of-mass frame to the lab, which is given by

$$\chi = \log \left(\frac{p_{CM} + \sqrt{m_B^2 + p_{CM}^2}}{m_B} \right). \quad (4.7)$$

The initial center-of-mass frame momentum p_{CM} can be found by using Eq. (4.2) and replacing m_C and m_D with m_A and m_B , respectively. These equations are evaluated with the appropriate mass values to find the initial energy of the proton in the lab frame from the randomly generated scattering angle and ^{46}Ar vertex energy.

4.1.1.2 Simulated scattering distribution

Although the uniform distributions described above are useful for modeling the efficiency of the detector, they are not representative of the distributions of parameters encountered in a real experiment. A more realistic set of simulated tracks can be created by drawing parameters from a distribution created by a simulation of the scattering process to be measured.

For the simulation of the $^{46}\text{Ar}(p, p')$ experiment, the parameter generation was based on a calculation from the R matrix code DSIGMAIV¹ using the expected resonance properties shown in Table 4.1. The cross section of the reaction was calculated using this code for center-of-mass incoming proton energies from 2.0 MeV to 4.5 MeV and center-of-mass scattering angles from 40° to 140°. The elastic scattering component was simulated using the global optical potential from Koning and Delaroche [29]. The optical potential parameters used are shown in Table 4.2 and the results of the calculation are shown in Fig. 4.2.

The results from DSIGMAIV give the differential cross section as a function of proton energy and scattering angle in the center of mass frame. The cross section is effectively an unnormalized probability of

¹Originally written by Wang Hongwei of the Shanghai Institute of Applied Physics at the Chinese Academy of Sciences. The version used included modifications made by Wolfgang Mittig of the NSCL.

^{47}Ar state	E_R	L	$2J$	Π	S	Γ_p
g.s.	2.582	1	3	-1	0.6	10.94
1.130	3.712	1	1	-1	0.8	63.80

Table 4.1: Expected resonance properties calculated from the results of Gaudefroy et al. [18] using the procedure from Section 1.1.8. The resonance energy E_R is given in MeV, and the resonance width Γ_p , as calculated by DSIGMAIV, is given in keV. L is the orbital angular momentum, J is the total angular momentum, Π is the parity, and S is the spectroscopic factor.

Term	V_r	R_r	a_r	V_i	r_i	a_i
Volume	62.60	1.19	0.67	0.30	1.19	0.67
Surface	-	-	-	7.70	1.29	0.54
Spin-Orbit	5.80	1.00	0.59	-	-	-

Table 4.2: Global optical model [29] parameters used in the simulation. V_r , R_r , and a_r are the depth, radius, and diffuseness parameters for a real-valued Woods-Saxon potential, while V_i , R_i , and a_i are the corresponding parameters for an imaginary Woods-Saxon potential. The depth is given in MeV, and the radius and diffuseness are given in fm. The Coulomb radius used was 1.27 fm.

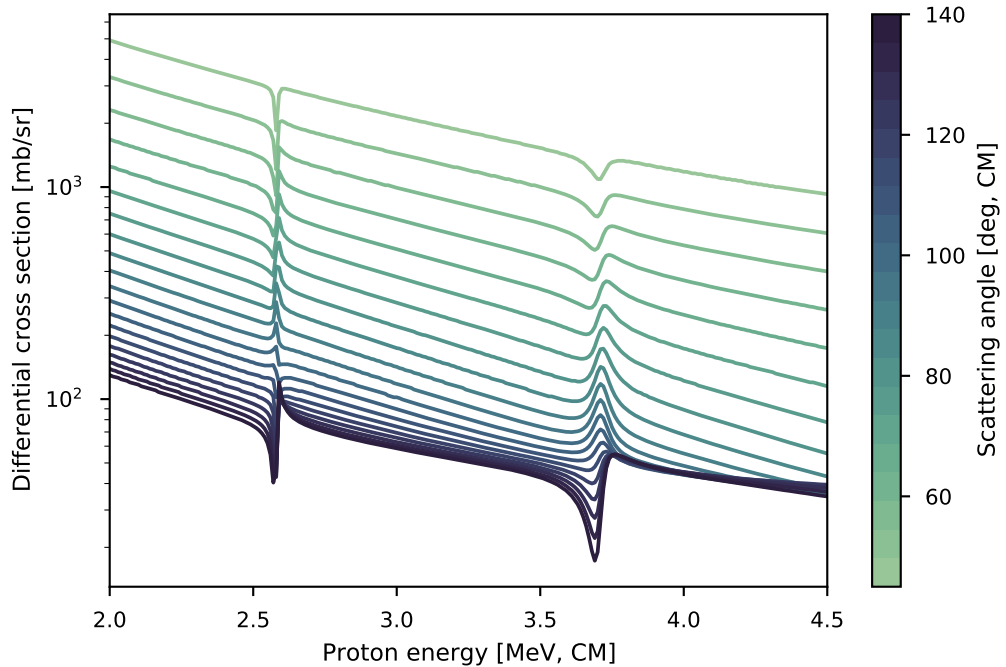


Figure 4.2: Results of DSIGMAIV calculation in the region of interest.

observing a particle with the given energy and scattering angle, so these results can be used with rejection sampling to generate a set of proton energies and scattering angles that follow our expectations for the experimental results.

Given the incoming proton energy E_p^{CM} and center-of-mass scattering angle θ_{CM} , we can calculate the energy of the outgoing proton using relativistic kinematics. The Lorentz boost matrix from the center-of-mass frame to the lab frame is given by

$$\Lambda = \begin{pmatrix} \cosh \chi & \sinh \chi & 0 & 0 \\ \sinh \chi & \cosh \chi & 0 & 0 \\ 0 & 0 & 1 & 0 \\ 0 & 0 & 0 & 1 \end{pmatrix} \quad (4.8)$$

for rapidity χ . The values of $\sinh \chi$ and $\cosh \chi$ can be found by boosting the target proton from the center-of-mass frame to the lab frame, where it is stationary. The result of that is

$$\cosh \chi = \frac{\sqrt{p_{\text{CM}}^2 + m_p^2}}{m_p} \quad (4.9)$$

$$\sinh \chi = \frac{p_{\text{CM}}}{m_p}, \quad (4.10)$$

where m_p is the proton mass and p_{CM} is the momentum in the center-of-mass frame. The latter quantity is known since we know E_p^{CM} :

$$p_{\text{CM}} = \sqrt{(E_p^{\text{CM}})^2 - m_p^2}. \quad (4.11)$$

Finally, we can boost the outgoing proton's four-momentum from the center-of-mass frame to the lab frame to find $E_{p'}^{\text{lab}}$:

$$\begin{aligned} E_{p'}^{\text{lab}} &= E_{p'}^{\text{CM}} \cosh \chi - p_{\text{CM}} \cos \theta_{\text{CM}} \sinh \chi \\ &= \sqrt{p_{\text{CM}}^2 + m_p^2} \frac{\sqrt{p_{\text{CM}}^2 + m_p^2}}{m_p} - p_{\text{CM}} \cos \theta_{\text{CM}} \frac{p_{\text{CM}}}{m_p} \\ &= \frac{p_{\text{CM}}^2}{m_p} (1 - \cos \theta_{\text{CM}}) + m_p. \end{aligned} \quad (4.12)$$

After subtracting away the rest mass, this value can be used as the initial energy E_0 in the parameter set.

The scattering angle in the lab frame is given by

$$\theta_{p'}^{\text{lab}} \approx \frac{1}{2} (\pi - \theta_{p'}^{\text{CM}}). \quad (4.13)$$

This is a non-relativistic approximation, but it holds quite well at the low energies of this experiment. This value is used to find the parameter θ_0 , which is given by

$$\theta_0 = \pi - \theta_{p'}^{\text{lab}} \quad (4.14)$$

since the coordinate system is defined such that the beam moves in the $-\hat{z}$ direction. The azimuthal angle ϕ_0 is a free parameter in the scattering process, so it is chosen randomly from a uniform distribution over the domain $[0, 2\pi]$.

Next, we need to calculate the initial position of the particle. The transverse positions x_0 and y_0 are chosen randomly from normal distributions centered at 0 with standard deviation 10 mm, a choice which simulates the emittance of the beam. The z_0 position is found using the kinematics of the beam particle and the stopping power of the gas.

The energy of the ^{46}Ar beam particle in the center-of-mass frame is simply

$$E_{\text{Ar}}^{\text{CM}} = \sqrt{p_{\text{CM}}^2 + m_{\text{Ar}}^2} \quad (4.15)$$

for the same p_{CM} as in Eq. (4.11) above. The lab energy is then

$$E_{\text{Ar}}^{\text{lab}} = E_{\text{Ar}}^{\text{CM}} \cosh \chi + p_{\text{CM}} \sinh \chi. \quad (4.16)$$

Expressions for p_{CM} , $\cosh \chi$ and $\sinh \chi$ from above can then be substituted into this equation to find the value.

Once the vertex energy of the ^{46}Ar nucleus is known, the vertex position z_0 can be found from the calculated range of the particle in the detector fill gas, a quantity that can be calculated with SRIM [57]. If the range of the incoming ^{46}Ar nucleus at the full beam energy is R_i and the range of an ^{46}Ar nucleus with the final vertex energy is R_f , then the distance traveled by the particle must be $R_i - R_f$, so the vertex is located at

$$z_0 = (1.0 \text{ m}) - (R_i - R_f). \quad (4.17)$$

At this point, we have a complete set of parameters $(x_0, y_0, z_0, E_0, \phi_0, \theta_0)$ that describes the simulated proton tracks.

4.1.2 Tracking and event generation

Once the set of initial parameters has been found, the proton tracks can be simulated. The simulation method is the same as in Section 3.4, but instead of finding the peak in each channel, each entire signal

is kept. These signals represent the ideal response of the detector. To better simulate the behavior of the detector, three kinds of noise are added to the simulated signals.

First, random Gaussian noise is added to each signal to simulate noise in the electronics. The distribution used to generate this noise has a mean of 0 and a standard deviation of 6, where both values are measured in ADC bins. This standard deviation was found by analyzing the distribution of the noise amplitudes of a number of experimental signals inside a time window where the traces contained no pulses.

The second kind of noise added is a simulated baseline depression signal of the form discussed in Section 3.1. The track of an ^{46}Ar nucleus with the full beam energy is simulated in the detector, and the signals are accumulated bin-wise to find the total energy deposited as a function of drift time. This signal is then inverted, rescaled, and added to each simulated signal to approximate the baseline depression effect in the experiment. The rescaling amplitude was found empirically from recorded experimental signals.

Finally, a constant offset, or *pedestal*, is added to each channel. The pedestals are slightly different for each channel as they originate from the baseline of each channel's ADC. These pedestals were measured during the experiment by triggering the detector with a pulser. After adding the pedestals, the signals are clipped to ensure they remain between 0 and 4096, the range of the 12-bit ADC.

4.1.3 Simulating the trigger

One of the most complex parts of the simulation process is determining whether an event would trigger the GET electronics. Each channel in the AGET chip has a subsystem that compares the shaped, amplified input signal to a configurable threshold to determine if the channel was hit (Fig. 4.3). These channel-level triggers are then accumulated at the CoBo level to make a decision about whether an event should be recorded. This process must be simulated in order to estimate the trigger efficiency during the experiment.

All of the information about the GET electronics presented in this section was taken from Baron and Delagnes [3].

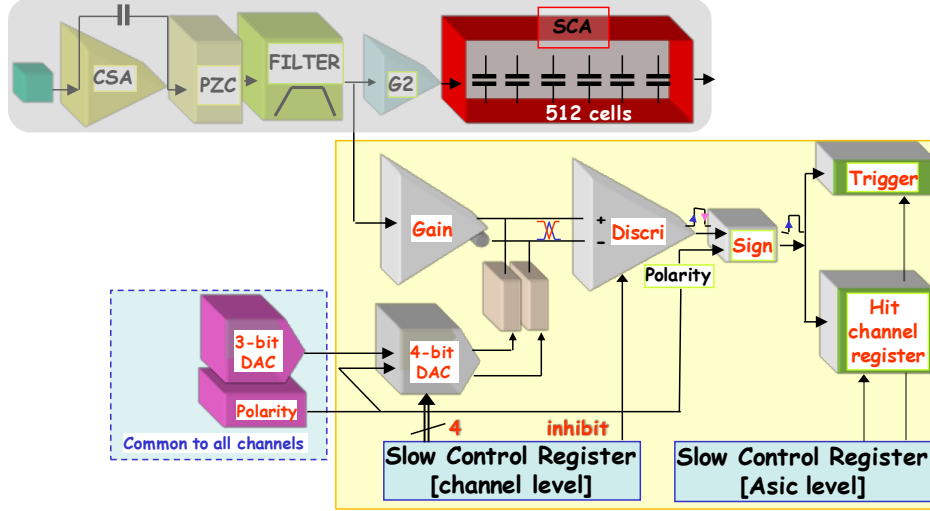


Figure 4.3: Schematic of a channel in the GET electronics, showing the trigger threshold circuit. (Reproduced from [3].)

4.1.3.1 Generating channel-level trigger signals

The trigger threshold for each channel can be represented as a 7 bit integer. The three most-significant bits are common to all channels in a given AGET, and the four least-significant bits are unique to each channel. An additional bit is used to store the polarity.

This raw, integer threshold value must be converted to be on the same scale as the data. The trigger discriminator in the electronics covers 17.5 % of the input range of the ADC; therefore, since the ADC has 4096 bins, the threshold in ADC bins must be

$$\text{Thresh.} = \frac{\text{Raw thresh.}}{128} \times 0.175 \times 4096, \quad (4.18)$$

where the raw threshold is the value determined from the two settings described above. The raw threshold is divided by 128 because that is the maximum value of a 7 bit unsigned integer.

Any time the amplified, shaped input signal rises above the threshold value, a trigger signal is generated by the AGET for the corresponding channel. The trigger signal is a square wave with a height of 48 ADC bins and a width of approximately² 235 ns. The trigger signal is either on or off: no trigger pileup can occur at the channel level. If the signal is still above threshold at the end of the trigger pulse, another trigger pulse will fire. This repeats until the signal falls below threshold.

²This value is not well-defined, but is instead within a small tolerance due to the way the chip is designed [3].

4.1.3.2 Generating CoBo-level multiplicity signals

Before discussing the multiplicity signals generated by the CoBo, a brief detour is required to understand the clocks used by the CoBo. The CoBo has a master clock frequency of 100 MHz from which several other clock domains are derived. The two domains relevant to the analysis are the *write* clock and the *read* clock:

- The write clock controls the sampling frequency in the detector, and its frequency is a configurable fraction of the master clock. In the ^{46}Ar experiment, the write clock frequency was 12.5 MHz. When the description of the analysis refers to a generic “clock frequency,” this is the frequency meant.
- The read clock controls the readout of the sampled values from the SCA into the ADC, and consequently the readout of digitized samples from the ADC to the CoBo. It has a fixed frequency of 25 MHz.

Between triggered events, each AGET sums the trigger signals from its 64 physics channels and continuously outputs this trigger multiplicity signal to the ADC. The CoBo sums the digitized multiplicity signals from all of the AGETs it controls, and it integrates this signal over a sliding time window. The multiplicity window has a configurable width which is defined in units of read clock ticks (or, units of 40 ns). This width was set to 300 ticks, or 12 μs , during the ^{46}Ar experiment. The integrated signal is then compared to a threshold value, which was set to 20 000 during most of the experiment. If the integrated multiplicity signal rises above this threshold, then the CoBo generates a trigger request.

An important caveat when simulating this process is that the CoBo samples the trigger signals from each AGET using the read clock frequency, or every 40 ns. For convenience, the simulated trigger signals were sampled at the same 12.5 MHz frequency as the simulated events. Therefore, the simulated integrated multiplicities must be multiplied a correction factor of

$$\frac{\nu_r}{\nu_w} = \frac{25\text{MHz}}{12.5\text{MHz}} = 2 \quad (4.19)$$

since the CoBo would sample the signal twice as many times as the simulation during the multiplicity window.

4.1.3.3 Generating global triggers

In the full GET electronics system, the channel-level trigger signals are collected by the MuTAnT module and combined using a configurable algorithm to generate a global trigger for the detector. However, the MuTAnT module was not yet available at the time of the $^{46}\text{Ar}(\text{p},\text{p}')$ measurement, so the AT-TPC was triggered with an external system instead.

To simulate this external trigger, the CoBo-level trigger signals are each compared to their individual integrated multiplicity thresholds. This produces a set of 10 Boolean values which are then combined with a logical OR to generate the global trigger. Therefore, a global trigger is generated if any individual CoBo rises above its multiplicity threshold during an event.

4.1.4 Cleaning and minimization

After testing whether the simulated events triggered the electronics, the events are processed by the cleaning and fitting functions described above in Sections 3.3 and 3.5. The results of the fits are stored along with the values of the parameters that were used to simulate the track.

4.1.5 Post-processing and cuts

After generating and fitting the tracks, the first step of the analysis process is to apply a cut on the values of the objective function χ^2 . Cuts are applied independently on the two components χ_{pos}^2 and χ_{en}^2 (see Section 3.4.3 for definitions). The χ^2 cuts also exclude events that cause the Monte Carlo fitter to return an error. This happens, for example, if there are too few data points in the event.

A second, independent cut is applied on the results of the trigger step of the simulation. This is possible because, unlike for experimental data, the simulation code can still perform the Monte Carlo fit on an event even if the event fails to fire the simulated trigger. This enables us to independently assess the acceptances of the detector and the fitting software.

These two cuts divide the data set into six categories based on whether or not the detector was triggered and whether the fit was good, the fit was bad, or the fit failed with an error.

Set	Runs	Pads excluded	Mult. thresh.	Pad threshold		Notes
				MSB	LSB	
0	53–76	436	15000	1	6	
1	77	436	15000	1	2	
2	78–102	4247	20000	1	2	
3	103–186	436	20000	1	2	
4	188–217	665	20000	1	2	
5	218–end	665	20000	1	2	CoBos 4 & 9 excluded

Table 4.3: Trigger conditions used in the experiment. As noted in the text, the unusually large number of excluded pads in set 2 was due to a user error.

4.2 Simulated acceptance

Using the methods described above, a set of simulations was performed to estimate the acceptance of the AT-TPC’s trigger setup and the efficiency of the fitting process. Because the trigger conditions were adjusted several times during the experiment, a separate simulation was performed for each set of trigger conditions so that the results could later be used to correct the recorded data for the efficiency. The trigger conditions are listed in Table 4.3. The conditions for run set 1 were skipped since that set only includes one run. For each of the remaining sets of runs, 10^6 events were simulated using a uniform parameter distribution as described in Section 4.1.1.1.

One of the most significant differences between the run sets was the size and shape of the trigger exclusion and low-gain regions on the pad plane. These regions are shown in Fig. 4.4. The trigger exclusion regions were defined by accumulating a large number of beam-only events and selecting the pads that recorded the largest signals. The large size of the region for set 2 was due to a user error, and the wedge shape of the region for set 5 was due to the exclusion of all of CoBos 4 and 9 from the trigger in an effort to reduce the trigger rate.

The distributions of the accepted and rejected events are shown as functions of the track parameters in Figs. 4.7 to 4.11. The trigger conditions appear to reject most events with a proton energy greater than approximately 4 MeV or a center-of-mass scattering angle greater than approximately 80° . Interestingly, the acceptance is not isotropic with respect to the azimuthal angle, but instead shows some fluctuations. This happens because the azimuthal symmetry of the detector is broken when the detector is tilted and placed inside the magnetic field.

In contrast with the χ^2 distributions shown in Figs. 4.5 and 4.6, the acceptances shown in Figs. 4.7

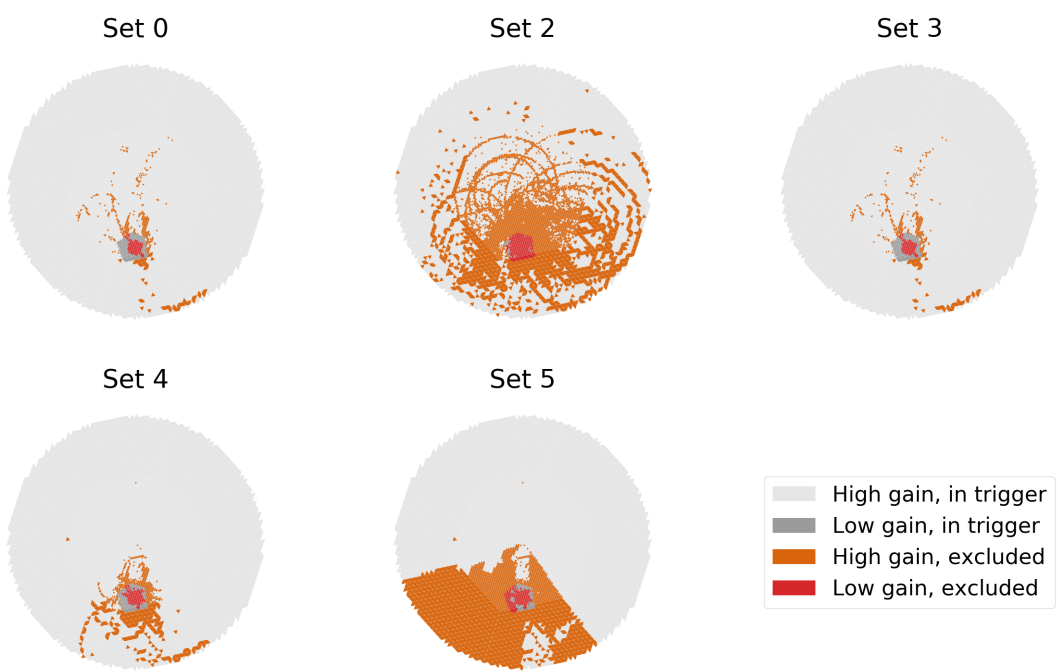
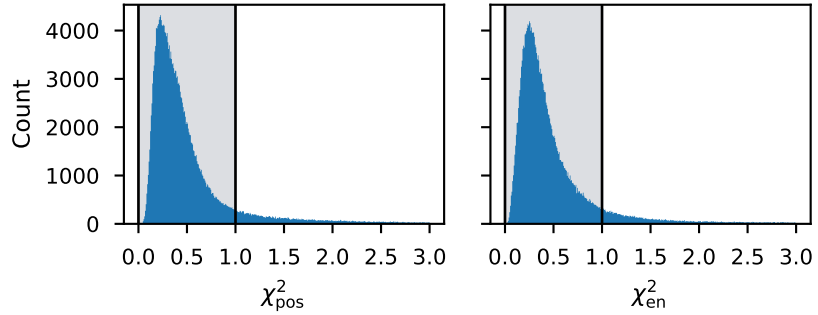
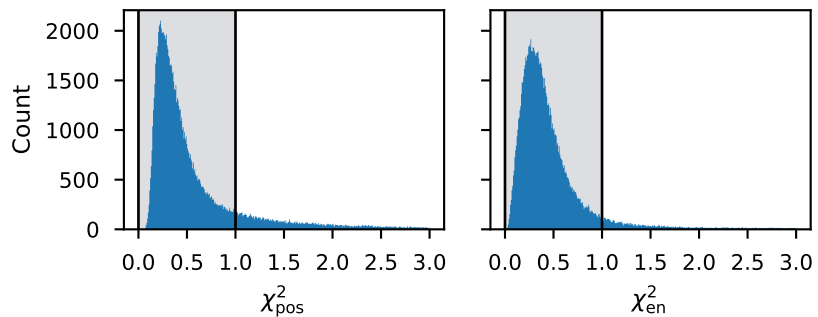


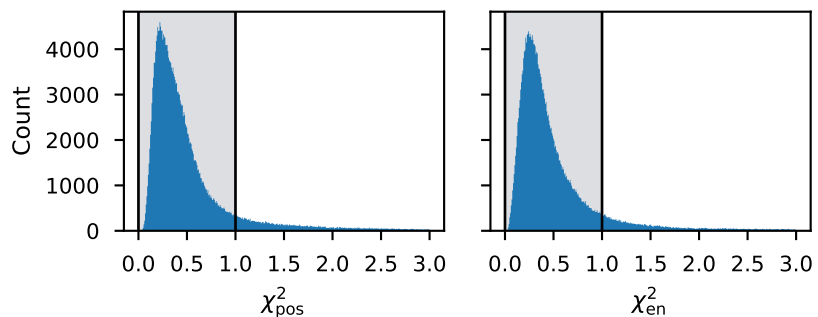
Figure 4.4: Trigger exclusion and low-gain regions used in the simulation and in the experiment. Only pads in the light and dark gray regions contribute to the trigger.



(a) Set 0

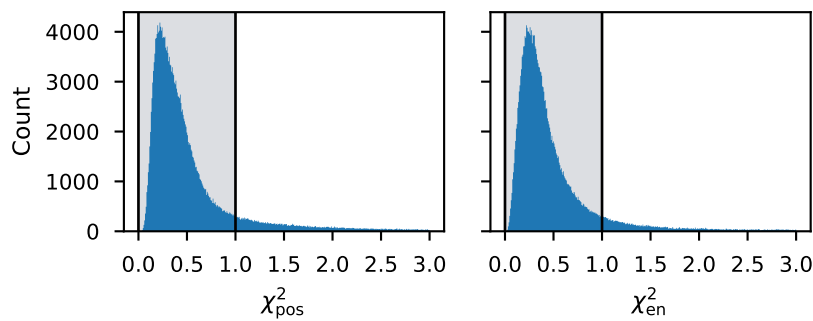


(b) Set 2

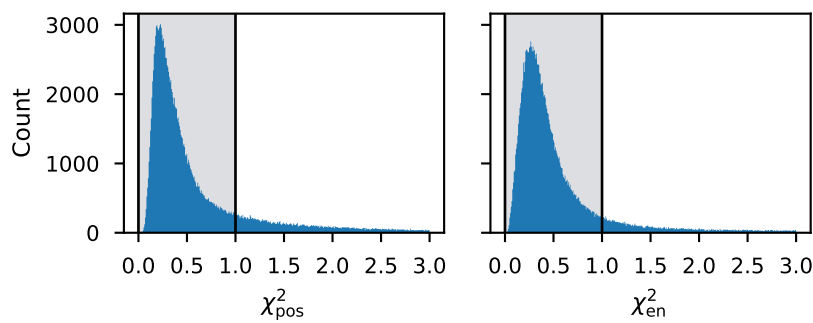


(c) Set 3

Figure 4.5: Distributions of the χ^2 values for the simulated events in the first three sets of runs. Events that fell outside of the shaded region between the two vertical black lines on the histogram were thrown away. The events that were kept had $\chi^2_{\text{pos}} < 1.0$ and $\chi^2_{\text{en}} < 1.0$. This plot does not include events for which the fitter returned an error.



(a) Set 4



(b) Set 5

Figure 4.6: Distributions of χ^2 values for the final two sets of runs. See the caption of Fig. 4.5 for details.

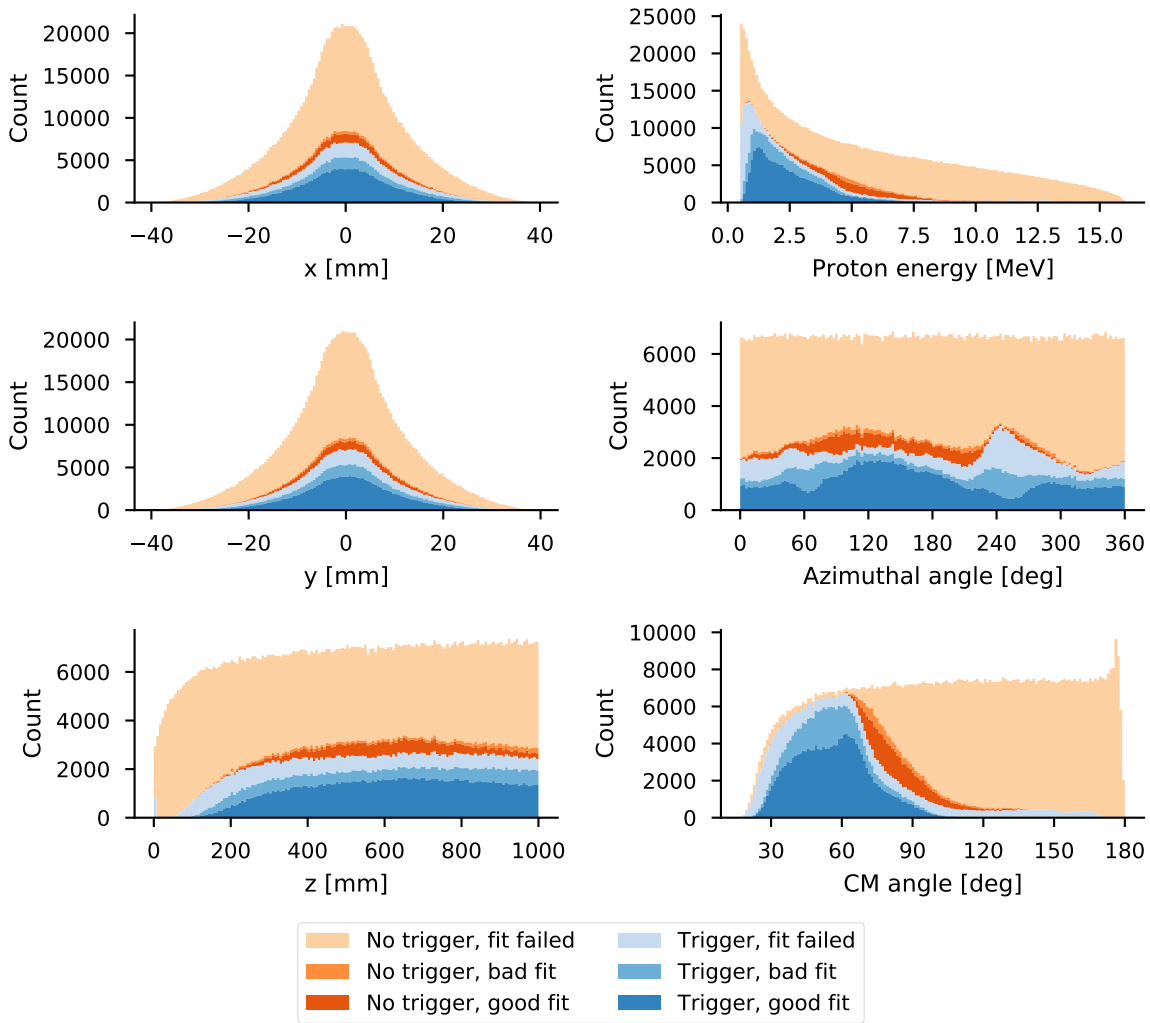


Figure 4.7: Simulated acceptance of the trigger and analysis as a function of the track parameters for trigger parameter set 0. The trigger and analysis cuts were applied independently to the simulated events, leading to six classes of events. Events are grouped into “trigger” and “no trigger” groups depending on whether they would have triggered the electronics in a real experiment. These groups are then subdivided into “good fit” and “bad fit” groups depending on whether they pass the χ^2 cuts. Events in the “fit failed” groups caused an error in the Monte Carlo algorithm. Only events in the “trigger, good fit” group would have been recorded and correctly reconstructed in the experiment. The six groups are stacked in these histograms, so the contour of the top of each plot reflects the shape of the total distribution.

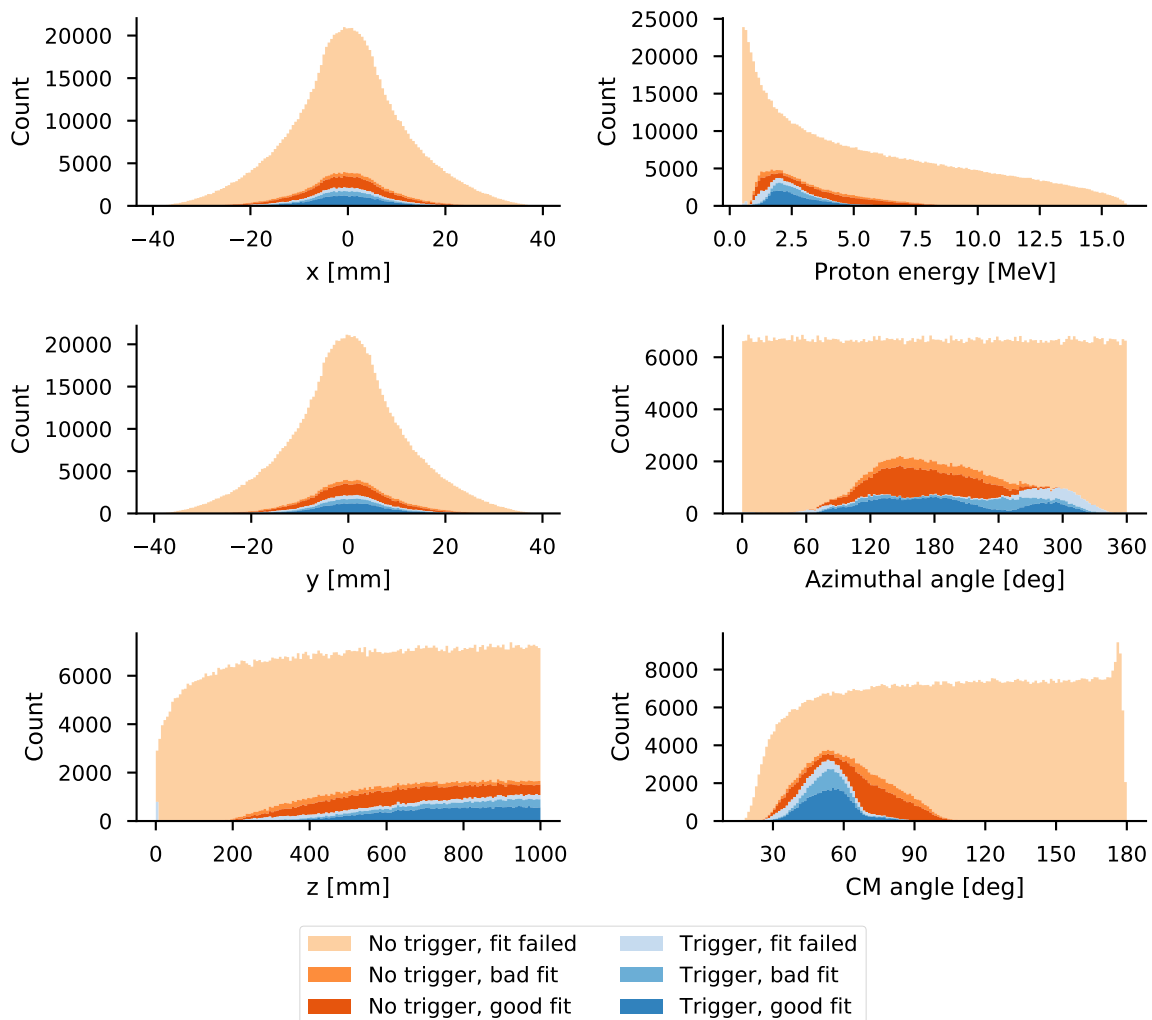


Figure 4.8: Simulated acceptance of the trigger and analysis for trigger parameter set 2. The large trigger exclusion region used in these runs prevented events outside of a very small angular and energy domain from being accepted.

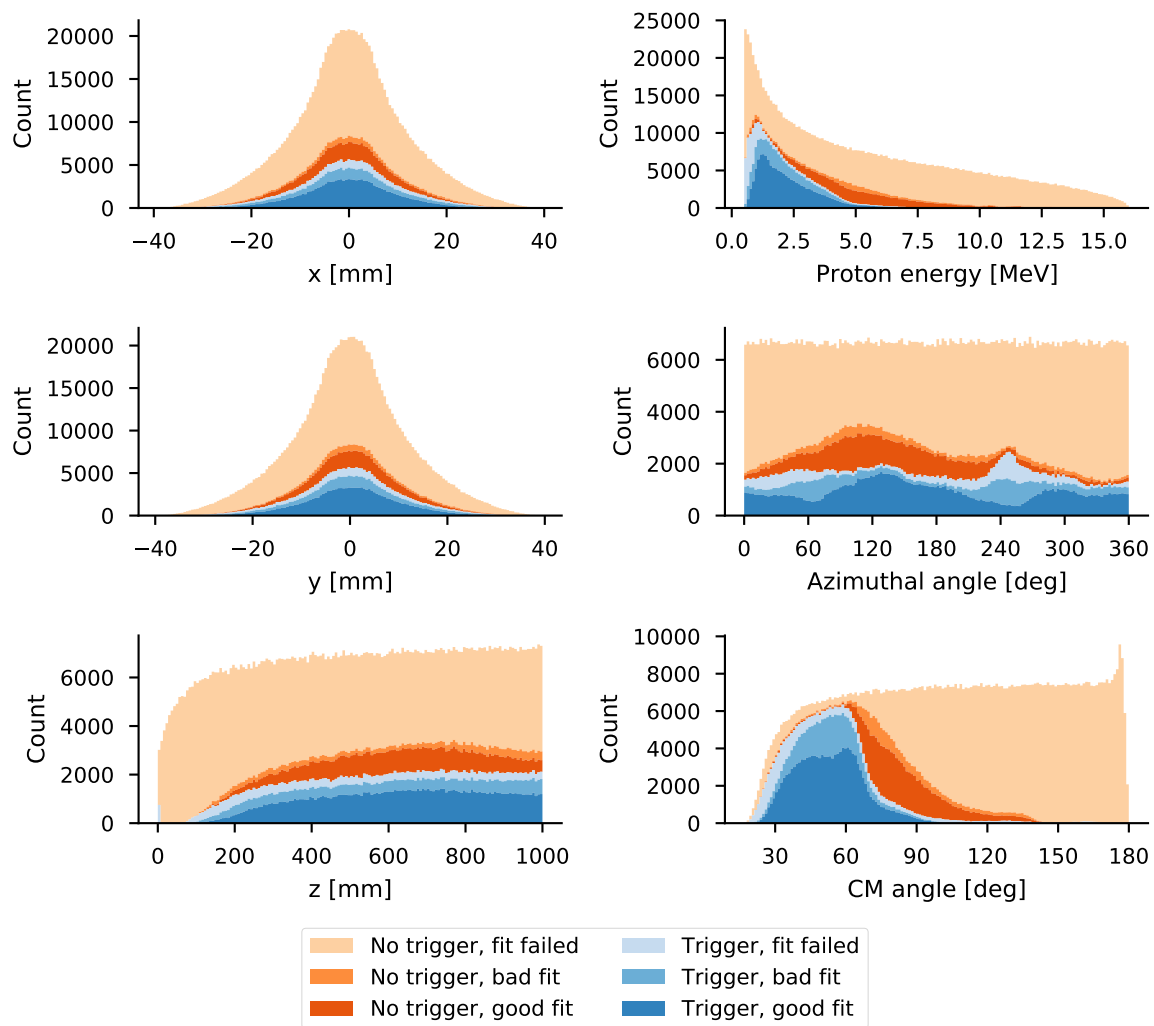


Figure 4.9: Simulated acceptance of the trigger and analysis for trigger parameter set 3.

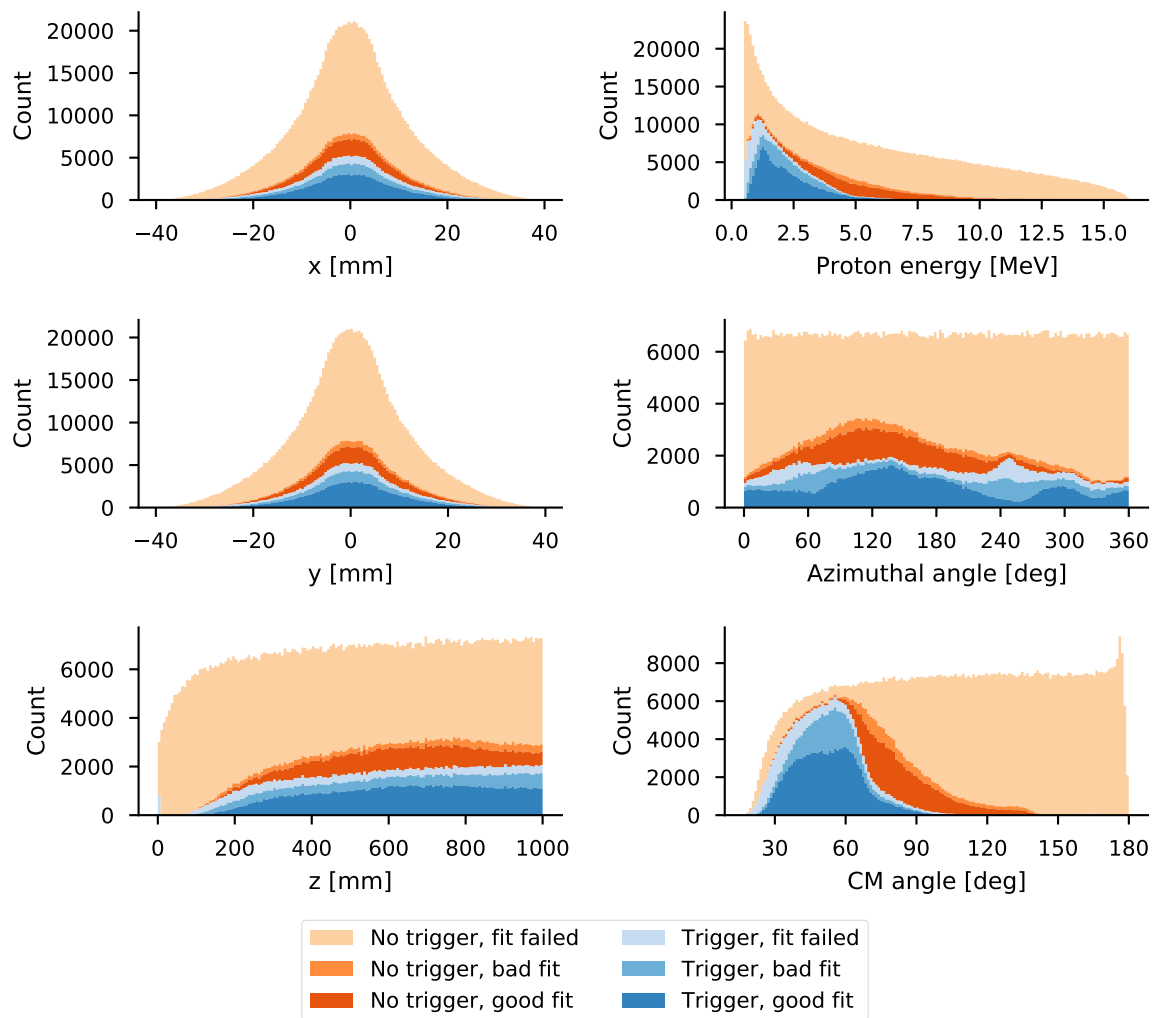


Figure 4.10: Simulated acceptance of the trigger and analysis for trigger parameter set 4.

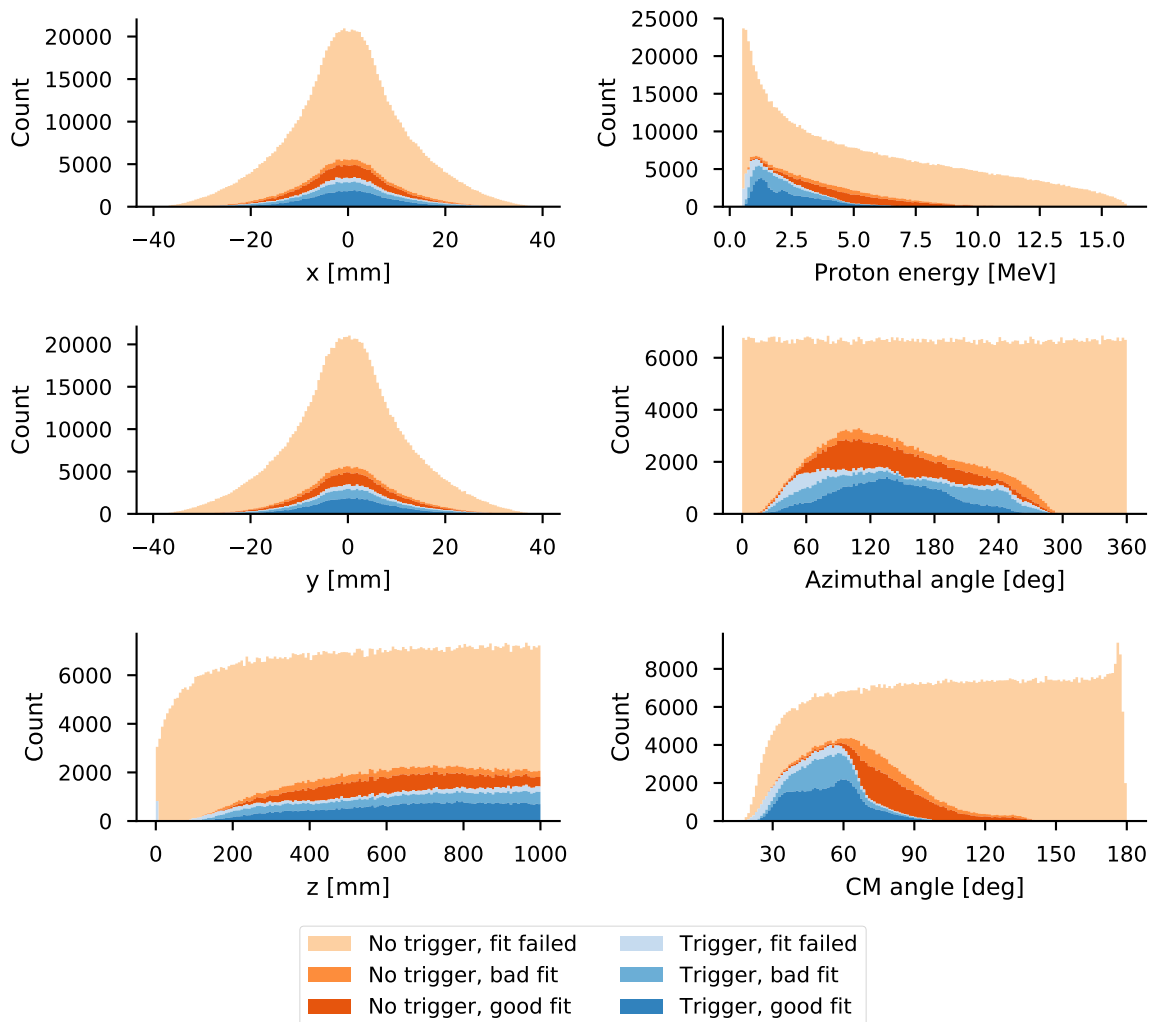


Figure 4.11: Simulated acceptance of the trigger and analysis for trigger parameter set 5. The acceptance was reduced for these runs due to the exclusion of CoBos 4 and 9 from the trigger. This is most visible in the distribution with respect to the azimuthal angle.

to 4.11 also include events that were not successfully processed by the Monte Carlo code. The majority of these events, which are shown in the “trigger, fit failed” and “no trigger, fit failed” groups, failed because they had a very small number of data points remaining after cleaning. Specifically, the fitting algorithm rejects any event with fewer than 50 data points without attempting to fit it as these events tend to be short tracks that are fit poorly. These rejected events are therefore not shown in the χ^2 distributions since no χ^2 values were calculated for them.

This simulated data set was used to calculate the efficiency of the detector as a function of center-of-mass scattering angle and ^{46}Ar vertex energy. To this end, the data were first binned in those two dimensions. The bins were assigned based on the known correct values of the scattering angle and vertex energy used to simulate the tracks—rather than the values reconstructed by the Monte Carlo fit—in order to remove any uncertainties arising from the fit itself. The efficiency in a given 2D bin i was defined as

$$\epsilon_i = \frac{A_i}{N_i}, \quad (4.20)$$

where A_i is the number of accepted events in the bin and N_i is the total number of events simulated in the bin. An “accepted” event can be defined as one that triggers the detector, passes the χ^2 cut, or both. Two-dimensional histograms of the efficiencies are shown in Figs. 4.12 and 4.13.

Statistically, the acceptance or rejection of an event within a bin can be considered to be a Bernoulli random process: the event is accepted with a fixed probability ϵ , which is equal to the efficiency, or rejected with probability $1 - \epsilon$. This implies that the number of accepted counts A_i in each bin should be binomially distributed with variance $N_i\epsilon(1 - \epsilon)$, where N_i is, again, the number of events simulated in that bin. Since the true value of ϵ is unknown, we can approximate the variance with the calculated ϵ_i . This leads to the following formula for the uncertainty of the efficiency:

$$\sigma_{\epsilon,i} = \frac{\sigma_A}{N_i} = \frac{1}{N_i} \sqrt{A_i \left(1 - \frac{A_i}{N_i}\right)}. \quad (4.21)$$

Figures 4.14 to 4.18 show the calculated efficiencies with these error bars as a function of vertex energy for a variety of scattering angles.

The plots shown in this section suggest that the limiting factor for the acceptance in this experiment was the trigger. The low acceptance of the trigger dominated the acceptance of the track reconstruction and fit, especially at forward angles. There are a few factors that likely contributed to this effect:

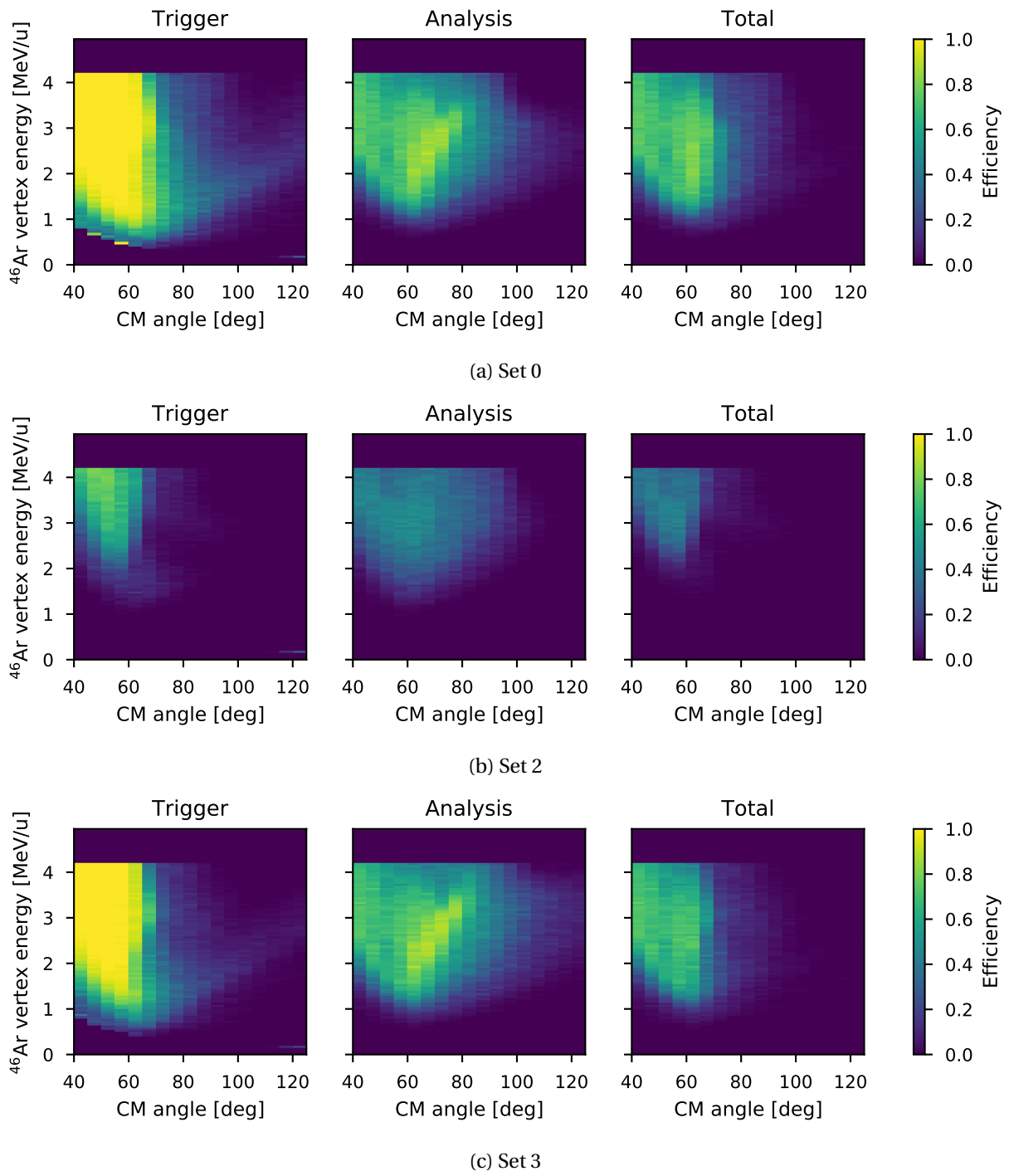
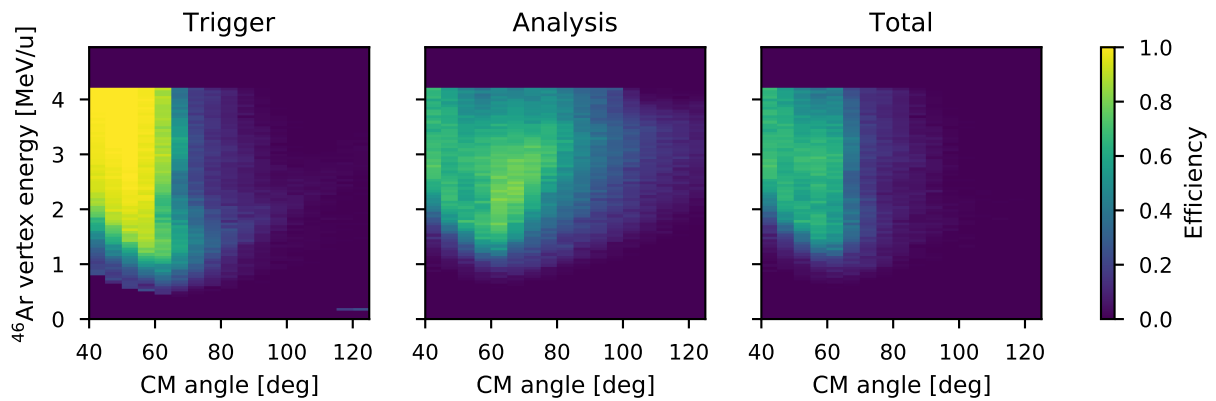
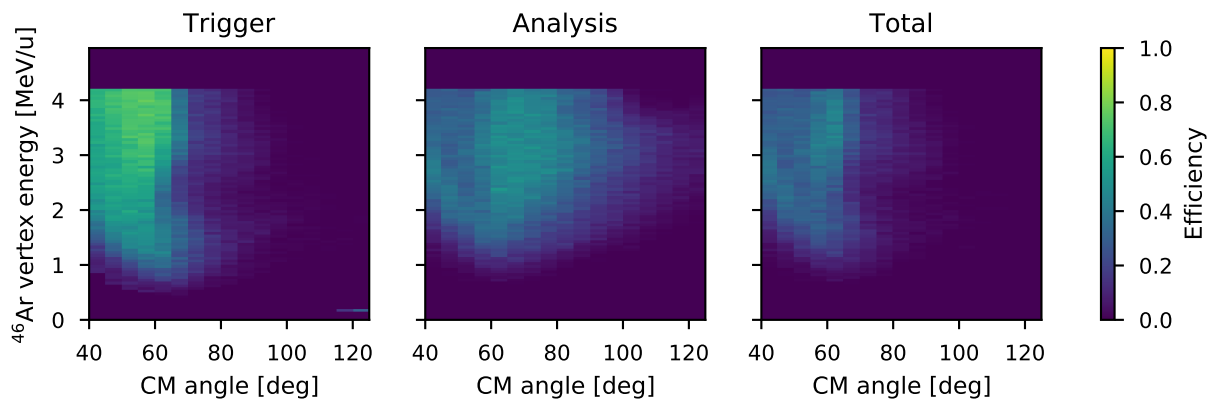


Figure 4.12: Efficiencies of the AT-TPC trigger, the analysis χ^2 cuts, and the total of the two for the first three sets of parameters, plotted as functions of the ^{46}Ar energy at the reaction vertex and the scattering angle in the center of mass frame. The bins used were 5° wide in the angular dimension and 50 keV wide in the energy dimension.



(a) Set 4



(b) Set 5

Figure 4.13: Efficiencies of the AT-TPC trigger, the analysis χ^2 cuts, and the total of the two for the last two sets of parameters. See the caption of Fig. 4.12 for details.

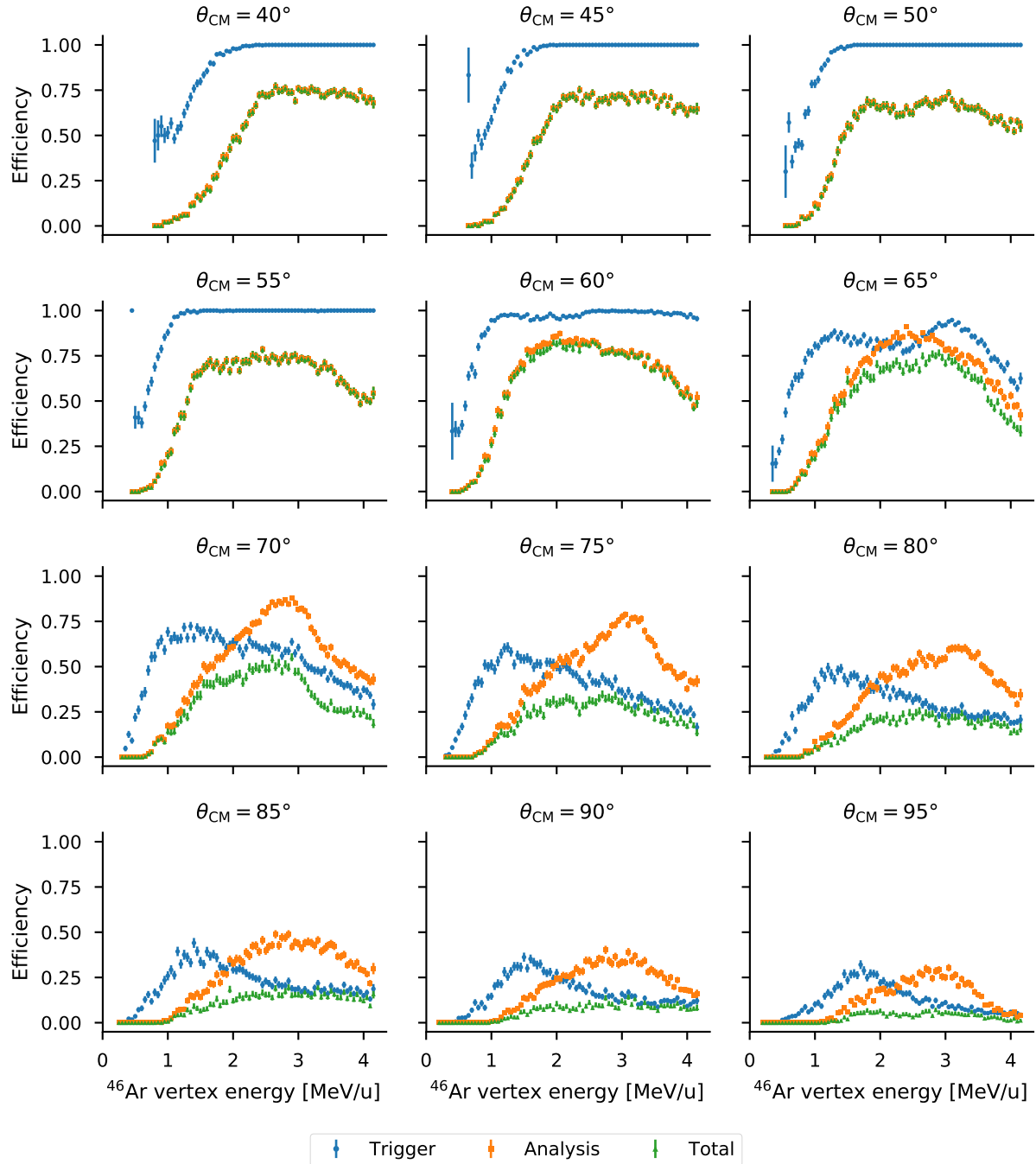


Figure 4.14: Efficiencies for parameter set 0 as a function of ^{46}Ar vertex energy at several scattering angles. The error bars shown are $\pm\sigma_{e,i}$ as defined in Eq. (4.21). The bins used in this plot are the same as those used in the 2D histograms in Figs. 4.12 and 4.13.

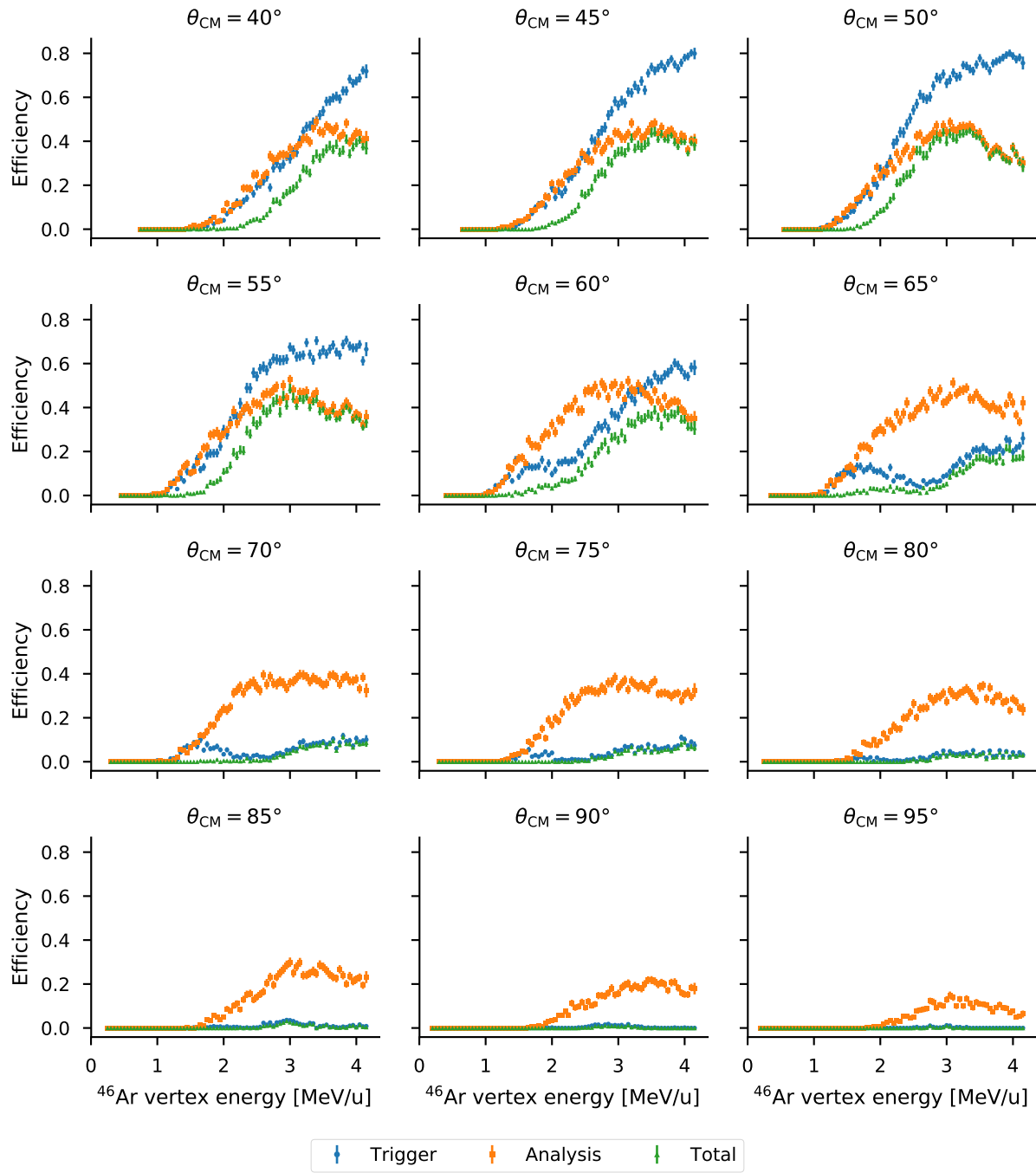


Figure 4.15: Efficiencies for parameter set 2 as a function of ^{46}Ar vertex energy at several scattering angles.

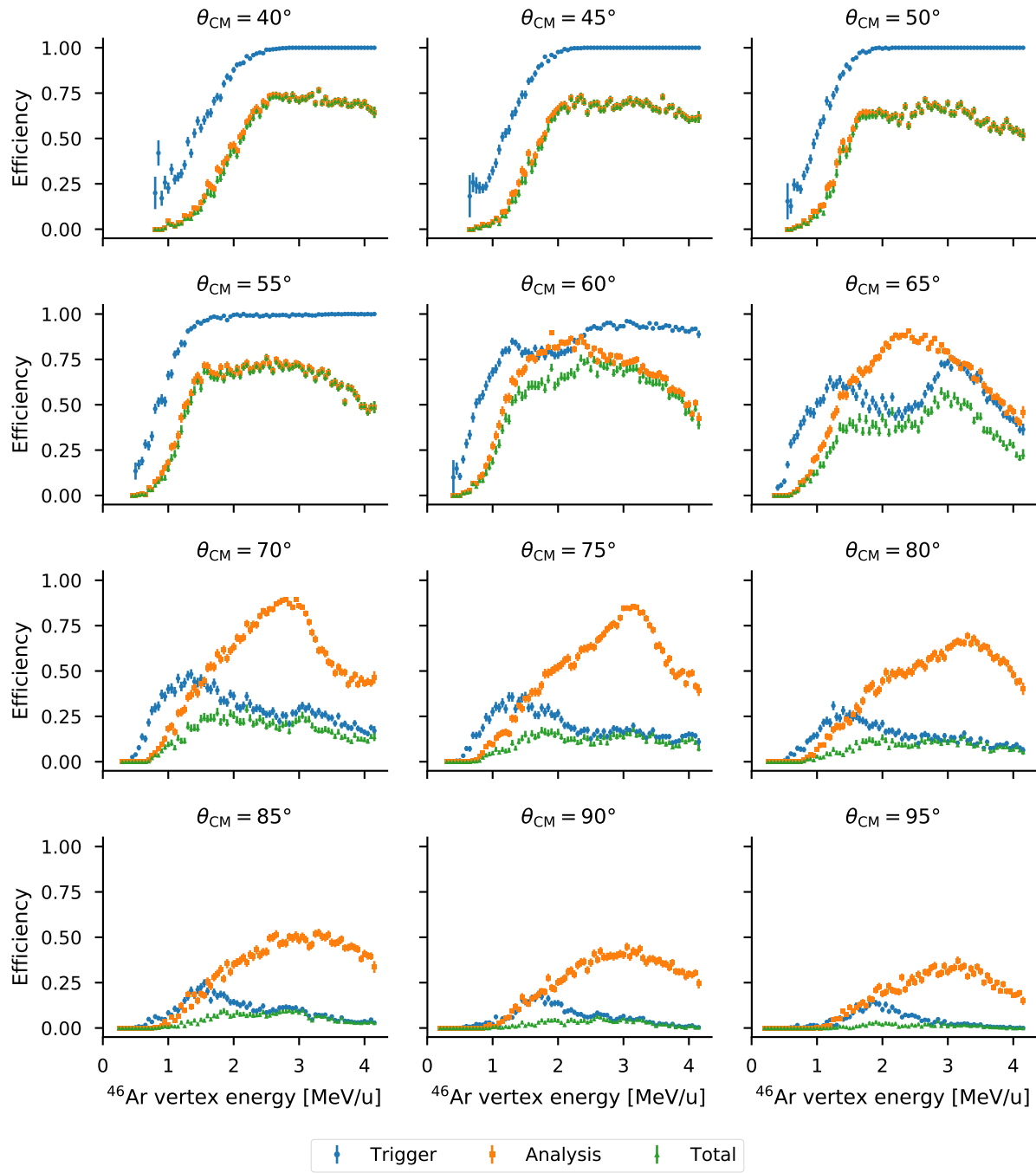


Figure 4.16: Efficiencies for parameter set 3 as a function of ^{46}Ar vertex energy at several scattering angles.

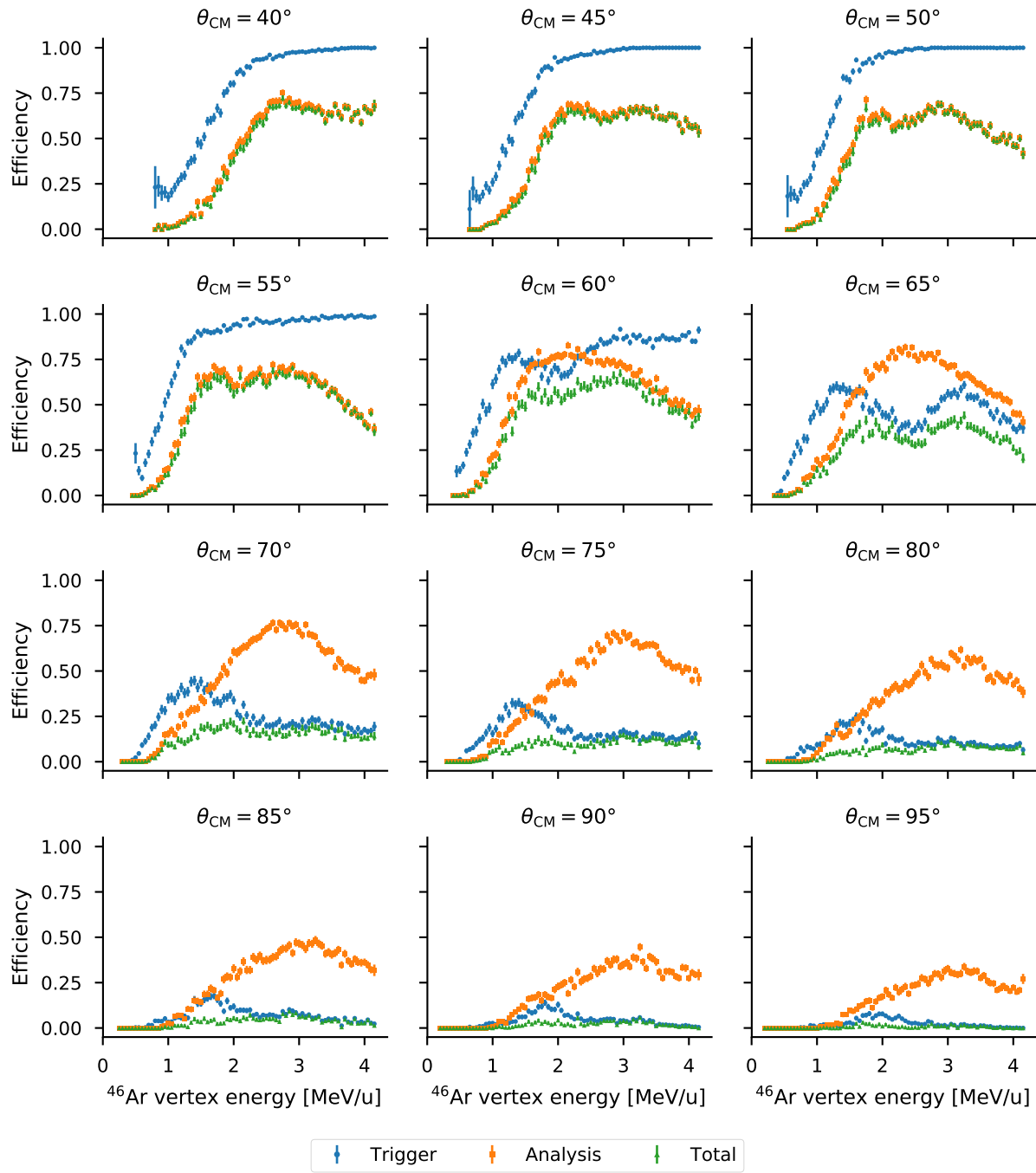


Figure 4.17: Efficiencies for parameter set 4 as a function of ^{46}Ar vertex energy at several scattering angles.

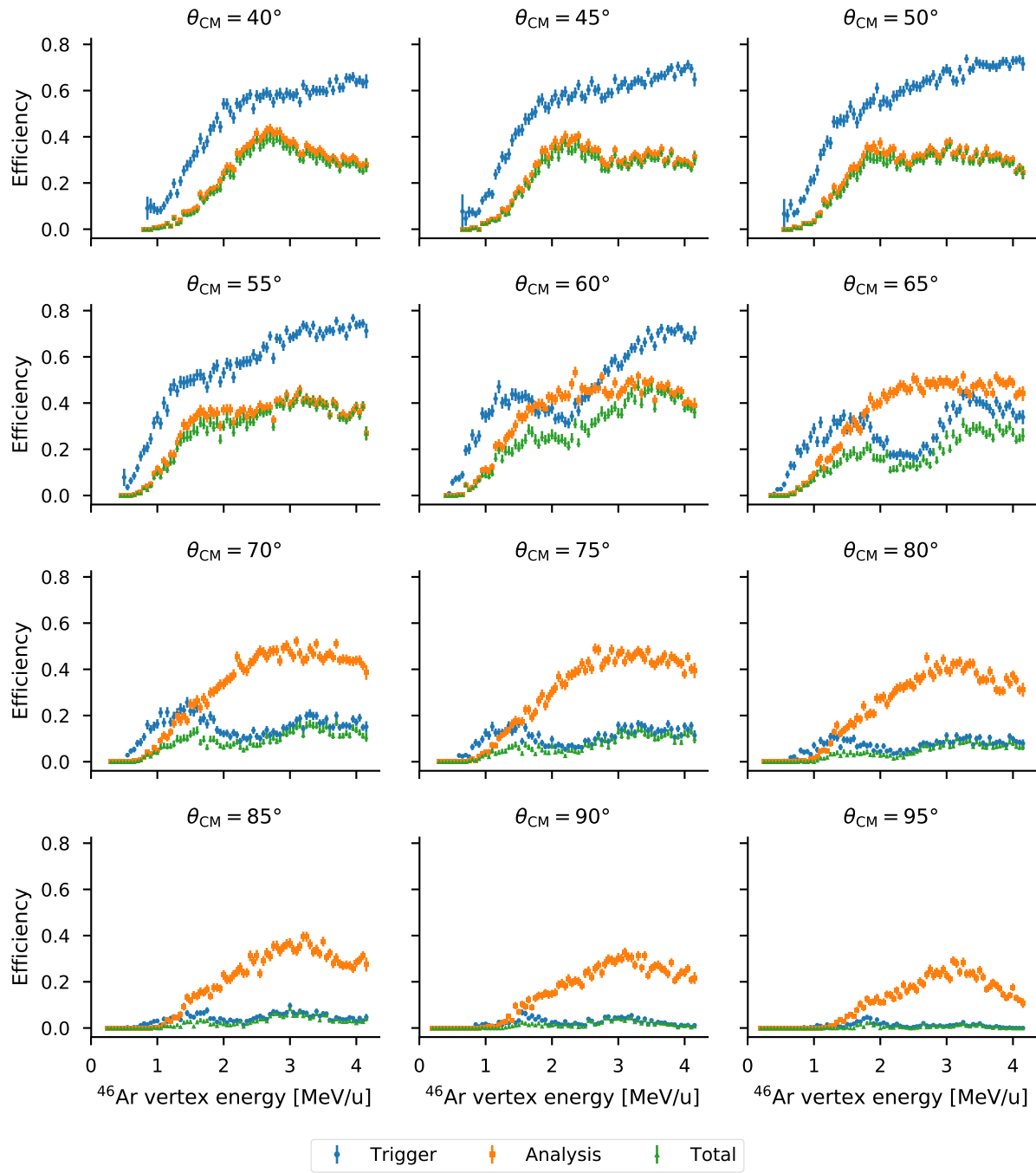


Figure 4.18: Efficiencies for parameter set 5 as a function of ^{46}Ar vertex energy at several scattering angles.

1. Higher-energy protons do not generally stop inside the active volume of the detector. Instead, they spiral through the volume at a nearly constant energy, far from the peak of the Bragg curve, and free fewer electrons per unit track length. This creates smaller signals in the electronics that are less likely to rise above threshold, preventing individual channels from triggering.
2. Events at very forward angles illuminate fewer pads on the sensor plane, leading to lower multiplicities. In principle, tilting the detector should address this since it spreads out the projection of the beam—and therefore the projection of forward events—over more pads; however, the particular combination of drift velocity, tilt angle, and magnetic field in this experiment combined to produce a Lorentz angle that almost perfectly canceled the tilt.
3. Since the MuTAnT module was not available during the experiment, the trigger used was not a true global multiplicity trigger, but instead a set of CoBo-level multiplicity triggers combined using a logical OR operation. Thus, events that activated few pads in many CoBos were cut if the multiplicity in each CoBo was below threshold, even if the event had a high global multiplicity.

Many of these effects can be addressed in future experiments by using the MuTAnT as a trigger and by carefully choosing the combination of gas pressure and fields.

4.3 Simulated resolution

The simulated data set described in Section 4.2 can also be used to establish a benchmark for the expected resolution of the detector for $^{46}\text{Ar}(\text{p}, \text{p}')$ scattering events. This was done by finding the difference between the reconstructed track parameters and the known correct parameters that were used to simulate each event. The distributions of this difference for the six track parameters are shown in Fig. 4.19.

Table 4.4 shows the output of fitting functions to these distributions of deviations. The distributions for Δx_0 , Δy_0 , ΔE_{pos} , and $E_{\text{kin}} - E_{\text{pos}}$ were fit using a Laplace distribution, which was defined as

$$f(x, \mu, b, A) = \frac{A}{2b} \exp\left(-\frac{|x - \mu|}{b}\right). \quad (4.22)$$

In the nomenclature used in Table 4.4, μ serves as the centroid for this distribution, b is the width parameter, and A is the normalization parameter. The remaining distributions were fit with a Gaussian

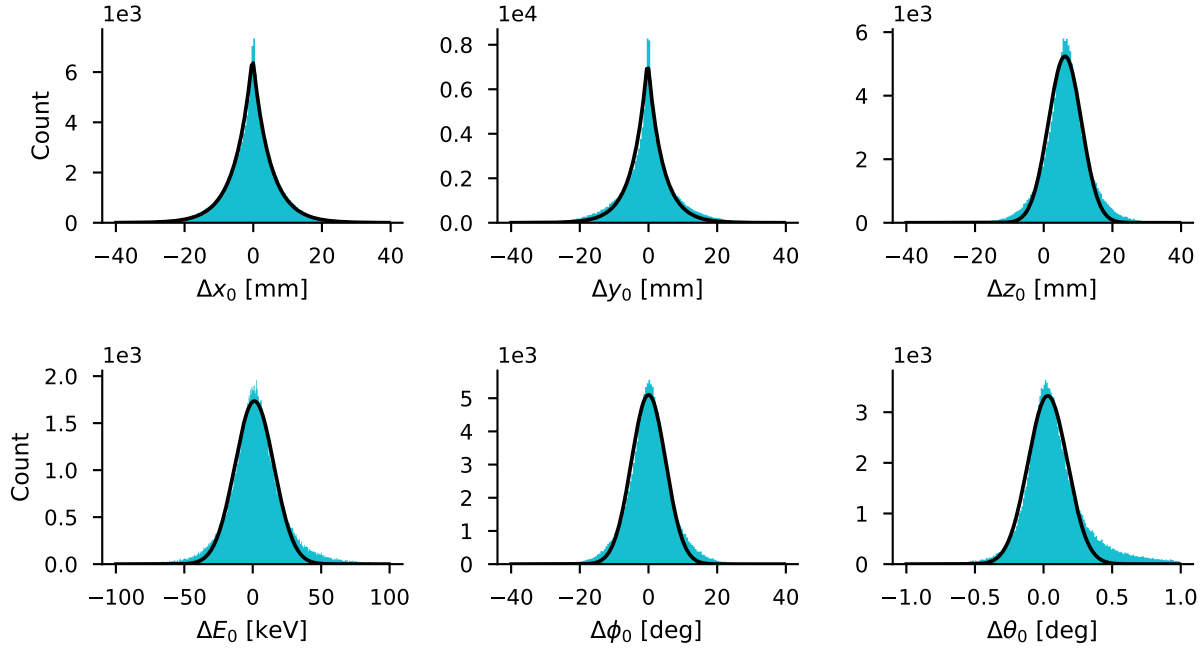


Figure 4.19: Simulated resolution of the AT-TPC. These six plots show the error in the reconstruction of each of the six track parameters, defined as the reconstructed value minus the correct value. The results of the fits to these distributions are given in Table 4.4.

Variable	Distribution	Centroid	Width	FWHM	Units	Normalization
Δx_0	Laplace	-0.210	5.07	7.03	mm	6.72×10^4
Δy_0	Laplace	-0.245	4.30	5.96	mm	6.32×10^4
Δz_0	Gaussian	6.19	4.81	11.3	mm	6.32×10^4
ΔE_0	Gaussian	1.18	14.3	33.7	keV	6.21×10^4
$\Delta \phi_0$	Gaussian	2.06×10^{-2}	5.00	11.8	deg	6.39×10^4
$\Delta \theta_0$	Gaussian	3.05×10^{-2}	0.144	0.339	deg	1.20×10^3
ΔE_{kin}	Gaussian	-7.25	244	575	keV/u	6.64×10^5
ΔE_{pos}	Laplace	20.4	18.0	25.0	keV/u	1.36×10^5
$E_{\text{kin}} - E_{\text{pos}}$	Laplace	-48.0	229	317	keV/u	7.14×10^5

Table 4.4: Results of fitting the distributions of parameter and energy deviations from Figs. 4.19 and 4.21. The Laplace and Gaussian distributions are defined in Eqs. (4.22) and (4.23), respectively. The units listed apply to both the centroid and width parameters. The full width at half-maximum (FWHM) was defined as $2\sigma\sqrt{2\log(2)}$ for the Gaussian distributions and $2b\log(2)$ for the Laplace distributions.

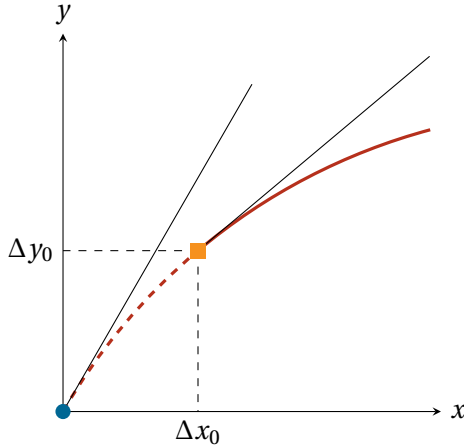


Figure 4.20: Illustration of relationship between uncertainty in vertex location and error in azimuthal angle. The reconstructed vertex is marked with an orange square, while the actual vertex location is marked with a blue circle. The red curve represents the proton track. The tangent lines at these two locations have very different slopes.

distribution

$$f(x, \mu, \sigma, A) = \frac{A}{\sqrt{2\sigma^2\pi}} \exp\left(-\frac{(x-\mu)^2}{2\sigma^2}\right), \quad (4.23)$$

where μ is the centroid, σ is the width parameter, and A is the normalization parameter. These results show a FWHM resolution of 33.7 keV for the proton energy and 0.339° for the scattering angle in the laboratory frame. The z position of the proton was resolved to within 11.3 mm at FWHM.

One unusual aspect of these results is the poor resolution found for the azimuthal angle ϕ_0 . The error in ϕ_0 is caused by the uncertainty in the extrapolation from the first data point back to the reaction vertex. The uncertainty in the vertex location leads to a correlated uncertainty in the azimuthal angle. This is shown by the difference in the tangent lines at the actual vertex and the reconstructed vertex in Fig. 4.20, which corresponds to $\Delta\phi_0$.

The parameters of the simulated tracks can also be used to estimate how precisely the ^{46}Ar vertex energy can be reconstructed using the same techniques as with data (see Section 3.7). The kinematic and positional vertex energies can be calculated for both the reconstructed parameters and the parameters used to simulate the tracks, providing an estimate of the resolution. The results of this comparison are plotted in Fig. 4.21, which shows distributions of the deviation in kinematic vertex energy and positional vertex energy as well as the difference between the two. The kinematic vertex energy was reconstructed

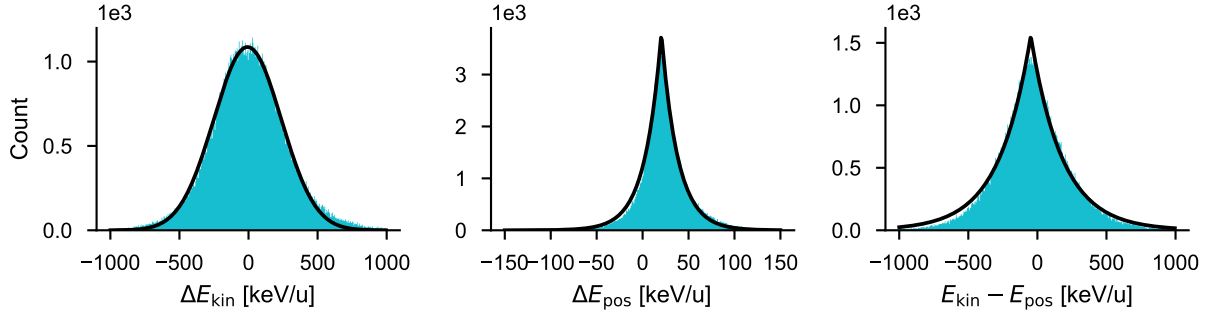


Figure 4.21: Simulated resolution of the two energy reconstruction techniques from Section 3.7. The widths of the distributions are given in Table 4.4. ΔE_{kin} and ΔE_{pos} are defined as the difference between the energies as calculated from the reconstructed parameters and the known correct parameters. For the rightmost plot of $E_{\text{kin}} - E_{\text{pos}}$, both values were found from the reconstructed parameters. The difference between the two energies for the known correct parameters is not shown since those two values are identical. Note that the horizontal scale is different on the center plot.

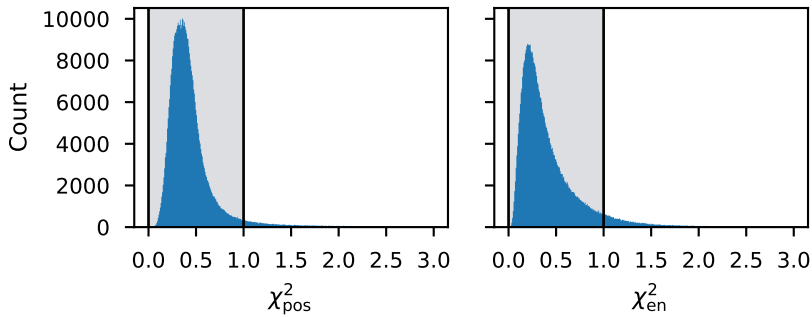


Figure 4.22: Distributions of the objective function components for simulated events drawn from the R matrix calculation results. Each distribution was cut at 1.0, discarding all events with a larger value of χ^2 . This is the same cut that was used for the flat distribution (see Figs. 4.5 and 4.6).

to a resolution of 575 keV/u, the positional vertex energy was resolved to within 42.4 keV/u, and the difference between the two had a resolution of 539 keV/u, all at FWHM.

4.4 R matrix simulation

A second simulation was performed to assess the AT-TPC's ability to resolve the resonances that were expected in the $^{46}\text{Ar}(\text{p}, \text{p}')$ measurement. This was done by simulating approximately 5.5×10^5 events following a distribution derived from an R matrix calculation as described in Section 4.1.1. Of these events, approximately 3.4×10^5 passed the simulated trigger cuts and the χ^2 cuts shown in Fig. 4.22.

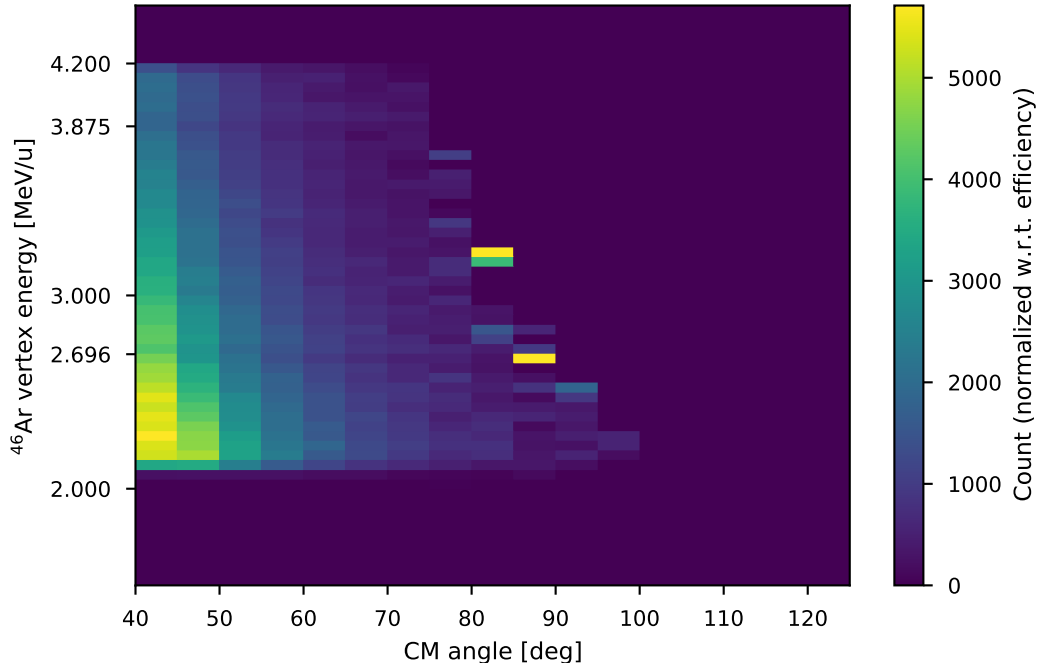


Figure 4.23: Two-dimensional histogram of results from the R matrix-based simulation. The two expected resonance locations are marked on the vertical axis at 2.696 MeV/u and 3.875 MeV/u. The two individual bright bins at 80° and 85° are artifacts from dividing by the very small number of counts in those bins.

After applying the χ^2 cut, the remaining events were binned based on their reconstructed positional ^{46}Ar vertex energies and center-of-mass scattering angles. The reconstructed values were used instead of the known correct values since the purpose of this particular simulation was to see how well the detector and fit could measure the resonances. The binned data were then normalized with respect to the total efficiency calculated earlier in Section 4.2.

Figure 4.23 shows a two-dimensional histogram of the results of the simulation. The resonances corresponding to the ground state and first excited state are visible as faint horizontal depressions in the color scale at energies of 2.696 MeV/u and 3.875 MeV/u, respectively. These energies differ by a small amount from the resonance energies listed in Table 4.1 since those correspond to the incoming proton energies in the center-of-mass frame while the simulated energies in Fig. 4.23 correspond to the ^{46}Ar energies in the laboratory frame. The two values are related by Eqs. (4.12) and (4.16) from Pages 63 and 64.

Figure 4.24 shows excitation functions from this simulation taken at a number of different center-of-mass angles. The resonances are particularly visible in the excitation functions for center-of-mass angles of 55° and 60°. This is partially because these are some of the largest angles where the efficiency

of the trigger is still large enough to accept many events. Larger angles correspond to smaller impact parameters and more-central collisions, and therefore should show larger resonances as seen in the R matrix calculation results in Fig. 4.2. However, when the efficiency becomes too small, the low statistics prevent a conclusive determination of whether or not the resonance is observed. The statistics at higher center-of-mass angles are naturally decreasing since the Rutherford cross section approaches zero as θ_{CM} approaches 180° .

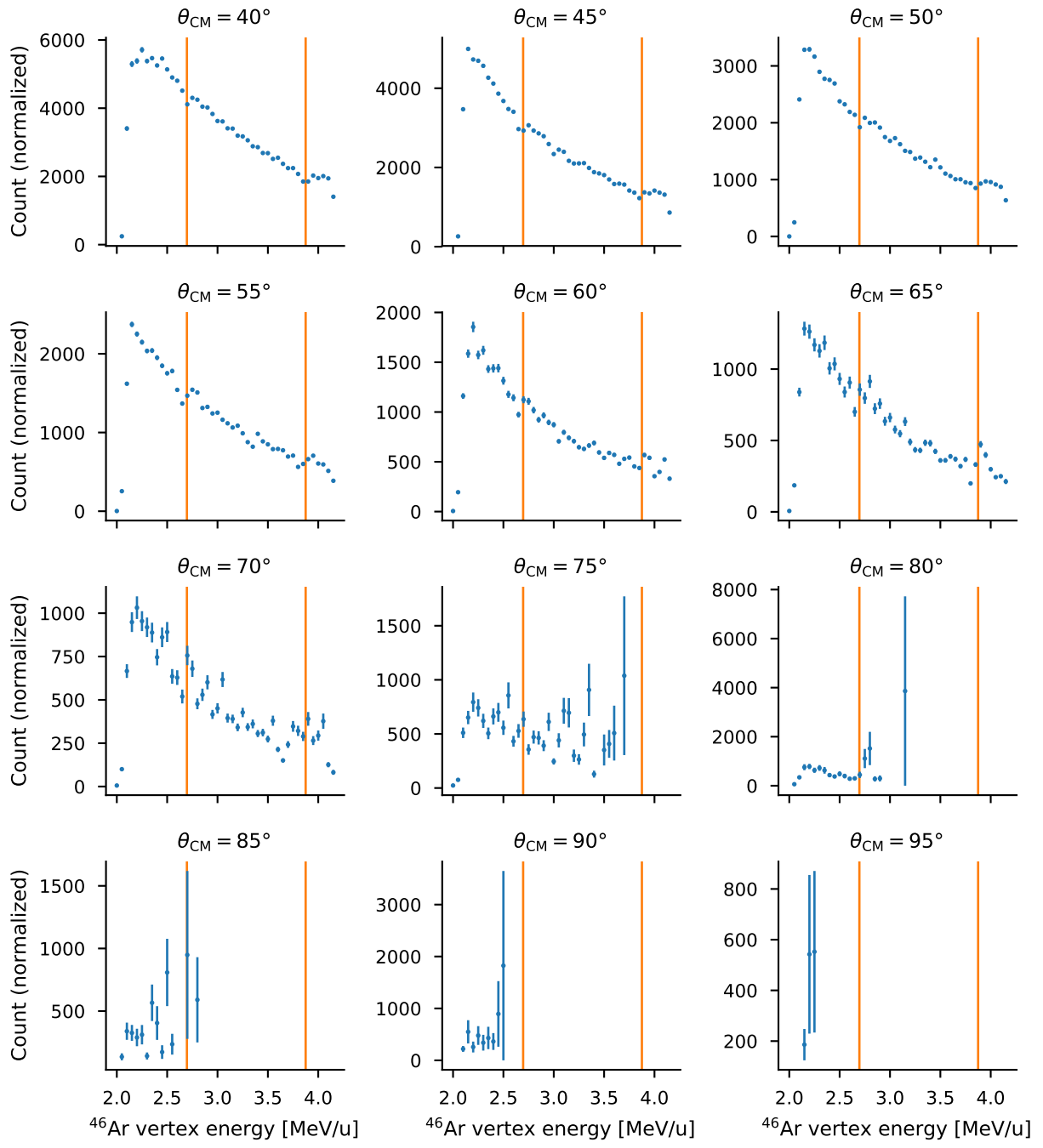


Figure 4.24: Excitation functions derived from the *R* matrix simulation. The expected locations of the two resonances are shown with vertical orange lines.

CHAPTER 5

EXPERIMENT

This chapter describes an experiment that was performed at the National Superconducting Cyclotron Laboratory (NSCL) to measure the reaction $^{46}\text{Ar}(\text{p}, \text{p}')$. The experiment, which was assigned the NSCL experiment number e15503b ran from the morning of September 9, 2015, through the evening of September 20, 2015. The description begins with an overview of the beam production methods and the detector setup used to measure the reaction. Following that is a description of the parts of the analysis process that are particular to this experiment; the general analysis process was described in Chapter 3. Finally, the experimental results are shown and discussed.

5.1 Beam production

The beam of ^{46}Ar used in this experiment was produced by the Coupled Cyclotron Facility [34] at the National Superconducting Cyclotron Laboratory (NSCL) at Michigan State University. A diagram of this facility's beam line is shown in Fig. 5.1. Beam production began with a primary beam of ^{48}Ca produced by a superconducting ion source and accelerated to a final energy of 140 MeV/u by the coupled cyclotrons. The primary beam was then impinged upon a beryllium target to produce a mixture of nuclei by the process of projectile fragmentation. These nuclei were separated in the A1900 fragment separator (see Fig. 5.2), a device which uses four large dipole magnets to separate particles based on their magnetic rigidity [36]. Particles with a different rigidity from the desired ^{46}Ar fragments follow different paths through the separator and are filtered out of the beam using adjustable slits.

The ^{46}Ar beam exited the A1900 at a much higher energy than what was needed to see the resonances in this experiment. However, the primary beam cannot be accelerated to a lower initial energy since at very low energies, fragmentation is not possible. This issue was addressed by stopping the high-energy beam particles and then re-accelerating them to a lower final energy. To accomplish this, the beam was sent into a helium-filled [53] linear gas cell where it was stopped. Electric fields were then used to extract the stopped ions from the gas cell and transport them to an electron beam ion source (EBIS), where their charge states were increased from 1+ to 17+ to make acceleration possible. Finally, the ions were injected into ReA3, a linear accelerator (linac), and re-accelerated to a final energy of 4.6 MeV/u.

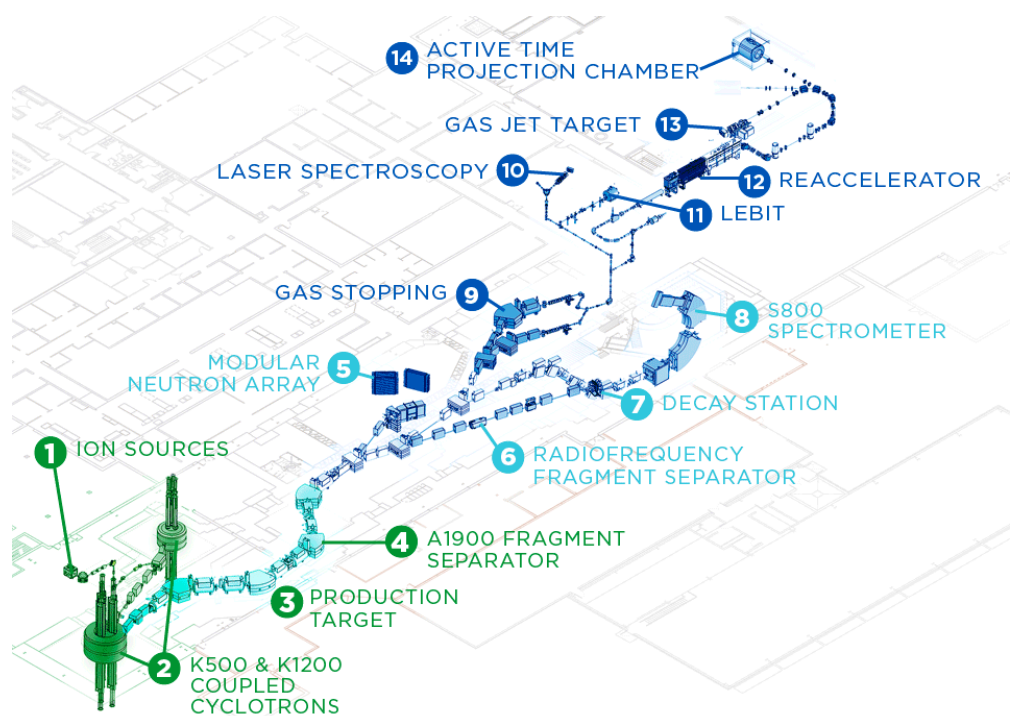


Figure 5.1: A diagram of the NSCL beamline, with some regions of the facility labeled. The beam starts at the ion sources (label 1) and ends at the AT-TPC (label 14). (Reproduced from <http://nscl.msu.edu/public/virtual-tour.html>.)

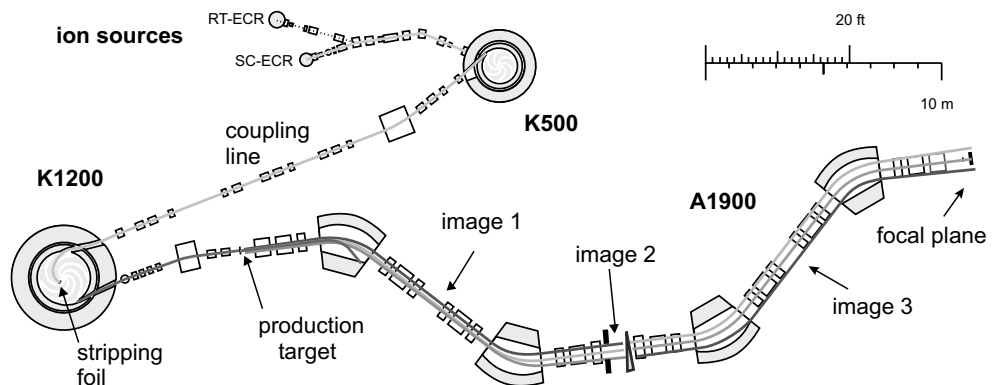


Figure 5.2: The A1900 fragment separator and the coupled cyclotrons. (Reproduced from [36].)

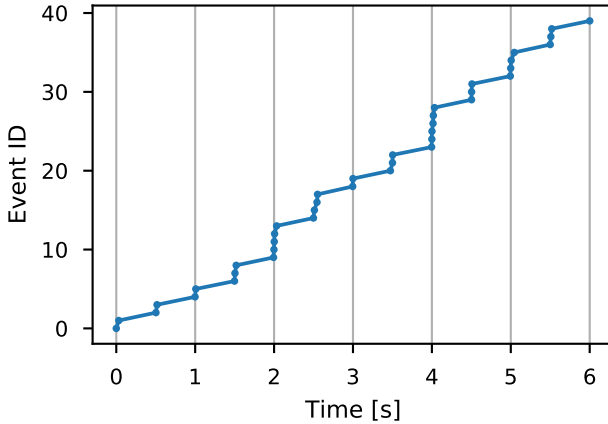


Figure 5.3: Timing of events recorded by the GET electronics. Particles arrived in bunches at a rate of approximately 2 Hz. Note that this only shows events that triggered the electronics; in reality, many more nuclei arrived in each bunch.

This re-acceleration process is very useful as it allows rare isotope beams to be produced at much lower energies than was previously possible; however, the re-accelerated beams do have a few unique characteristics that must be accounted for. The primary complication introduced is the time structure of the re-accelerated beam. Particles are extracted from the EBIS with a period on the order of milliseconds, creating large, widely spaced bunches of particles (see Fig. 5.3). Additionally, the first stage of the ReA3 linac was operated in a pulsed mode to address electrical power considerations, further contributing to bunching. This resulted in a very high instantaneous beam rate with a low duty cycle, causing a significant degree of pileup in the AT-TPC, as shown in Fig. 5.4. These high-multiplicity events are very difficult to analyze, but fortunately they can be easily filtered out using data from an ion chamber upstream of the AT-TPC, as described in Section 5.3.3 below.

In addition to bunching the beam, the duration of the charge breeding process allows some of the beam nuclei to decay. While the 8.4(6) s half-life [38] of ^{46}Ar is very long compared to the time it takes the particles to travel from the production target to the EBIS, the nuclei then spend on the order of milliseconds in the EBIS. During that time, a small but significant number of ^{46}Ar nuclei β -decay into ^{46}K , a few of which further β -decay into ^{46}Ca with a half-life of 105(10) s [38]. These decay products have the same mass as ^{46}Ar and some of them leave the EBIS with the same charge state, so they are transmitted through the pre-separator and accelerated to the same final velocity by the linac. Fortunately, it is possible to separate the ^{46}Ar from its decay products using the signals from the ion chamber, which will also

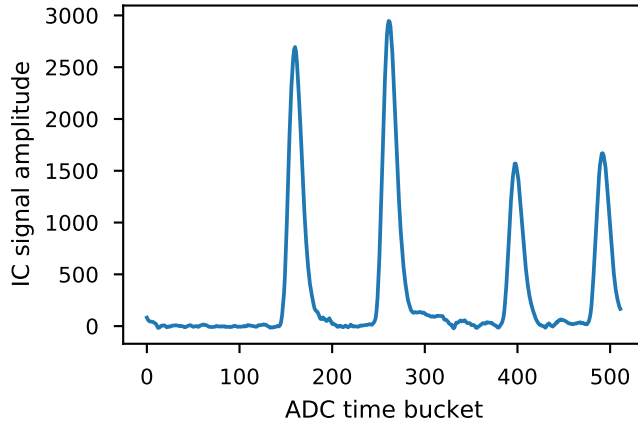


Figure 5.4: A signal from the ion chamber (see Section 5.2.2) from an event where four particles entered the detector.

be described in Section 5.3.3 below.

5.2 Detection setup

The beam of ^{46}Ar was measured using the AT-TPC, which was described in detail in Chapter 2. This section will cover the way the detector was set up in this experiment.

5.2.1 AT-TPC setup

The AT-TPC was mounted inside its solenoid in the ReA3 experimental area at the NSCL and connected to the ReA3 beam line. The jack on the detector's support carriage was used to raise the downstream end of the detector until its central axis was tilted upward by an angle of 6.2° with respect to the central axis of the solenoid. The GET electronics were then connected to the TPC.

The active volume of the detector was filled with isobutane gas at a pressure of 19.2 torr and the shielding volume was filled with nitrogen gas at the same pressure. Both gases were circulated through the detector and continuously replaced at a rate of $83 \text{ cm}^3/\text{min}$ to maintain a low level of contaminants in the gas.

A potential of -9.0 kV was applied to the AT-TPC's cathode with respect to its grounded anode, creating an electric field of approximately 9.5 kV/m in the active volume. The solenoid was energized and produced a magnetic field of 0.997 T as measured by a Hall probe mounted on the axis of the magnet and

flush with the upstream end of the bore. According to a field map of the magnet, this corresponds to a magnetic field of 1.68 T in the center of the bore where the TPC is located. The solenoid's power supply was disconnected after the magnet was energized, leaving the magnet running in persistent mode.

To amplify the ionization electrons, a potential of -450 . V was applied to the Micromegas mesh with respect to the grounded pad plane. In later runs, this was reduced to -446 . V to reduce sparking between the mesh and the pads. This high potential difference was required to detect the relatively small amount of charge produced by the scattered protons even though it caused a relatively high current of around $8\ \mu\text{A}$ to flow between the pads and the mesh when the heavily ionizing ^{46}Ar nuclei passed through the detector. A potential of -500 . V was applied to the field cage ring nearest to the Micromegas to ensure the linearity of the electric field between the end of the field cage and the negatively biased Micromegas mesh.

5.2.2 Ion chamber and secondary DAQ

A small, cylindrical ion chamber was constructed and inserted into the beam line just upstream of the AT-TPC. The chamber is 5 cm long and contains 5 thin foils mounted at equal intervals along the axial direction. The foils have a diameter of 1 in and consist of approximately $400\ \mu\text{g}/\text{cm}^2$ of aluminum evaporated on a plastic substrate. The outermost two foils are grounded and serve as entrance and exit windows, while the inner three foils establish equipotentials for the electric field. The electron drift direction is parallel to the beam, and signals are read out from the center foil, which is kept at a potential of 100 V relative to the outermost foils. Like the active volume of the AT-TPC, the ion chamber was filled with isobutane gas at a pressure of 19.2 torr.

This ion chamber served two purposes. First, the energy loss data from the ion chamber was used to help separate the desired beam particles from contaminants. Second, the timing signal from the ion chamber was used to prevent the AT-TPC from triggering on events that were not correlated with a beam particle and to establish an absolute, global time reference for each event that corresponded to when a beam particle entered the active volume of the AT-TPC. The data from the ion chamber was digitized using a 12-bit flash ADC VME module and recorded using a separate DAQ from the main system. This auxiliary DAQ system also digitized and recorded the trigger signal output to the CoBos and a signal derived from the Micromegas mesh.

5.2.3 Trigger

The final version of the MuTAnT board was not yet available when this experiment was run, so the GET electronics had to be triggered externally. Each CoBo was configured to compare its total multiplicity signal to a multiplicity threshold with an integration window of 300 cycles of the 25 MHz read clock, or 12 μ s. Whenever the CoBo multiplicity exceeded the threshold, the CoBo would output a trigger signal through a LEMO connector on its front panel. The CoBos also output a second signal through another connector whenever they were busy processing an event. For a more thorough description of the CoBo multiplicity trigger, see Section 4.1.3. The trigger thresholds are listed in Table 4.3 on Page 69.

To build a trigger, the multiplicity trigger signals from the 10 CoBos were collected and combined with a logical OR operation in a VME module to produce a global multiplicity trigger signal. The busy signals were combined in the same way to produce a global busy signal. These two global signals were then combined to produce a signal that was true when any CoBo had a multiplicity trigger and no CoBo was busy. More formally, for CoBo multiplicity signals M_i and busy signals B_i , the trigger logic derived from the GET electronics was

$$T_{\text{GET}} = (M_0 \vee M_1 \vee \dots \vee M_9) \wedge \overline{(B_0 \vee B_1 \vee \dots \vee B_9)}. \quad (5.1)$$

In addition to the signals from the GET electronics, a trigger signal was derived from the ion chamber output using a discriminator module. This ion chamber trigger was then delayed and compared to a coincidence window which was opened by the CoBo multiplicity trigger. If the delayed ion chamber signal fell within this coincidence window, a master trigger signal was generated and distributed to the 10 CoBos.

The master trigger was based on the delayed ion chamber signal to ensure that the trigger timing was always constant with respect to the arrival of the beam particle into the AT-TPC, rather than the delayed time of arrival of the drifting electrons. The latter is highly dependent on the trajectory of the charged particle emitted during the reaction, and therefore it does not provide a good timing reference. This reference is essential to establish the relationship between the measured time of the signals and the position along the drift direction of the electrons since this relationship is used to deduce the absolute position of the tracks in this direction.

Finally, in addition to the master trigger above, the detector was also periodically triggered on a downscaled version of the raw trigger signal from the ion chamber. This was done so that the detector

would record a few unreacted beam events every second for calibration purposes.

5.2.4 Excluding beam events

The GET electronics provide the ability to remove individual pads from the multiplicity trigger described in Section 5.2.3 and to adjust the gain of the charge-sensitive preamplifier on each channel independently (see Fig. 4.3 on Page 66 for a schematic of the channel, where the preamplifier is labeled “CSA”). These features are crucial as the pad-level trigger suppression allows unreacted beam events to be excluded from the trigger, and the channel-level preamplifier gain setting allows a low-gain region to be established where the strongly ionizing beam particles are projected onto the sensor plane.

These regions were found by taking a short data run with no beam suppression. Approximately 100 events were then analyzed and the integrated charge deposited in each pad was accumulated for all events into one array. An empirically chosen threshold was applied to select the set of pads that were activated most often in this set of events. Since scattering events are rare compared to unreacted beam events, this set of pads corresponds to the set of pads illuminated by the beam. These pads were then set to a low gain and removed from the trigger. The exclusion regions used in the experiment were shown in Fig. 4.4 on Page 70.

5.3 Analysis and results

The analysis process for AT-TPC data was described in general in Chapter 3. This section will cover the specifics of the analysis done on the ^{46}Ar data, and then the results of the analysis will be shown.

5.3.1 Correlating VME and GET events

As described in Section 5.2.2, a separate VME DAQ was used to record signals from the ion chamber and Micromegas mesh. The ion chamber signal is required to select ^{46}Ar events and exclude beam contaminants, so each event recorded by the VME DAQ must be paired with its corresponding event in the GET DAQ. In principle, this can easily be done by comparing the event ID recorded in each system: the two IDs should be perfectly correlated since the VME DAQ generated the trigger signals that were sent to the GET DAQ. However, in practice, the two sets of event IDs tended to drift out of alignment over the course of longer runs.

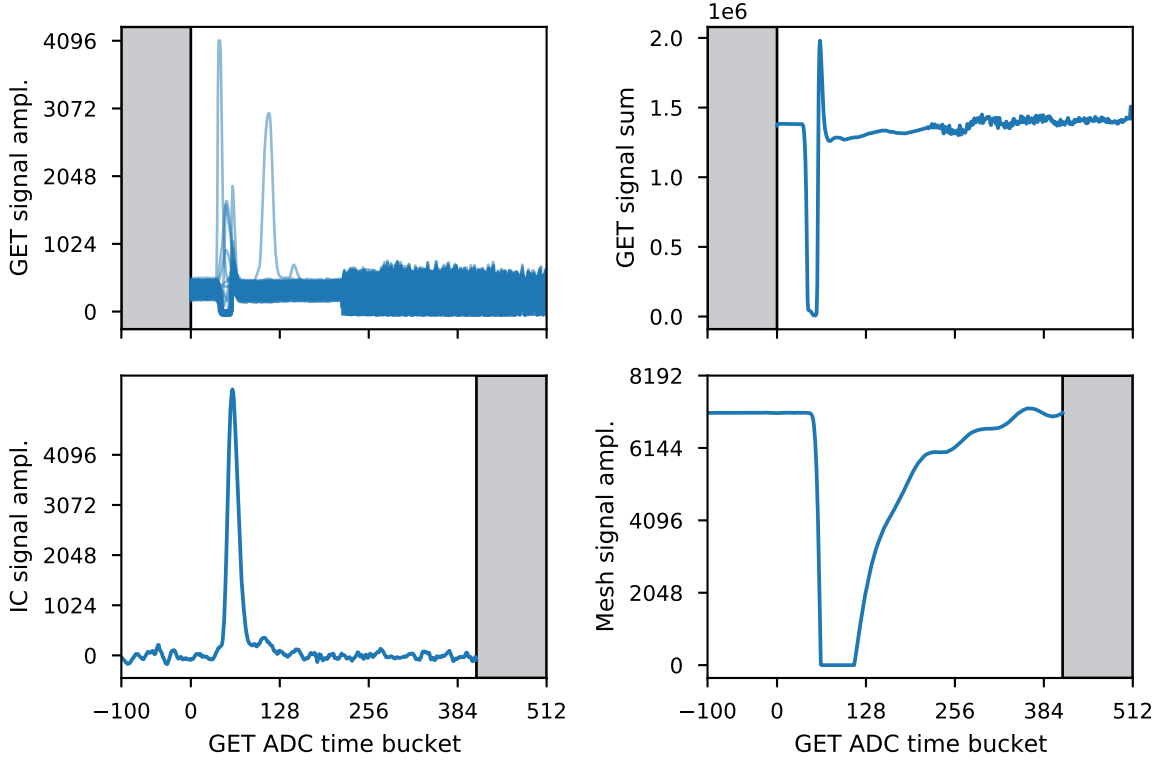


Figure 5.5: Plots of various signals in a spark-like event. The top left plot shows the individual signals in the GET electronics, and the top right plot shows the sum of these signals. The bottom left plot contains the signal from the ion chamber, and the bottom right plot shows the signal from the Micromegas mesh. The gray regions indicate domains in which there is no data. The time buckets in the two DAQ systems are of the same width, but are offset by 100 due to the trigger delay.

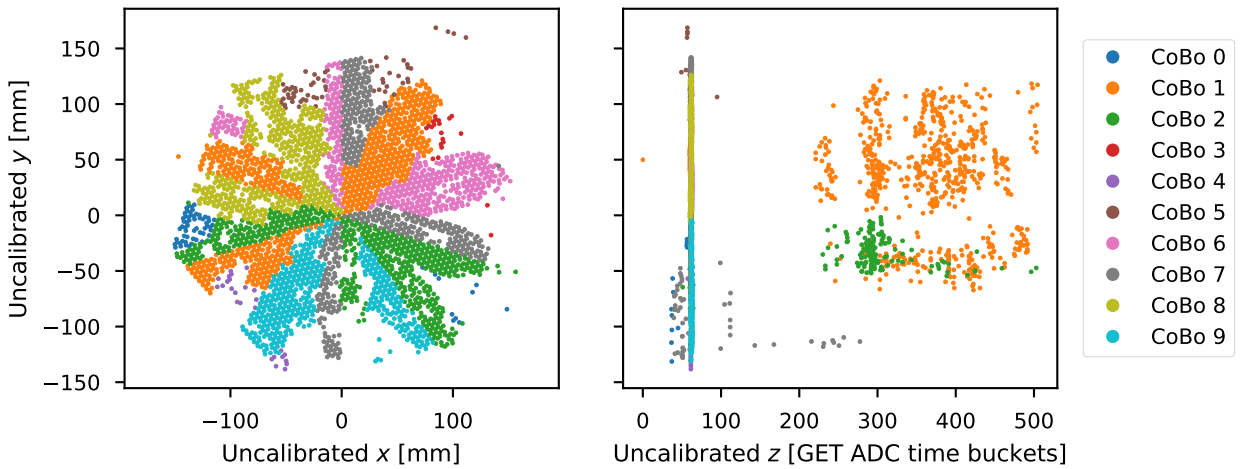


Figure 5.6: Plots of (x, y, z) positions corresponding to peak locations in a spark-like event. The majority of the channels in the inner region of the pad plane fired at approximately the same time.

The alignment of the two systems was checked and corrected by looking at spark-like events. These occurred periodically in every run, and were characterized by a large saturated pulse in the signal from the mesh (the bottom right plot in Fig. 5.5) and large, simultaneous pulses in many channels of the GET electronics (Fig. 5.6).

A small Python script was developed to analyze each spark-like event in the two DAQs and realign the event IDs when one system became misaligned with the other. Spark-like events in the VME DAQ were identified by selecting events whose mesh signal saturated the ADC (i.e., had a minimum value of 0) and had a large, negative slope in a region more than one time bucket wide. The condition on the magnitude of the slope removes pileup events from consideration, and the requirement that the region of large slope be wider than one time bucket removes events where the signal suffered a discontinuity due to a malfunction of the electronics. Any sets of sequential spark-like events were removed from consideration since it would be impossible to determine whether the event in each DAQ was due to the same spark.

Once the spark-like events were identified in the VME DAQ, the GET event with the corresponding event ID was examined to determine if it contained a spark as well. Sparks in the GET events were identified by selecting the region of time buckets where the mesh sparked and counting the number of channels that attained an extreme value in that region. Extreme values were defined as values greater than 4060 or less than 10 (for comparison, recall that the range of the 12-bit ADC is from 0 to 4095). Channels that did not vary from their baseline by more than 10 time buckets were discarded. The event was classified as a spark if more than 40 % of the remaining channels attained an extreme value. Outliers in this statistic were identified by analyzing the two spark events following the current one if misalignment was detected: if the next two sparks were aligned, the current spark was labeled as an outlier and ignored.

When the two systems were found to be out of alignment, the two GET events before and after the event where the spark was expected were analyzed to try to find the correct alignment point. If this succeeded, an event ID offset was recorded for the remaining events in the run, and the events between the last aligned spark and the current spark were marked as invalid since there is no way to determine where in that range the misalignment began. If the alignment point could not be found, an error message was printed and the run was deemed unrecoverable. The portion of each run between the last spark and the end was marked as invalid because it would be impossible to tell if these events were misaligned.

Finally, note that this complex procedure will not be required in future experiments since the Mu-

TAnT board provides a global clock signal and generates the timestamps and event IDs used across the entire system, thereby ensuring synchronization. As stated previously, though, the MuTAnT was unfortunately not yet available when the ^{46}Ar experiment was performed.

5.3.2 Merging GET data files

As mentioned in Section 2.5, the DAQ system features a distributed design that routes data from each CoBo to an independent recording computer. While this improves throughput, it also means that the experimental data for each run is spread across many separate files. The partial events from these files had to be merged before they could be analyzed. The data format written by the GET system provides two ways to merge events: by event ID and by timestamp.

The most reliable way to merge events is by timestamp since the timestamps should increment uniformly between CoBos even if not all CoBos are triggered on each event. However, merging by timestamp was not possible for this experiment since the MuTAnT board was not available, and without the MuTAnT providing a system-wide clock signal, the timestamps on each CoBo slowly diverged due to the natural variance in the circuits' internal clock frequencies.

Instead, the events were merged using the event ID. This method is generally reliable for two reasons. First, the external trigger setup always distributed a trigger signal to all CoBos regardless of which CoBos had a multiplicity trigger, so it should be impossible for any CoBo to not receive a trigger for a particular event. Second, the CoBos were configured to always output the fixed-pattern noise channels even if there were no physics channels above threshold in a given event, so each data file will always contain at least one data frame for every event even if that event did not contain any physics data for that CoBo. That being said, during the analysis it became apparent that CoBo 0 occasionally failed to trigger, causing its event IDs to fall behind those produced by the rest of the CoBos. This was corrected by comparing the intervals between successive events' timestamps in each CoBo and inserting an offset where those intervals were not approximately equal. This method works even though the CoBo clocks were not synchronized because the slight difference in clock periods between the boards is negligible on the small scale of the interval between events.

The raw output was merged into one file per experimental run in a separate step before the rest of the analysis was performed. The merging program read in partial events from the raw files produced by

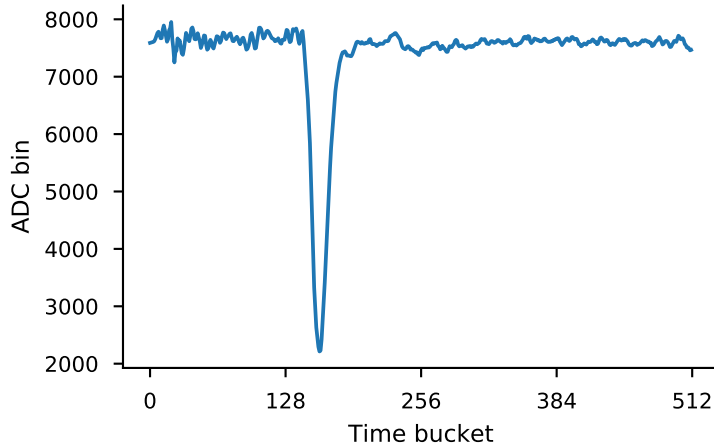


Figure 5.7: A raw ion chamber signal produced by an ^{46}Ar nucleus. The passage of the nucleus through the chamber is indicated by the large negative peak around $t = 160$. The ADC used to record this signal was 12 bits, but it also had an overflow bit that made it effectively record 13 bits per sample for a maximum digitized value of 8192.

the DAQ, grouped them by event number, and assembled full events from the fragments. The four fixed-pattern noise (FPN) channels in each AGET were then averaged together and renormalized to produce a set of AGET-level FPN signals with mean zero. These AGET-level FPN signals were then subtracted from the physics channels controlled by each AGET to correct the data for the fixed-pattern noise. The FPN data was then discarded. Finally, the data was compressed and written to an HDF5 file¹ for later analysis.

5.3.3 Beam particle identification

Although the beam of ^{46}Ar delivered by ReA3 was about 90 % pure, there were a few contaminants that needed to be removed from the data set. The main contaminants were identified as ^{46}K and ^{46}Ca (the daughter and granddaughter nuclei of ^{46}Ar) as well as one or more isotopes of nickel from the beam line. These were removed using the data from the ion chamber.

A raw signal from the ion chamber is shown in Fig. 5.7. The amplitude of the peak produced by the beam particle is proportional to the amount of charge deposited by the particle as it passed through the isobutane gas inside the chamber. This energy loss is, in turn, proportional to the square of the charge of the beam particle according to Bethe's formula. If we assume that all of the species present in the beam have the same momentum and mass, then this amplitude allows us to separate the particles.

¹HDF, or the *Hierarchical Data Format*, is a commonly-used, cross-platform format for storing large amounts of data. C, C++, Fortran, and Python libraries for reading it are available at <https://support.hdfgroup.org/HDF5/>.

All of the contaminants identified above have a larger nuclear charge Z than ^{46}Ar . Therefore, a good first step to eliminating the contaminants is to remove any event that saturates the ion chamber ADC. This was done by cutting any event where the digitized signal reaches zero. Next, events where the trigger signal was not correctly digitized were removed, and so were events that did not trigger at least one CoBo. This last criterion was found using a coincidence register recorded by the VME electronics.

After this first pass of cuts, the peaks were located in each ion chamber event and the peak heights were recorded. Events with more than one peak were flagged as pileup and discarded. The peak heights were then plotted in a histogram, shown in Fig. 5.8, and a cut was applied to keep only the large ^{46}Ar peak. This peak contained 1.015×10^6 events. Note that the runs were divided into two sets in this plot since the gain of the ion chamber was reduced between runs 216 and 217 by inserting a 0.3x attenuator before the ADC. This was done to reduce the number of events that saturated the ADC.

5.3.4 Noise removal

In the next phase of the analysis, the merged events were read in from the HDF5 files produced in the merging step. The baseline of each channel was corrected using the Fourier transform as described in Section 3.1. Next, a single peak was found in each channel by finding the maximum, and the peak location was then refined by finding its center of gravity (see Section 3.2).

After peak finding, the (x, y, z, a) data points were calibrated as discussed in Section 3.2. This particular calibration used a nominal set of parameters and was required mainly to transform the z dimension into spatial units; the data were re-calibrated later, so the specific values of these parameters were not essential during this step of the analysis.

The calibrated data were processed using the Hough transform and nearest neighbor algorithms from Section 3.3. This produced two values for each point: the minimum orthogonal distance to the nearest Hough line and the number of neighbors within a given maximum radius, which was set to 15 mm. These two figures were then written to a new HDF5 file along with the *uncalibrated* peak locations in three dimensions, the peak amplitudes, and the index of the pad that generated each point. Writing out all of the data in this step allowed us to adjust our cuts interactively later, and to experiment with making the cleaning cuts more or less restrictive as needed. In addition to this data, the center of curvature as found by the Hough transform was also recorded in the output file.

5.3.5 Beam tracks

As discussed previously in Section 3.1, the beam tracks recorded during the ^{46}Ar experiment were not usable for the analysis. This was caused in part by an unanticipated saturation effect in the preamplifier of the GET electronics channels corresponding to the pads illuminated by the beam particle track. This generated the unusually shaped signals shown in the top panel of Fig. 5.9. In addition, this saturation also caused the pole-zero correction circuit to malfunction, causing the baseline restoration to fail. This is shown in the inset in the top panel of Fig. 5.9.

Even if the electronics had worked as expected, the beam tracks would have still been difficult to use in this experiment because of the size of their projection onto the pad plane. Due to an unfortunate coincidence, the drift velocity, electric and magnetic fields, and tilt angle used in this measurement combined in such a way that the beam was projected onto a very small, almost point-like region on the pad plane. The beam therefore illuminated very few pads, so the reconstructed beam tracks had very few points, as seen in the bottom panel of Fig. 5.9. These sparse tracks are impossible to fit with a high degree of precision.

These difficulties led us to abandon fitting the beam tracks entirely. Instead, we assumed that the beam must lie along the z axis and introduced the vertex component of the objective function discussed in Section 3.4.3.

5.3.6 Track fitting

The track fitting process began by reading in the cleaned data and center of curvature produced in the previous step. A cut was applied to the data to keep only points that

- were less than 40 mm from the nearest Hough line,
- had more than two neighbors within a radius of 15 mm, and
- had a time bucket index (uncalibrated z position) less than 500.

The first two criteria were designed to exclude noise points as defined by the cleaning process. The final criterion eliminated a narrow noise pulse that occurred in several channels at the end of many events, perhaps due to switching noise in the electronics. Any event that had fewer than 50 data points remaining after these cuts was discarded to avoid wasting computer time on extremely short tracks that correspond

Parameter	Value	Units
Tilt angle	6.2	deg
Drift velocity	$-0.0604\hat{\mathbf{u}} - 0.552\hat{\mathbf{v}} - 5.14\hat{\mathbf{w}}$	cm/ μ s
Electric field	$-1026\hat{\mathbf{v}} + 9444\hat{\mathbf{w}}$	V/m
Magnetic field	$1.68\hat{\mathbf{w}}$	T
Gas pressure	19.2	torr
CoBo write clock	12.5	MHz
Shaping time	280	ns
Micromegas gain	500	(unitless)

Table 5.1: Parameter values used while analyzing the $^{46}\text{Ar}(\text{p}, \text{p}')$ data. The vectorial values are given in the beam coordinate system of Fig. 3.2.

to very forward scattering angles in the center-of-mass system where the nuclear potential scattering is minimal.

The remaining points were then calibrated and transformed into the beam coordinate system using the method described in Section 3.2 with the parameters listed in Table 5.1. Initial estimates for the track parameters were found using the method described in Section 3.4.4, and these values were used to seed the Monte Carlo fitter. The experimental hit pattern was reconstructed using the peak amplitudes and pad numbers from the calibrated data points. The optimizer was run on each track, and the results were written to a set of SQLite² databases for later analysis.

After track fitting was completed, these databases were collected into one dataset containing a total of 7.45×10^5 events. This is somewhat less than the number of ^{46}Ar events identified from the ion chamber data since some very low-multiplicity tracks were eliminated after cleaning.

Poorly fit events were filtered out using a cut on the values of the objective function components χ^2 , as shown in Fig. 5.10. After the χ^2 cuts, 2.2×10^5 events remained (approximately 30 % of the original dataset). Further cuts were applied to remove events that were fit with a backwards scattering angle in the laboratory frame (which is kinematically forbidden for elastic scattering), events that were not recorded during a production run, and events that were marked as invalid due to misalignment between the GET and VME DAQ systems (see Section 5.3.1). These cuts removed an additional 3×10^4 events, leaving a total of 1.9×10^5 good events after cuts.

An interesting feature of both χ^2 distributions is the very broad secondary peaks that occur at higher

²A single-file relational database format. This provides the benefits of database transactions (such as preventing corruption if the program is killed in the middle of a write operation) without the overhead and configuration requirements of a database server.

values of χ^2 . The events that make up these broad peaks consist partly of poorly fit tracks and noise events caused by spurious triggers, as expected, but this region also contained many events from the ^{46}Ar beam particle scattering off of the carbon nuclei that make up part of the isobutane molecule. These events were fit poorly by the optimizer since the algorithm assumed it was fitting the track from a proton with $Z/A = 1$, and not, say, a ^{12}C nucleus with $Z/A = 1/2$. This implies that the χ^2 cut can be used to filter out carbon scattering events, a conclusion that was supported by extensive spot checks of the data.

5.3.7 Proton parameter distributions

Figure 5.11 shows the distribution of proton energies as reconstructed by the Monte Carlo optimizer. The number of counts peaks at approximately 2 MeV and then diminishes rapidly at larger energies, dropping below 10 around 6 MeV. The low number of counts at higher proton energies is explained by the low trigger acceptance for these events, as shown in Figs. 4.7 to 4.11 and discussed in Section 4.2.

The distribution of reconstructed scattering angles in the center-of-mass frame is shown in Fig. 5.12. The distribution is quite narrow, showing that the angular coverage is limited to angles between approximately 30° and 70° in the center-of-mass frame or 55° and 75° in the laboratory frame. Again, this is the result of the low trigger acceptance outside this angular domain.

Figure 5.13 shows the distribution of vertex locations in the detector. The location (x_0, y_0) of the vertex was approximately normally distributed about the beam axis with a full width of approximately 10 mm at half-maximum. Figure 5.13b shows that the distribution grows wider for smaller z_0 , which suggests that this spread is caused by the emittance of the beam.

5.3.8 Vertex energy reconstructions

As discussed in Section 3.7, the ^{46}Ar vertex energy can be reconstructed for each event by two different methods. One method uses the vertex location and a calculation of the beam particle's energy loss in the gas to calculate the final energy of the beam particle at the vertex location. The other method uses the scattering angle and the energy of the outgoing proton to calculate the energy of the incoming ^{46}Ar nucleus using formulas from relativistic kinematics. These two reconstructions are compared in Fig. 5.14. It is apparent from this figure that the resolutions of the two reconstructions are vastly different: the energy is reconstructed much more precisely from the vertex position than it is from the kinematics.

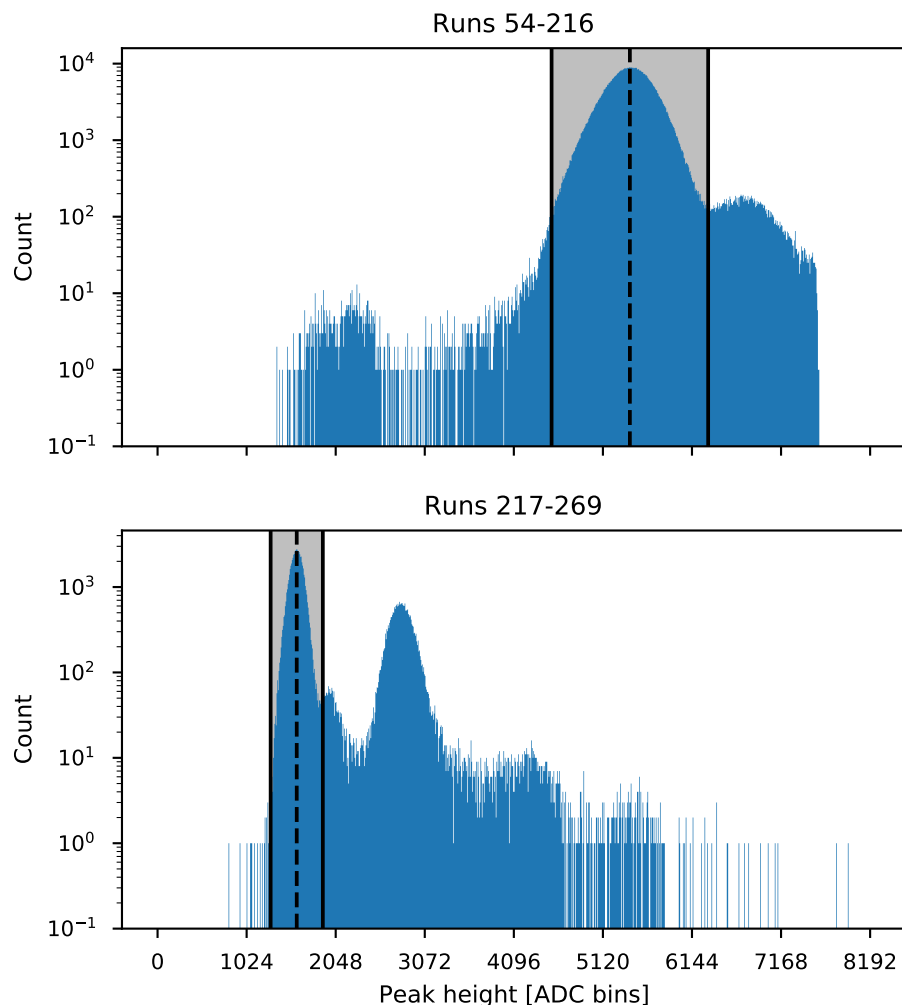


Figure 5.8: Distribution of peak heights in the ion chamber. The center of the ^{46}Ar peak is indicated by the dashed vertical line, and the boundaries of the cut applied around this peak are shown with solid lines.

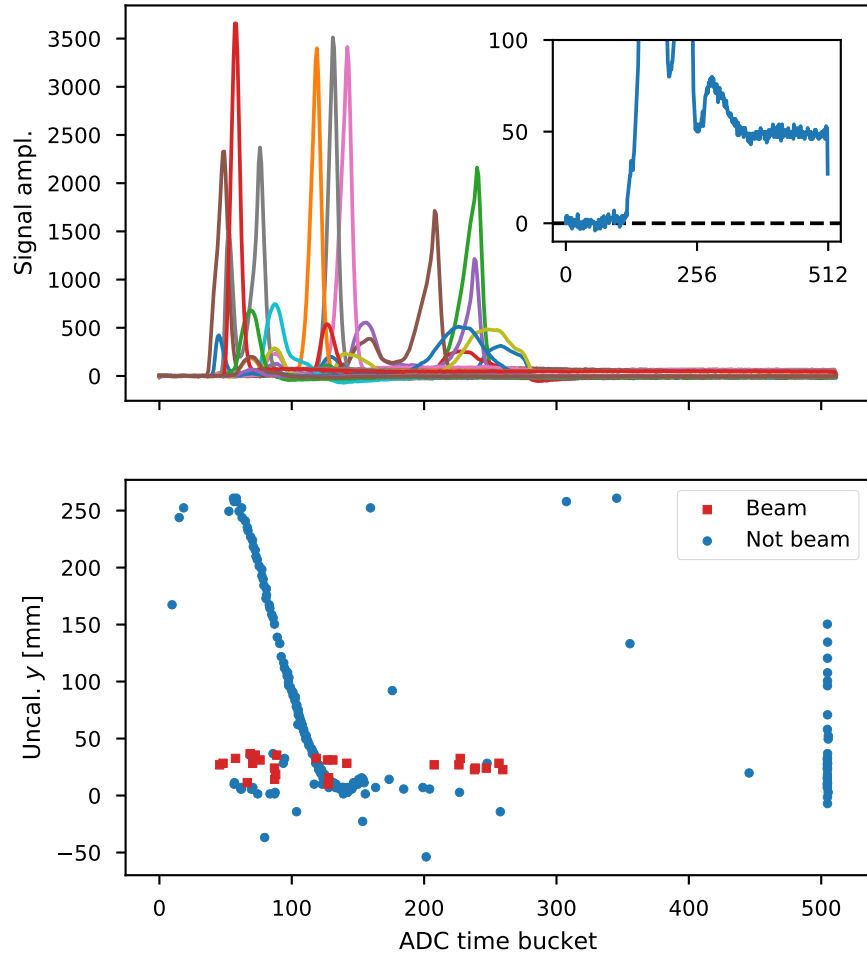


Figure 5.9: A recorded beam track from the ^{46}Ar experiment. The top panel shows the traces from the low-gain region of the sensor plane, which is where the beam track is projected onto the pads. The signals have an unusual shape which is much different from the signals generated by the proton tracks. The inset illustrates the failure of the baseline restoration for one track. In the lower panel, the red squares correspond to the reconstructed beam track, which is quite sparse.

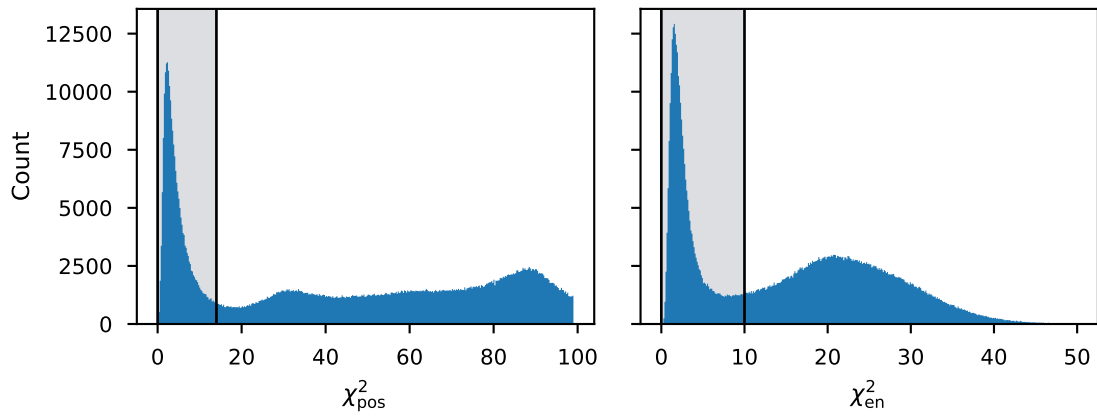


Figure 5.10: Distributions of the objective function components from fitting experimental data. The position component was cut at 14, while the energy component was cut at 10. Events with larger values for either of these components were discarded.

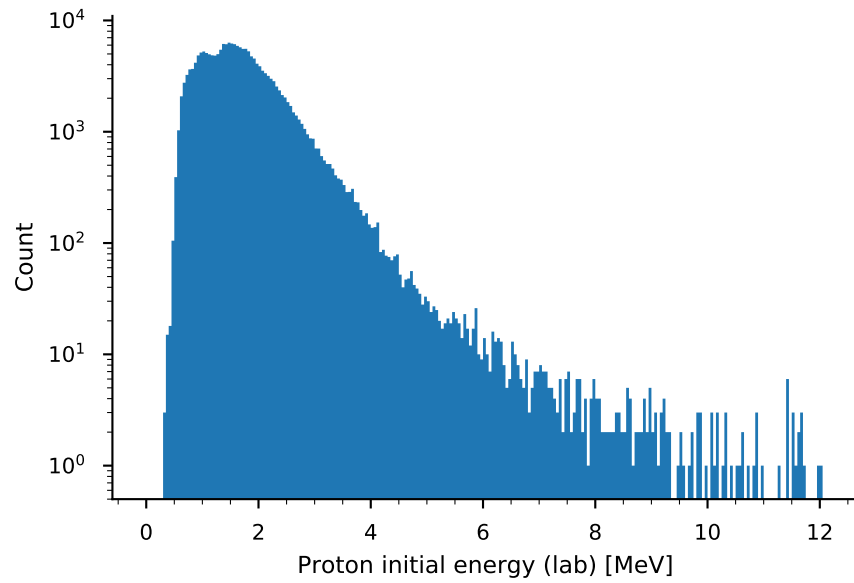


Figure 5.11: Distribution of reconstructed proton vertex energies from the experiment. Note that the vertical axis uses a logarithmic scale.

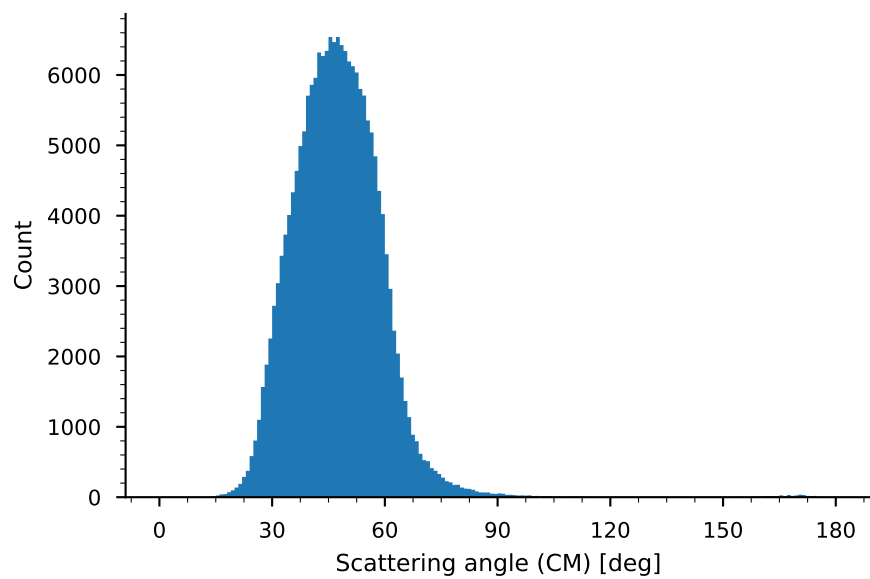
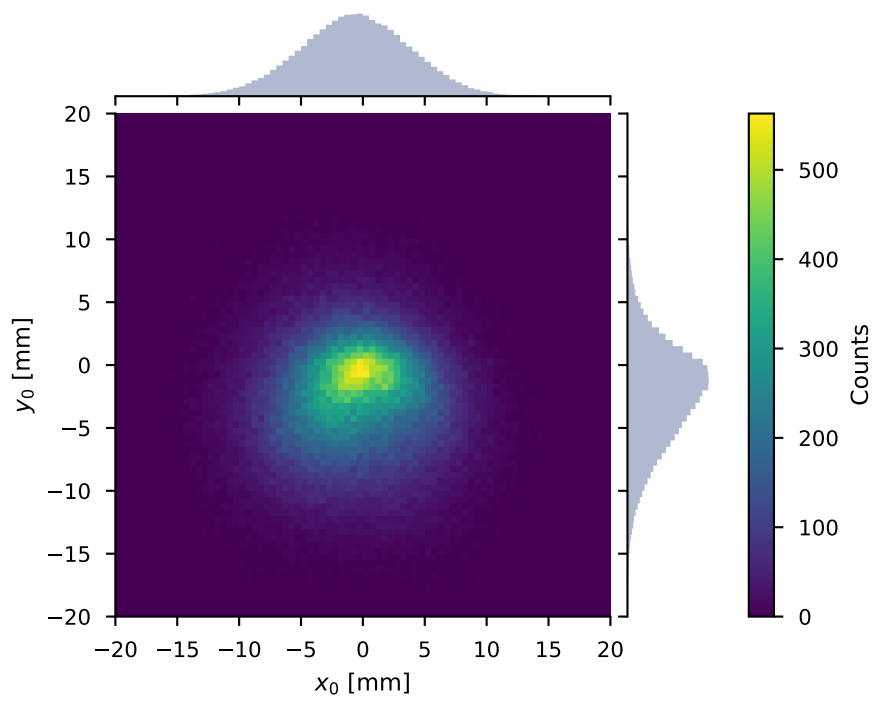
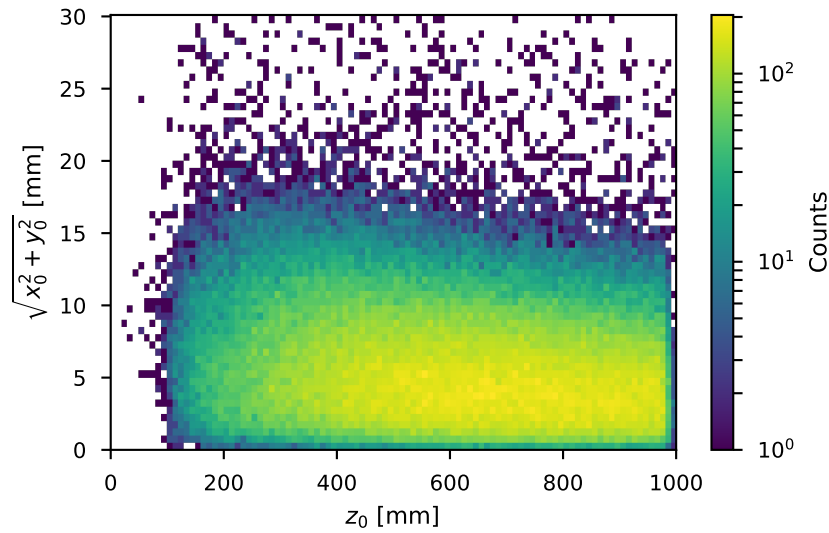


Figure 5.12: Distribution of reconstructed scattering angles in the center-of-mass frame.



(a) Distribution about beam axis



(b) Spread as a function of z

Figure 5.13: Distribution of vertex positions in the detector. Plot (a) shows the overall distribution of vertex positions in the plane transverse to the beam. Plot (b) shows that the radius of this distribution increases for smaller z , or for vertex positions further from the beam entrance window.

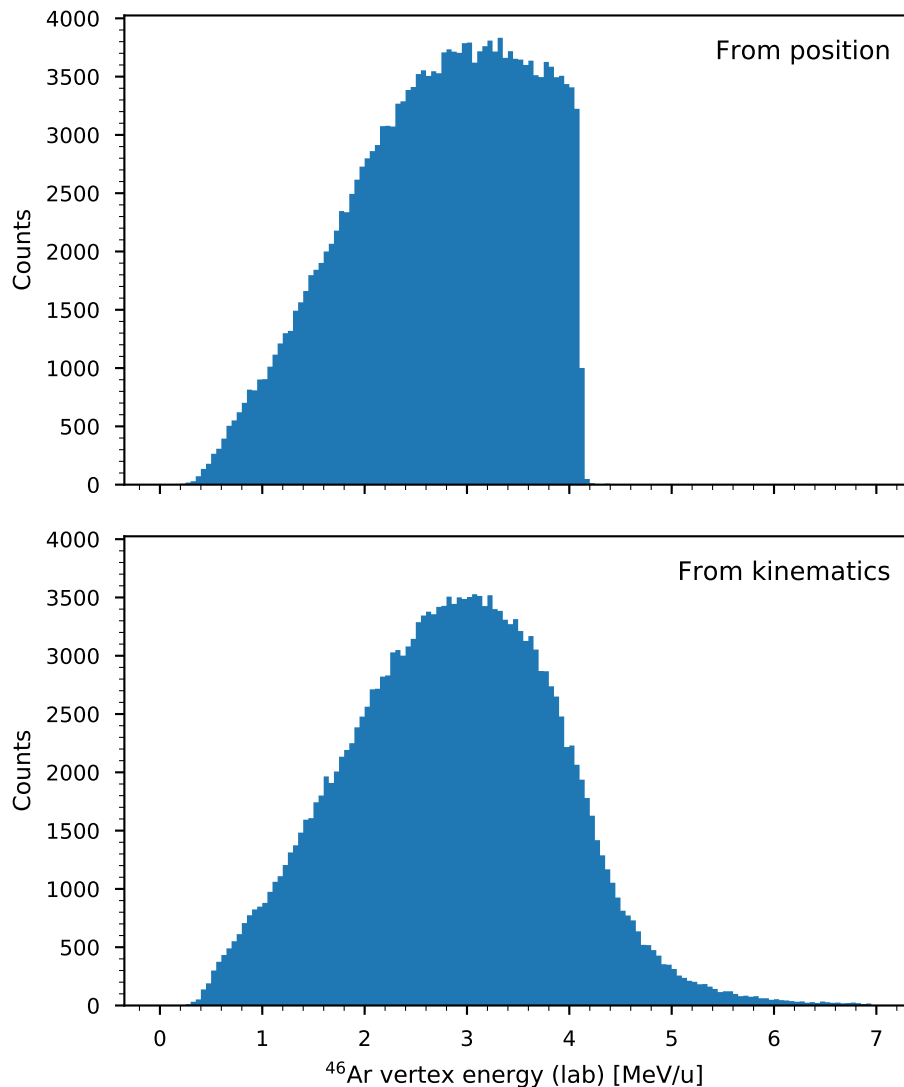


Figure 5.14: ^{46}Ar vertex energies as reconstructed from the vertex position (top) and from kinematics (bottom). The reconstruction methods are detailed in Section 3.7.

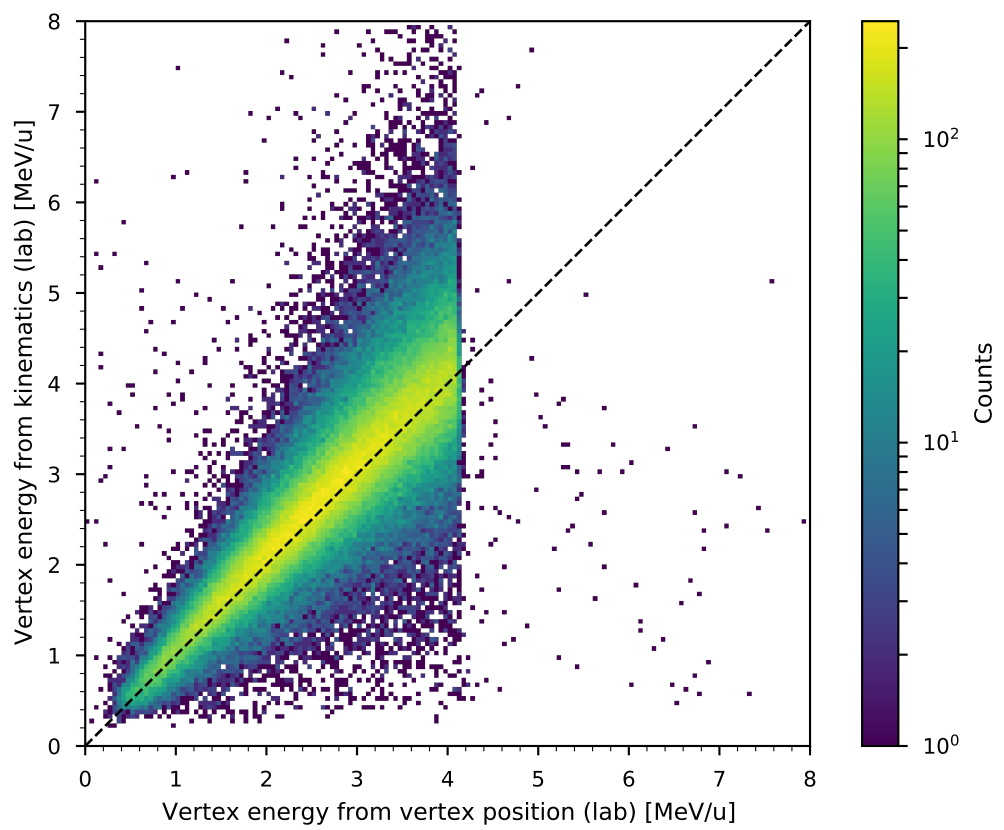


Figure 5.15: A comparison of the two vertex energy reconstructions. The line $y = x$ is plotted for reference.

While the position-based vertex energy reconstruction appears to be quite precise, its accuracy depends on the precision of several experimental parameters as well as the accuracy of the SRIM [57] calculation used to generate the stopping power of the gas. The accuracy of the energy reconstruction can be assessed by comparing the proton energy to the ^{46}Ar vertex energy. Assuming elastic scattering, kinematics calculations suggest that for proton energy E_p and vertex energy E_{Ar} ,

$$4E_{\text{Ar}} \approx \frac{E_p}{\cos^2(\theta_{\text{lab}})}. \quad (5.2)$$

These values are compared in Fig. 5.16, where the 2D histogram in the background shows values of $E_p / \cos^2(\theta_{\text{lab}})$ and the red, dashed curve shows values of $4E_{\text{Ar}}$. This plot indicates that the calibration was slightly off at low energies, so the data were recalibrated using the linear transformation

$$E'(z) = E_{\text{beam}} - \alpha(E_{\text{beam}} - E(z)), \quad (5.3)$$

where $E_{\text{beam}} = 4.17 \text{ MeV/u}$ is the incoming beam energy, and α is a scaling parameter that controls the magnitude of the recalibration. The best value of this scaling parameter was found to be 1.09, and the recalibrated energy corresponding to this parameter is shown in Fig. 5.16 in cyan. This recalibration is effectively the same as increasing the stopping power of the gas by 9 %, which indicates that the measured gas pressure may have been somewhat inaccurate.

The poor resolution of the kinematic vertex energy reconstruction is caused by the fact that the beam track was not usable in the recorded data. Because the beam track could not be fit, the emittance of the beam introduces an uncertainty of up to 1° or 2° in the scattering angle since the analysis assumes the beam lies along the z axis. Kinematics calculations show that this can introduce uncertainties on the order of 1 MeV/u in the vertex energy at higher laboratory scattering angles (see Fig. 5.17).

Figure 5.15 shows a two-dimensional histogram comparing the two vertex energy reconstructions. The distribution generally follows the line $y = x$, indicating that although the resolutions of the two reconstructions are vastly different, they tend to agree with each other on average. This suggests that the data were correctly calibrated and that the fitting method was correct.

One prominent feature of the positional vertex energy spectrum is the sharp cutoff at 4.1 MeV/u. This corresponds to the position of the beam entrance window at $z = 1 \text{ m}$ in the detector, and it is not the product of any artificial cut applied to the data. Therefore, this edge can be fit to produce an estimate of the resolution of the vertex energy reconstruction. This was done by fitting the edge with a modified

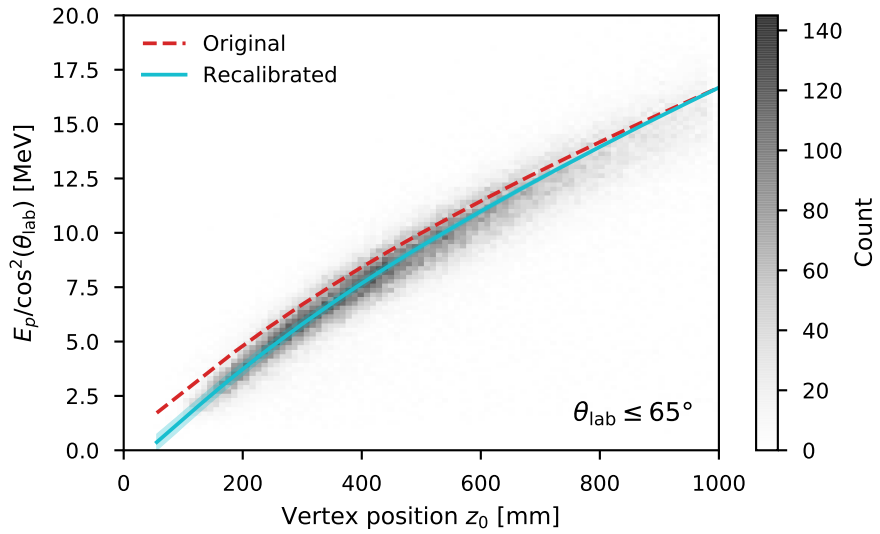


Figure 5.16: Positional vertex energy recalibration. The 2D histogram shows values of $E_p / \cos^2(\theta_{\text{lab}})$, and the two curves show values of $4E_{\text{Ar}}$. The original calibration is shown with a dashed red curve, and the corrected calibration is shown with a solid cyan curve. The error band on the corrected calibration shows the interval $1.065 \leq \alpha \leq 1.115$, where the best value is in the center at $\alpha = 1.09$. Events with $\theta_{\text{lab}} > 65^\circ$ were eliminated from this plot to reduce the spread at higher energies caused by $\cos^2(\theta_{\text{lab}})$ approaching 0.

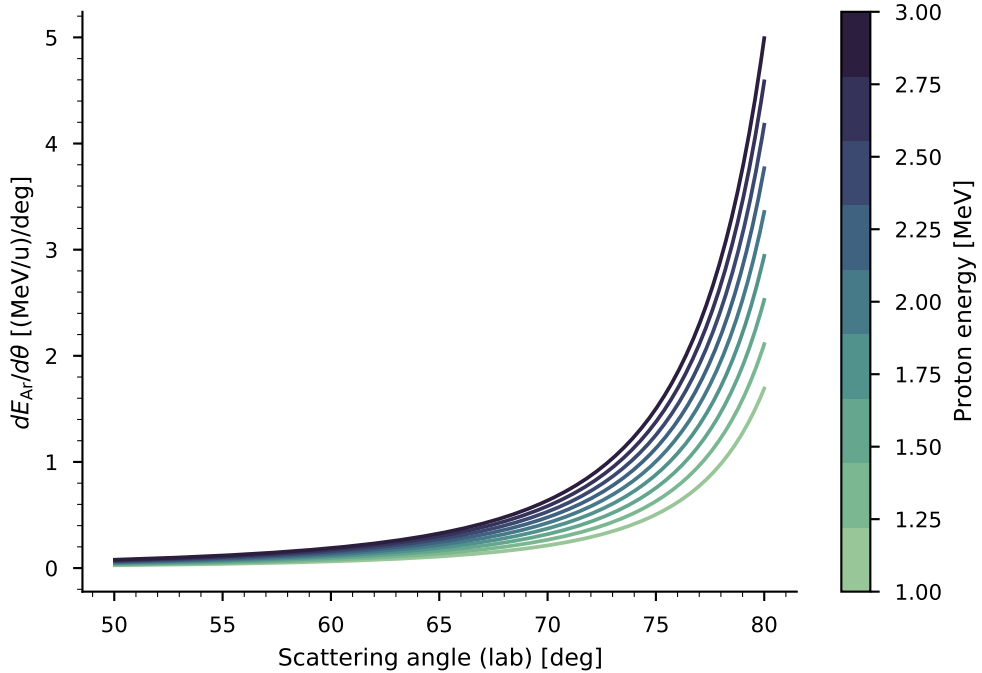


Figure 5.17: Derivatives of kinematic lines at a few proton energies. The vertex energy changes very rapidly as a function of scattering angle as the scattering angle approaches 90° in the laboratory frame.

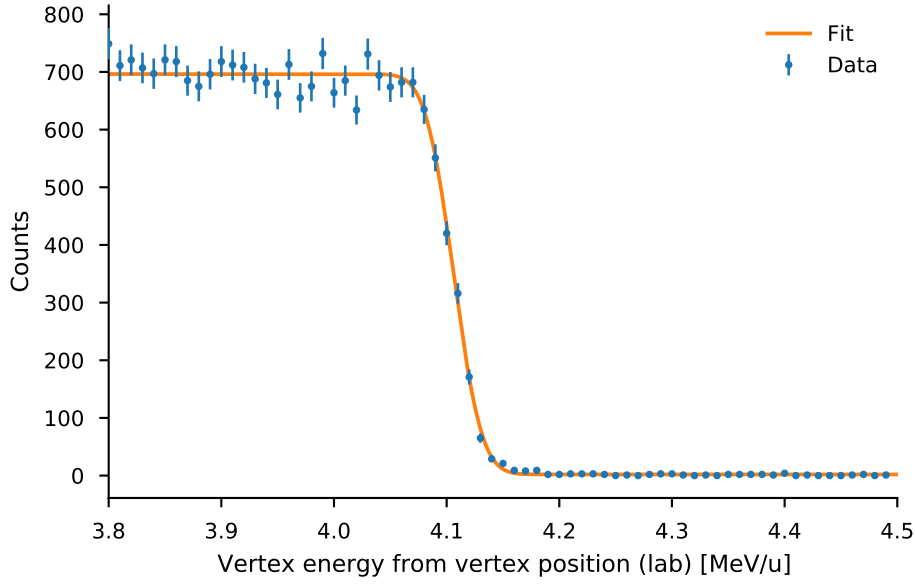


Figure 5.18: Results of a fit to the edge of the positional vertex energy distribution. The fit was performed with the function defined in Eq. (5.4), yielding parameters $\mu = 4.11 \text{ MeV/u}$, $\sigma = 19.7 \text{ keV/u}$, $A = 694$, and $b = 1.98$. The bins in the energy dimension were 10 keV/u wide, and the error bars shown are $\pm\sqrt{N}$.

Gaussian cumulative distribution function (CDF)

$$f(x; \mu, \sigma, A, b) = A(1 - \Phi(x; \mu, \sigma)) + b \quad (5.4)$$

where A corresponds to an amplitude, b is a vertical offset, μ is the mean, σ is the standard deviation, and Φ is the usual definition of the Gaussian CDF, which is given by

$$\Phi(x; \mu, \sigma) = \frac{1}{\sqrt{2\pi\sigma^2}} \int_{-\infty}^x e^{-(x'-\mu)^2/2\sigma^2} dx'. \quad (5.5)$$

The result of this fit is shown in Fig. 5.18. The width was found to be $\sigma = 19.7 \text{ keV/u}$, giving a resolution of 46.4 keV/u at FWHM.

5.3.9 Cross sections and excitation functions

After reconstructing the ${}^{46}\text{Ar}$ vertex energies, the data were binned as a function of positional vertex energy and center-of-mass scattering angle. The bins were chosen to be 50 keV/u wide in energy and 5° wide in scattering angle. The binned results are shown as a two-dimensional histogram in Fig. 5.19, and unnormalized excitation functions are shown in Fig. 5.20.

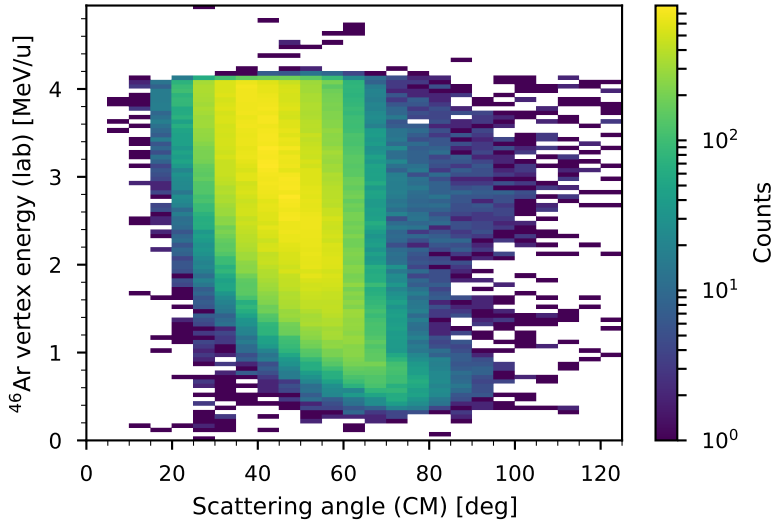


Figure 5.19: Two-dimensional histogram showing measured counts binned as a function of ^{46}Ar vertex energy in the laboratory frame and scattering angle in the center-of-mass frame.

Normalized cross sections were found from this binned data using the general formula for a cross section,

$$\frac{d\sigma}{d\Omega} = \frac{N_{\text{reac}}}{N_{\text{beam}} n_t 2\pi \sin\theta \Delta\theta}, \quad (5.6)$$

where N_{reac} is the number of scattering events that occurred, N_{beam} is the number of ^{46}Ar nuclei that entered the detector, n_t is the number of target nuclei per unit cross sectional area in the detector, θ is the scattering angle, which was taken in the center-of-mass frame, and $\Delta\theta$ is the size of the angular bins.

The number of ^{46}Ar nuclei N_{beam} that entered the detector was calculated using the ion chamber data and the scalers:

$$N_{\text{beam}} = N_{\text{IC}} f_{\text{Ar}}. \quad (5.7)$$

Here, N_{IC} is the number of particles that passed through the ion chamber, a value that was recorded in a scaler during the experiment. The correction factor f_{Ar} is the proportion of the beam particles that were ^{46}Ar and not a contaminant. This was found by dividing the number of ^{46}Ar peaks in the ion chamber data by the total number of peaks. This calculation does not account for particles that may have passed through the ion chamber without being transmitted into the AT-TPC, but measurements of the transmission made during the experiment showed that this can be neglected.

The target density n_t was found from the properties of the gas:

$$n_t = n dx = \left(\frac{\rho N_A N_t}{M} \right) \left(\frac{1}{dE/dx} \right) dE. \quad (5.8)$$

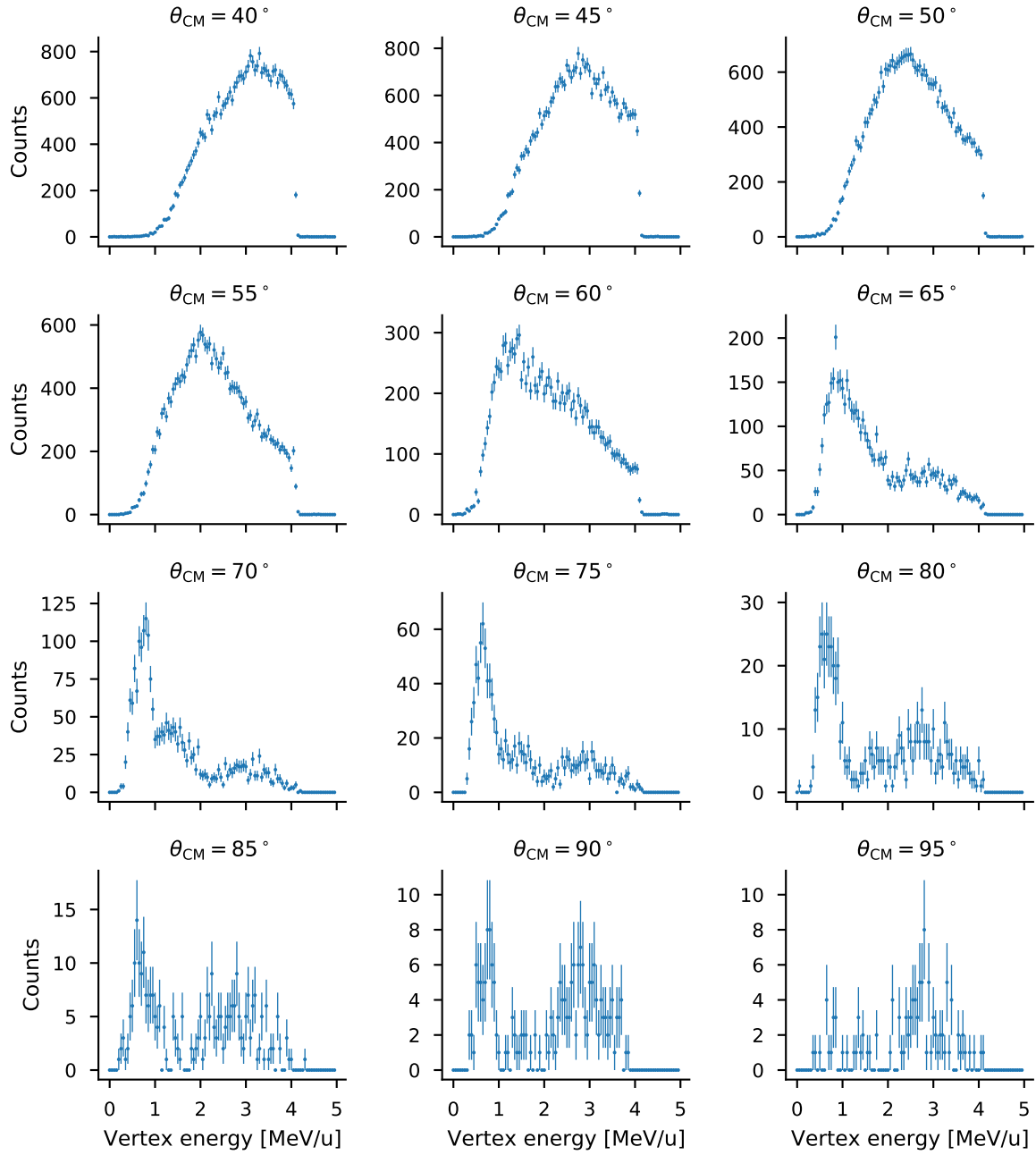


Figure 5.20: Unnormalized excitation functions as a function of ^{46}Ar vertex energy in the laboratory frame, shown at a variety of center-of-mass scattering angles. The error bars shown are $\pm\sqrt{N}$, where N is the number of counts in a given bin.

In this equation, n is the number of gas molecules per unit volume, ρ is the mass density of the gas, N_A is Avogadro's number, N_t is the number of target nuclei per gas molecule, M is the molar mass of the gas, dE/dx is the energy lost by the beam particle to the gas per unit track length, and dE is taken to be the size of the energy bins. The energy loss data was calculated using SRIM, and the remaining quantities were looked up in standard references.

The last remaining piece of Eq. (5.6) to calculate is the number of reactions N_{reac} . This quantity represents the total number of reactions that occurred in the detector, a value that is generally greater than the number that were observed due to the trigger acceptance and dead time. This was calculated by correcting the observed number of counts using estimates of the proportion of events that were not recorded:

$$N_{\text{reac}} = \frac{N_{\text{obs}}}{\epsilon_{\text{sim}} \epsilon_{\text{live}} \epsilon_{\text{pu}} \epsilon_{\text{corrupt}}}. \quad (5.9)$$

Here, ϵ_{sim} is the simulated total efficiency described in Section 4.2, which accounts for the acceptances of the trigger and the analysis process. The second factor, ϵ_{live} , accounts for the dead time of the detector, and was calculated as the ratio between the number of live triggers and the number of free triggers as recorded by scalers in the VME DAQ system. The factor ϵ_{pu} accounts for the rejection of pileup events, and was calculated by dividing the number of single-particle events in the ion chamber by the total number of valid events. Finally, $\epsilon_{\text{corrupt}}$ accounts for events that were discarded due to unrecoverable misalignment between the GET and VME DAQ systems. This was calculated as a ratio between the number of aligned events in each run and the total number of events.

To reduce the amount of uncertainty introduced by dividing the observed counts by the values of ϵ_{sim} derived from the simulation, the simulated efficiencies were fit using kernel ridge regression, a machine learning technique. Murphy [37] describes ridge regression as a modification of ordinary least squares (OLS) regression that adds to the objective function a penalty term $\lambda \|\mathbf{w}\|_2^2$ depending on a weighting parameter λ and the square of the ℓ_2 or Euclidean norm of the fit parameters \mathbf{w} . He states that this helps keep the values of the fit parameters small, reducing the likelihood of overfitting. *Kernel* ridge regression modifies this procedure further by replacing the inner products that appear in the OLS solution with calls to a kernel function $\kappa(\mathbf{x}, \mathbf{x}') \in \mathbb{R}$ that is generally nonnegative and symmetric in its arguments, and can be interpreted as a measure of the similarity between feature vectors (measurements of the independent variable) \mathbf{x} and \mathbf{x}' [37]. The kernel function used in this fit was the radial basis function (RBF)

$$\kappa(\mathbf{x}, \mathbf{x}') = e^{-\gamma \|\mathbf{x} - \mathbf{x}'\|^2}. \quad (5.10)$$

If the parameter γ is chosen to be σ^{-2} , this function corresponds to a Gaussian distribution [43]. The fit itself was performed using a Python implementation of kernel ridge regression from the scikit-learn package [43].

Figure 5.21 shows the result of applying this fitting procedure to the simulated efficiencies from the third parameter set defined in Table 4.3. The fit curve, shown in orange, smooths out the small-scale statistical fluctuations in the efficiencies while maintaining the large-scale shape of the data. This smoothing is justified on the assumption that the efficiencies of the trigger and analysis should vary relatively slowly as functions of energy. Therefore, using a fitted version of the data reduces the statistical noise in the result without requiring an impractically large number of simulated tracks.

Figure 5.22 shows the cross sections calculated for the experimental data using Eq. (5.6). The measured cross sections are approximately of the same order of magnitude as the R matrix simulation result, although the curvature of the data points is somewhat different from that of the simulation. This suggests that the simulation of the acceptance might be inaccurate, although this is difficult to prove due to the low number of counts in each bin, especially at higher θ_{CM} .

5.3.10 Alternative analysis method

The accuracy of the cross sections presented in Section 5.3.9 depends heavily on the calculated efficiency. This efficiency is found using a Monte Carlo simulation, so its value is subject to random fluctuations. In addition, simplifying assumptions made in the simulation may introduce inaccuracies in the output. Therefore, it is worthwhile to consider an alternative method of comparing the data to the R matrix simulation.

In theory, the excitation function of a resonant scattering reaction should consist of isolated Breit–Wigner resonances superimposed on a smoothly varying background described by the optical model [22, pg. 597]. Thus, we should expect to see any resonances in the data as deviations from a smooth baseline given by the optical model excitation function folded with the efficiency. If this baseline is removed, then the resonances should be the only remaining features. This argument can also be applied to the results of the R matrix calculation, yielding a theoretical curve that can be compared to the experimental data.

Since the analytical form of the baseline for the experimental data is unknown, it was modeled using a quadratic function. Ordinary least squares regression was used to fit this function to the total recorded

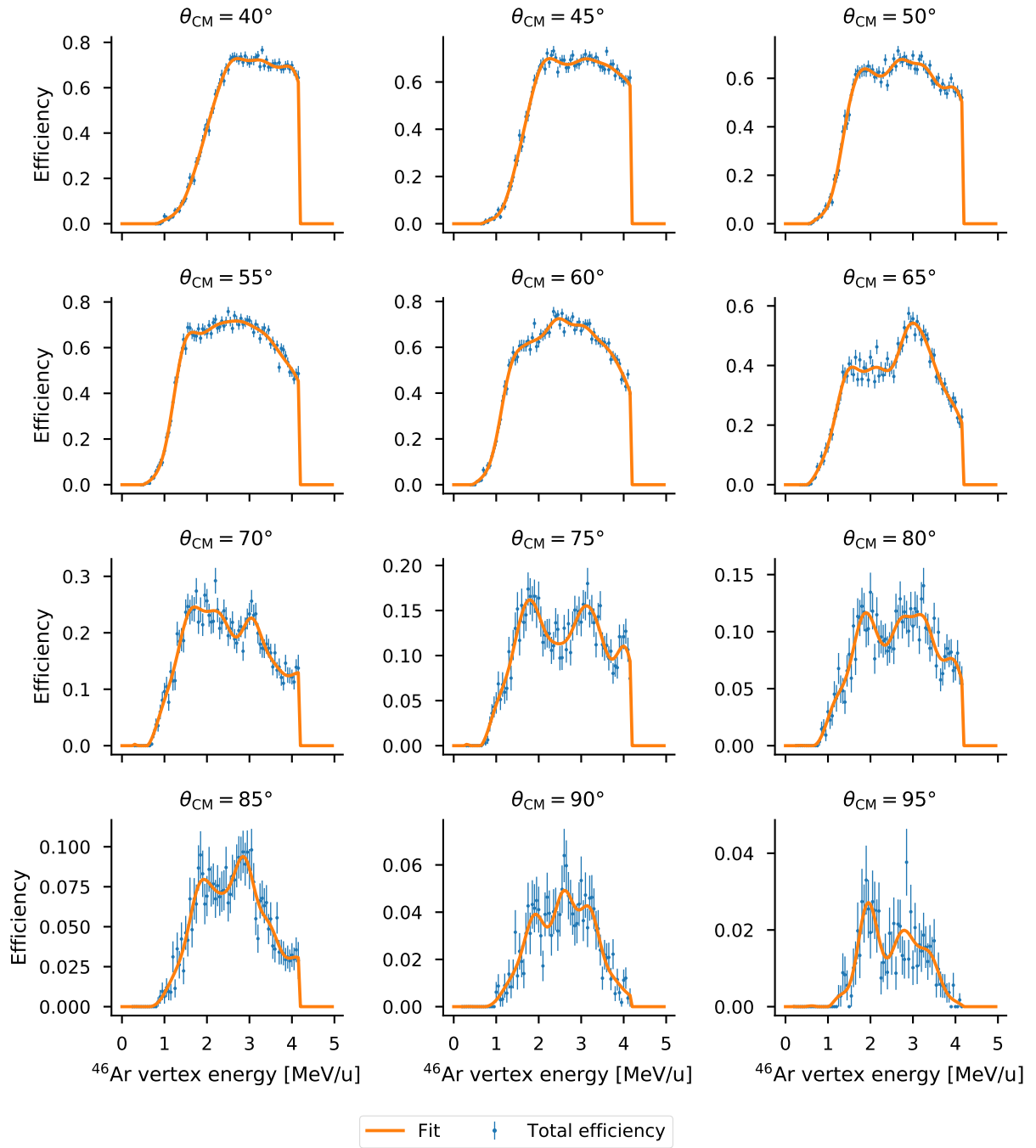


Figure 5.21: Simulated total efficiencies for parameter set 3 (as defined in Table 4.3) with kernel ridge regression fit. Similar fits were performed for the efficiencies generated for the other parameter sets.

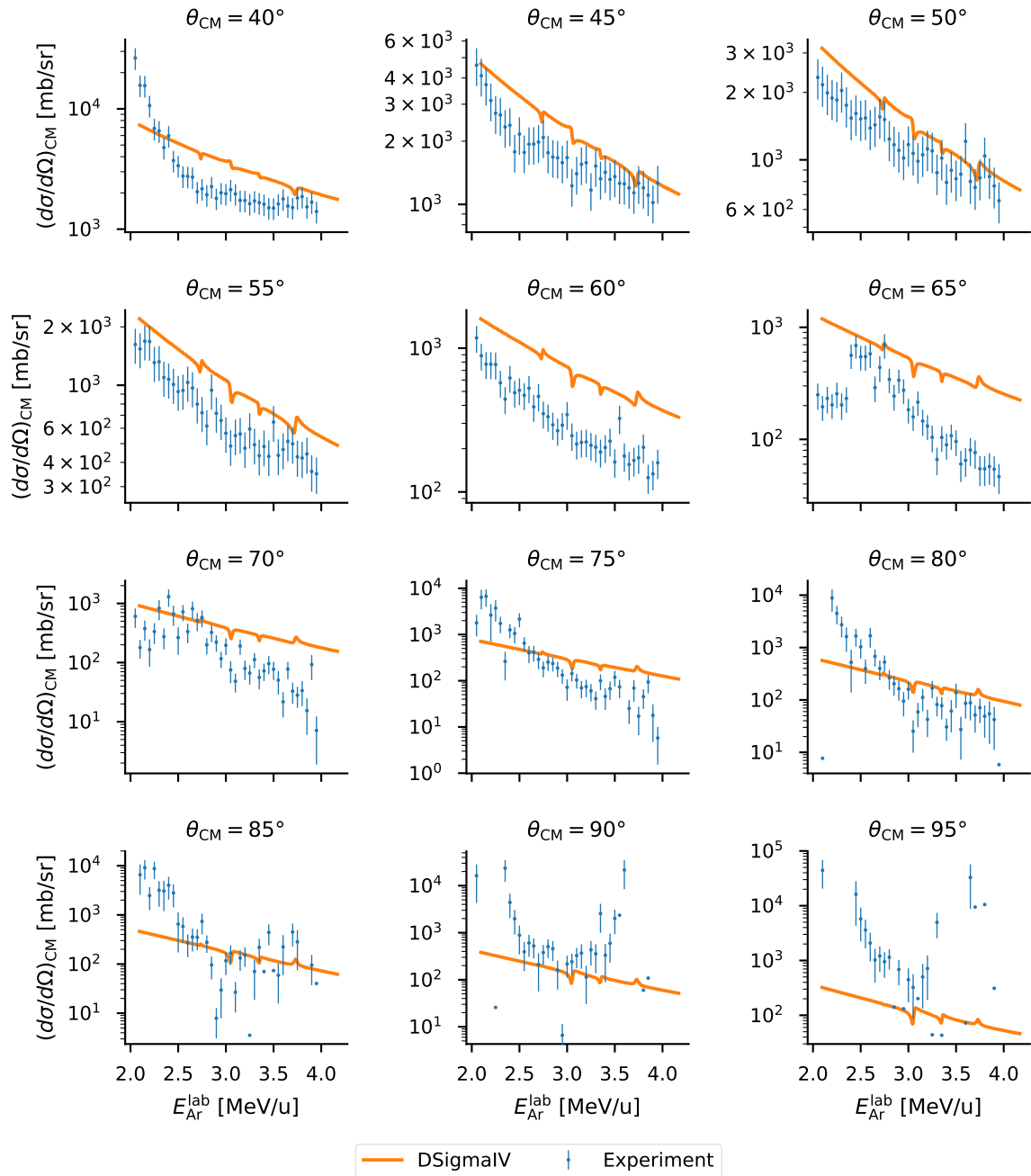


Figure 5.22: Excitation functions in the region of interest for $^{46}\text{Ar}(p,p')$ calculated from experimental results. The results of an R matrix calculation performed with DSIGMAIV is also shown for comparison. The parameters used in this calculation are given in Section 5.3.10.

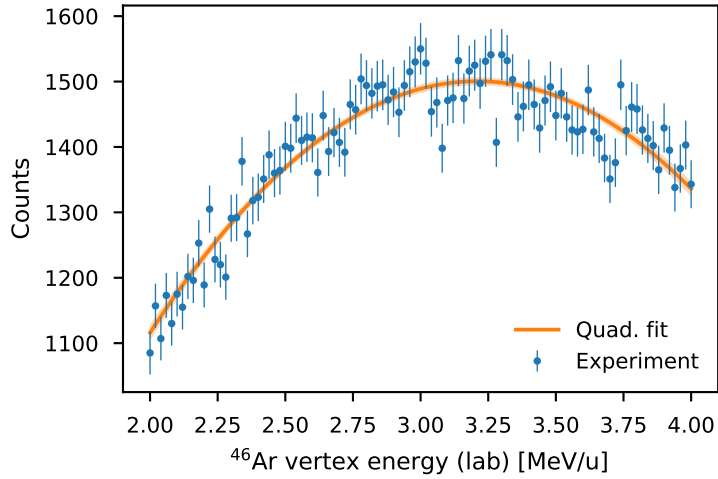


Figure 5.23: Experimental counts summed over all scattering angles and fit with a quadratic function. The fit function was $y(x) = -263(12)x^2 + 1687(74)x - 1207(108)$, where the numbers in parentheses are the standard errors of the fit coefficients. A 1 σ error band is shown around the fit using shading.

counts integrated over all scattering angles with 20 keV/u bins in the energy dimension. The result of the fit is shown in Fig. 5.23. Integrating over all angles greatly increases the number of counts in each bin, and it should not greatly affect the shape of the resonances since we are effectively only integrating between approximately 30° and 60° due to the severe limitations on our acceptance. Nonetheless, any effect that the integration has on the results will be compensated for below.

A similar procedure was applied to the R matrix calculation results from DSIGMAIV. Let $R_{E\theta}$ represent the calculated cross section in the bin defined by energy E and scattering angle θ . Then, a weighted total excitation function was defined as

$$\tilde{R}_E = \sum_{\theta} \frac{R_{E\theta} N_{\theta}}{\max_E(R_{E\theta})}, \quad (5.11)$$

where $\max_E(R_{E\theta})$ denotes the maximum value of the cross section in each angular slice, and N_{θ} is a normalization factor calculated from the experimental data. If the experimental bins are denoted $D_{E\theta}$, then these normalization factors are given by

$$N_{\theta} = \frac{\sum_E D_{E\theta}}{\sum_{E\theta} D_{E\theta}}. \quad (5.12)$$

This renormalizes the amplitude of the excitation function for each scattering angle to be proportional to the number of counts observed in that angular bin in the experiment. Therefore, when the calculated excitation functions are summed, the proportion contributed by each angular bin will be the same for

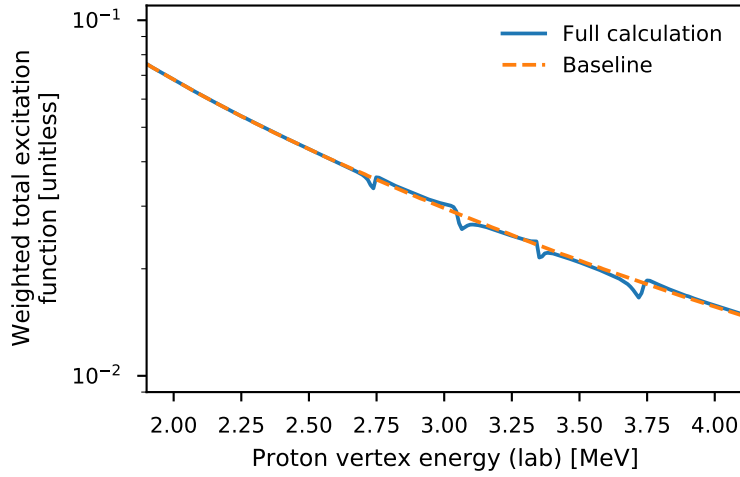


Figure 5.24: Weighted total excitation function defined in Eq. (5.11) calculated for both the full R matrix simulation (labeled “Full calculation”) and a calculation with no resonances (labeled “Baseline”).

the experiment and the calculation. One downside to this approach is that the resulting total excitation function is unitless and its scale is arbitrary, but this will be addressed below.

Instead of fitting the R matrix calculation to remove the baseline, a second calculation was performed using the same input file, but with all resonances removed. This produced the curve labeled “baseline” in Fig. 5.24. This calculated baseline serves the same purpose as the baseline function that was fit to the data above.

To put the data and the R matrix calculation on the same scale, a relative difference was calculated between each quantity and its respective baseline. The relative difference was defined as

$$\Delta(D, B) = \frac{D - B}{B} \quad (5.13)$$

for data point D and baseline point B . This scales the two datasets to be of the same magnitude, and it removes the baseline from each. The R matrix calculation curve was then convolved with a Gaussian of standard deviation 19.7 keV to account for the resolution of the AT-TPC and provide a fair comparison. The width of this Gaussian corresponds to the resolution of the positional vertex energy reconstruction found in Section 3.7. The convolution greatly reduces the resonance amplitudes, especially in the case of the narrow $3/2^-$ resonance corresponding to the ground state of ^{47}Ar . This is shown in Fig. 5.25.

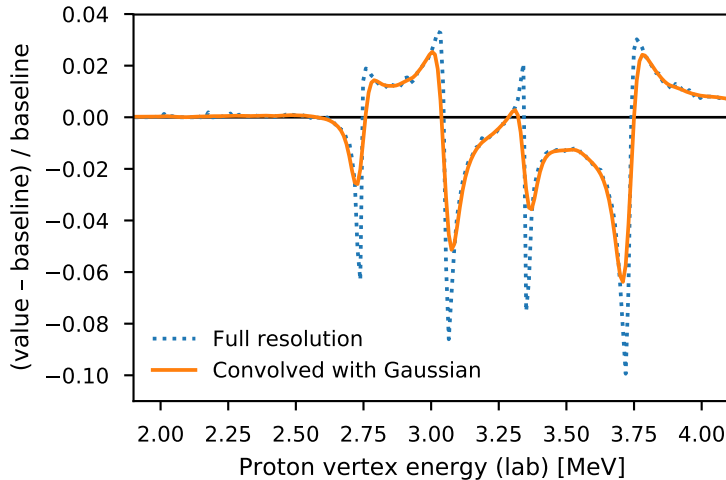


Figure 5.25: Effect of convolving the R matrix calculation with a Gaussian. The resonances in the convolved version are wider and have significantly smaller amplitudes.

5.3.11 Results

Figure 5.26 shows the final comparison between the R matrix calculation and the data. Four resonances are shown in the result, and the properties of these resonances are given in Table 5.2. The R matrix calculation shown in the figure was performed with the Koning and Delaroche [29] global optical potential parameters given in Table 4.2 on Page 62.

Each resonance was calculated with a resonance mixing phase of 20° to account for the fact that the observed cross section is averaged over several fine structure states [47]. The value of this phase was chosen to be compatible with calculations done by Harney [20] and with the results of Scott et al. [47] with ^{40}Ar .

For each resonance, the total resonance width Γ can be written as

$$\Gamma = \Gamma_p + \Gamma_\downarrow, \quad (5.14)$$

where Γ_p is the proton single-particle width and Γ_\downarrow is the spreading width caused by splitting over fine structure states. The value of Γ_\downarrow was taken to be 10(10) keV based on the values compiled by Reiter and Harney [45] for proton scattering reactions on nuclei of a similar mass to ^{47}Ar . The relative uncertainty of the values of Γ_p produced by DSIGMAIV was estimated to be 10 %.

As discussed in Section 1.1.8, the resonance energy $E_{\text{res}}^{\text{CM}}$ is related to the energy E_x of the excited state

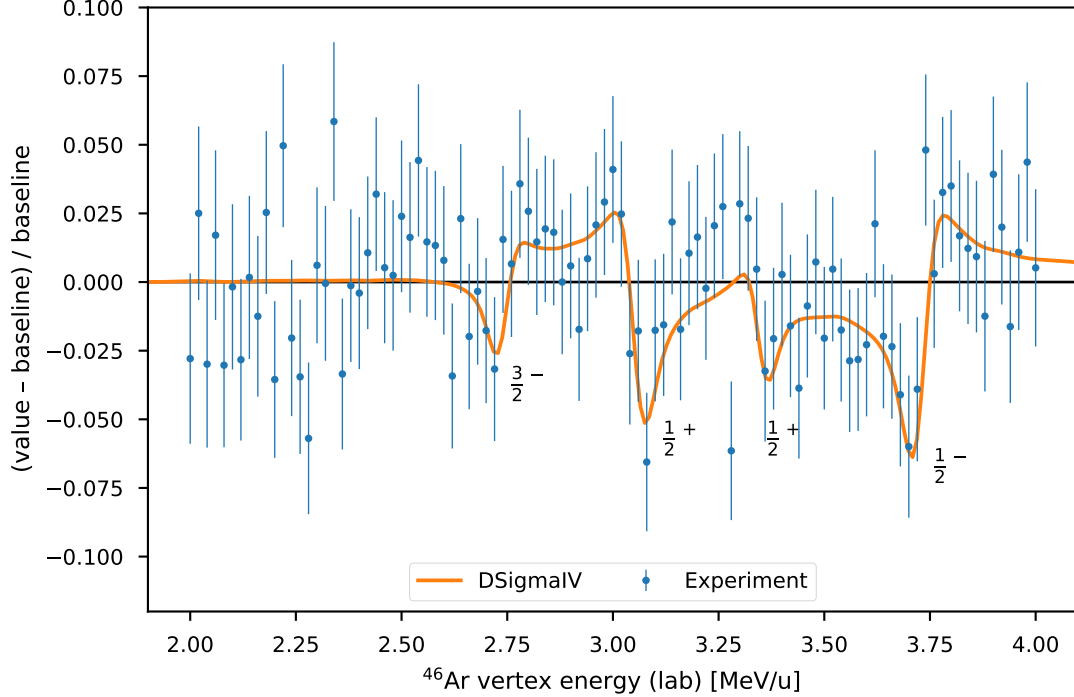


Figure 5.26: Comparison of data to R matrix calculation.

$E_{\text{res}}^{\text{CM}}$	$E_{\text{Ar}}^{\text{CM}}$	E_x	J^π	S	Γ	Γ_p	Γ_\downarrow
2680(20)	$-127^{+39}_{-36} \pm 20$	$0^{+25}_{-20} \pm 28$	$3/2^-$	$0.27 \pm 0.03^{+0.21}_{-0.13}$	15(10)	4.3(4)	10(10)
2990(20)	$183^{+36}_{-50} \pm 20$	$310^{+20}_{-40} \pm 28$	$1/2^+$	$0.30 \pm 0.07^{+0.14}_{-0.08}$	30(10)	20(2)	10(10)
3280(20)	$473 \pm 36 \pm 20$	$600 \pm 20 \pm 28$	$1/2^+$	$0.09 \pm 0.02^{+0.05}_{-0.07}$	18(10)	8.0(8)	10(10)
3650(20)	$843^{+32}_{-58} \pm 20$	$970^{+10}_{-50} \pm 28$	$1/2^-$	$0.42 \pm 0.05 \pm 0.09$	34(10)	24(2)	10(10)

Table 5.2: Properties of the resonances shown in Fig. 5.26. Energies and widths are given in keV/u. $E_{\text{Ar}}^{\text{CM}}$ is the energy of the corresponding level in the analogue nucleus calculated assuming $\Delta E_C - S_n = 2807(30)$ keV, from the literature values of those parameters; E_x is the excitation energy calculated from the resonance assuming $\Delta E_C - S_n = 2680(20)$ keV, the energy of the ground state resonance; S refers to the spectroscopic factor; Γ is the total resonance width; Γ_p is the proton single-particle width; and Γ_\downarrow is the spreading width arising from mixing with the $T_<$ states. For quantities with two uncertainties, the first value is the systematic uncertainty and the second is statistical.

in the analogue nucleus through the relation

$$E_x = E_{\text{res}}^{\text{CM}} - (\Delta E_C - S_n), \quad (5.15)$$

where ΔE_C is the Coulomb shift of the state and S_n is the neutron separation energy of the analogue nucleus. The energies $E_{\text{Ar}}^{\text{CM}}$ in Table 5.2 were calculated using a Coulomb shift of 6.47139 MeV from a recent theoretical calculation by Wang et al. [55]. To account for the fact that the Coulomb shift can vary slightly between levels, it was assigned a systematic uncertainty of 30 keV, which was the standard deviation of the differences between the observed and theoretical excitation energies found in ^{40}Ar [47, Table 1]. The value of the neutron separation energy was 3.664 73(158) MeV, which was found using the NNDC Q-value calculator³, which is based on a recent set of mass measurements collected by Wang et al. [54]. In addition to the uncertainties arising from these values, a systematic uncertainty in the energy recalibration (see Section 5.3.8) was added for each level. These uncertainties were [-20 keV, +25 keV] for the ground state resonance, [-40 keV, +20 keV] for the first $1/2^+$ resonance, [-20 keV, +20 keV] for the second $1/2^+$ resonance, and [-50 keV, +10 keV] for the $3/2^-$ resonance. These values were found by varying the recalibration scaling parameter up and down by 2.5 %, a limit which corresponds to the error band shown in Fig. 5.16.

Alternatively, the excitation energy can be found by assuming that the ground state resonance must correspond to zero excitation energy in the analogue nucleus. This produces the excitation energies listed as E_x in Table 5.2.

During the analysis, we noticed that the spectroscopic factors in the DSIGMAIV output were systematically much lower than the values found in the (d, p) measurement. This can be explained by the differences in the way the R matrix theory generates a single-particle width. As discussed in Section 1.1.6, the R matrix model depends on a somewhat arbitrary boundary called the channel radius to set the scale of the nuclear potential. Models of transfer reactions, on the other hand, do not include this division of space, and the nuclear shape there depends only on the optical model parameters used. This produces more realistic single-particle widths, and therefore more realistic spectroscopic factors. Thus, we renormalized the spectroscopic factors generated by DSIGMAIV to make them compatible with the values from the optical model. These renormalization factors were found from an analysis of the ^{40}Ar case⁴, and they are given in Table 5.3. The spectroscopic factors listed in Table 5.2 are the renormalized values.

³<https://www.nndc.bnl.gov/qcalc/index.jsp>

⁴Analysis performed by Lisa Carpenter at the NSCL.

J^π	Renormalization factor
$3/2^-$	1.34(6)
$1/2^+$	1.22(24)
$1/2^-$	1.33(9)

Table 5.3: Renormalization factors applied to spectroscopic factors from DSIGMAIV.

J^π	Slope [keV $^{-1}$]	$I(\Gamma_\downarrow = 10 \text{ keV})$	Rel. uncertainty [%]
$3/2^-$	1.6×10^{-5}	-1.55×10^{-3}	10
$1/2^+$	2.2×10^{-5}	-4.51×10^{-3}	4.9
$1/2^+$	-7.7×10^{-7}	-4.28×10^{-3}	0.18
$1/2^-$	1.3×10^{-5}	-6.86×10^{-3}	1.9

Table 5.4: Calculated values of the resonance integral from Eq. (5.17) and the relative uncertainty $\delta I/I$ it contributes to the spectroscopic factor for a variation of 10 keV in Γ_\downarrow .

The systematic uncertainty in the spectroscopic factors can be related to variations in the integral of each resonance with respect to energy. If we assume a Breit–Wigner resonance shape, then the cross section has the general form

$$\frac{d\sigma}{d\Omega} \propto \frac{\Gamma_p}{(E - E_{\text{res}})^2 + \Gamma^2/4}. \quad (5.16)$$

The integral of this is

$$I \equiv \int_{-\infty}^{\infty} \frac{\Gamma_p}{(E - E_{\text{res}})^2 + \Gamma^2/4} dE = \frac{2\pi\Gamma_p}{\Gamma}, \quad (5.17)$$

which is inversely proportional to the spectroscopic factor since [22]

$$S \propto \frac{\Gamma}{\Gamma_p}. \quad (5.18)$$

Thus, by measuring the change in I when varying Γ_p and Γ_\downarrow , we recover information about the uncertainty in S . This was applied by varying Γ_\downarrow from 0 keV to 50 keV in 5 keV steps and calculating the integral of the negative part of the resonance⁵ at each step. The results of this are summarized in Table 5.4. The dependence on Γ_\downarrow was found to be small, so this effect was neglected in the final error analysis.

Finally, a Monte Carlo simulation was performed with TRIM [57] to assess the effects of energy straggling, or random fluctuations in the energy lost to the gas, on the energy resolution. The simulation was performed using isobutane gas with density $6.108 \times 10^{-5} \text{ g/cm}^3$ (19.2 torr at room temperature). The thickness of the gas target was varied between 10 cm and 70 cm in 10 cm steps, which corresponded to

⁵The positive part depends more strongly on the resonance mixing angle, so it was excluded.

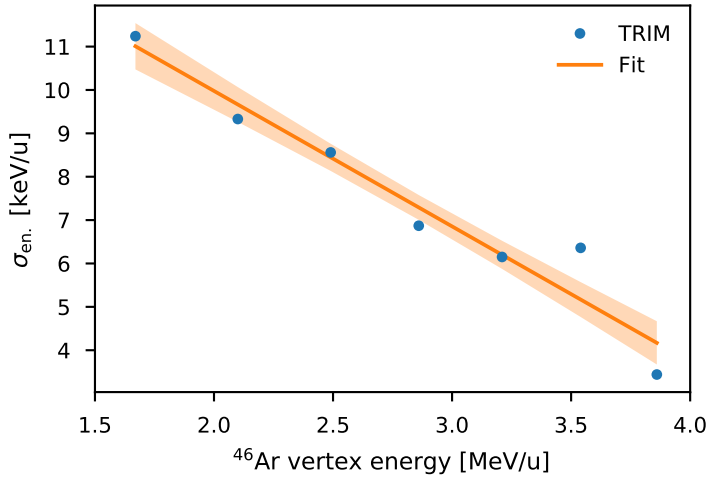


Figure 5.27: Results of energy straggling calculation with TRIM [57]. The orange line is a linear fit to the data with slope $-3.12(35)$ keV/MeV and intercept $16.2(10)$ keV. The shaded orange band is a 1σ error band.

Energy (lab) [keV/u]	Straggling (lab) [keV/u]
2738	7.67
3055	6.68
3351	5.16
3729	4.58

Table 5.5: Straggling at the resonance locations.

vertex energies between 1.67 MeV/u and 3.86 MeV/u, thereby covering the range of interest. The vertex energies were calculated by taking the mean of the outgoing ^{46}Ar ion energies, and the straggling was taken to be the standard deviation of these energies. The results are shown in Fig. 5.27 with a linear fit, and the straggling values predicted at the four resonance energies are shown in Table 5.5. The largest predicted straggling was 7.67 keV/u, which is much smaller than the energy resolution or the energy bin size, so the straggling was negligible.

5.3.12 Statistical testing

An F -test was performed to establish the statistical significance of these resonances. This test was constructed to compare two models to the data: the R matrix model and the horizontal line $y = 0$, which will be referred to as the null model. The F -test asks whether the null hypothesis—that both models fit the data equally well—can be rejected in favor of the alternative hypothesis—that the R matrix model fits

J^π	Energy range [MeV/u]	F	p
$3/2^-$	(2.55, 2.86)	0.80	0.59
$1/2^+$	(2.86, 3.25)	1.46	0.27
$1/2^+$	(3.20, 3.55)	0.27	0.94
$1/2^-$	(3.4, 4.0)	2.36	0.07
—	(2.5, 4)	6.15	<0.01

Table 5.6: Statistical significance of the proposed resonances. The first three lines show the results of the F -test applied to the three individual resonances. The last line shows the result of the test applied to the data as a whole.

the data significantly better than the null model. This was done by computing the F statistic given by

$$F = \frac{(\text{RSS}_0 - \text{RSS}_R)/(\nu_0 - \nu_R)}{\text{RSS}_R/\nu_R}. \quad (5.19)$$

Here, the subscript R refers to the R matrix model, and the subscript 0 refers to the null model. ν is the number of degrees of freedom in each model, which was taken to be $N - 6$ for the R matrix model and N for the null model, with N being the number of data points. Finally, RSS is the residual sum of squares

$$\text{RSS} = \sum_i [y_i - \hat{y}(x_i)]^2 \quad (5.20)$$

for data points (x_i, y_i) and model prediction $\hat{y}(x)$. This statistic was compared to the F distribution, which has a cumulative distribution function given by

$$F(x; \nu_1, \nu_2) = I_{\frac{\nu_1 x}{\nu_1 x + \nu_2}} \left(\frac{\nu_1}{2}, \frac{\nu_2}{2} \right) \quad (5.21)$$

where I represents the regularized incomplete beta function. The null hypothesis was rejected if the p -value

$$p = 1 - F(F; \nu_0 - \nu_R, \nu_R) \quad (5.22)$$

was less than 0.10. This would imply that the R matrix model described the data significantly better than a horizontal line, which would suggest that the resonance is statistically significant. Values of F and p for each resonance are given in Table 5.6.

5.4 Discussion

5.4.1 Comparison to previous measurements

Table 5.7 and Fig. 5.28 compare the excitation energies E_x and spectroscopic factors S found in this work to literature values. In addition to the experimental values, three shell model calculations are included

in this table and figure. First is a calculation using the SDPF [41] interaction performed by Gaudefroy et al. [18]. The SDPF interaction models the nucleus using a valence space consisting of the *sd* shell levels for the protons and the *pf* shell levels for the neutrons [41]. This model is the oldest of the three, but it provides the best agreement with our value of the energy of the $1/2^-$ state. In addition to the SDPF calculation, two calculations by Gade et al. [15] are included using the newer SDPF-U [40] and SDPF-MU [52] interactions. According to Gade et al. [15], the SDPF-U interaction uses the same valence space as the SDPF interaction, but it is tuned using experimental and theoretical data from neutron-rich silicon isotopes to produce more-reliable results for these species. The SDPF-MU interaction improves this further by adding cross-shell tensor force interactions between the protons in the *sd* shell and the neutrons in the *pf* shell, which helps the interaction to better reproduce $B(E2; 0^+ \rightarrow 2^+)$ values and $E(2_1^+)$ and $E(4_1^+)$ energies in silicon and sulfur isotopes near $N = 28$ [15]. These models agree quite well with the experimental results of Gaudefroy et al. [16], but this is to be expected since the models were developed using those results as input [15]. In general, the results of our experiment agree with the literature values within 2σ for the ground state, but the agreement is less clear for the first excited state.

One possible explanation for the incompatibility between the $1/2^-$ spectroscopic factor found in this experiment and the larger value reported by Gaudefroy et al. [16] is the presence of a nearby $5/2^-$ state. This state was first observed by Bhattacharyya et al. [6] at 1234(4) keV, only 34(7) keV above the energy of 1200(6) keV they observed for the $1/2^-$ state, and it was later seen by Gade et al. [15] at 1231(4) keV. This state was not known to Gaudefroy et al. [16], and with their experimental resolution of 75 keV for the $1/2^-$ state, they would not have been able to separate this $5/2^-$ state from the $1/2^-$ state. Thus, we should expect that their spectroscopic factor for the $1/2^-$ state will be larger than the true value since their $1/2^-$ peak also includes contributions from transfer into the $5/2^-$ state. The $5/2^-$ state should not contribute to the value of the spectroscopic factor of the $1/2^-$ state observed in our experiment, however, since the probability of populating this $5/2^-$ state in a (p, p') reaction is negligible compared to the probability in a (d, p) reaction.

An interesting consequence of a smaller spectroscopic factor for the $1/2^-$ state is its possible effect on the single-particle energies. As discussed in Section 1.1.2, the single-particle energies are calculated from a weighted sum of the experimental energy levels where the weights are the spectroscopic factors. Thus, if the spectroscopic factor for the $1/2^-$ state is substantially smaller than the value found by Gaudefroy et al. [16], then the $2p_{1/2}$ single-particle energy must be larger than the value they reported since it will have

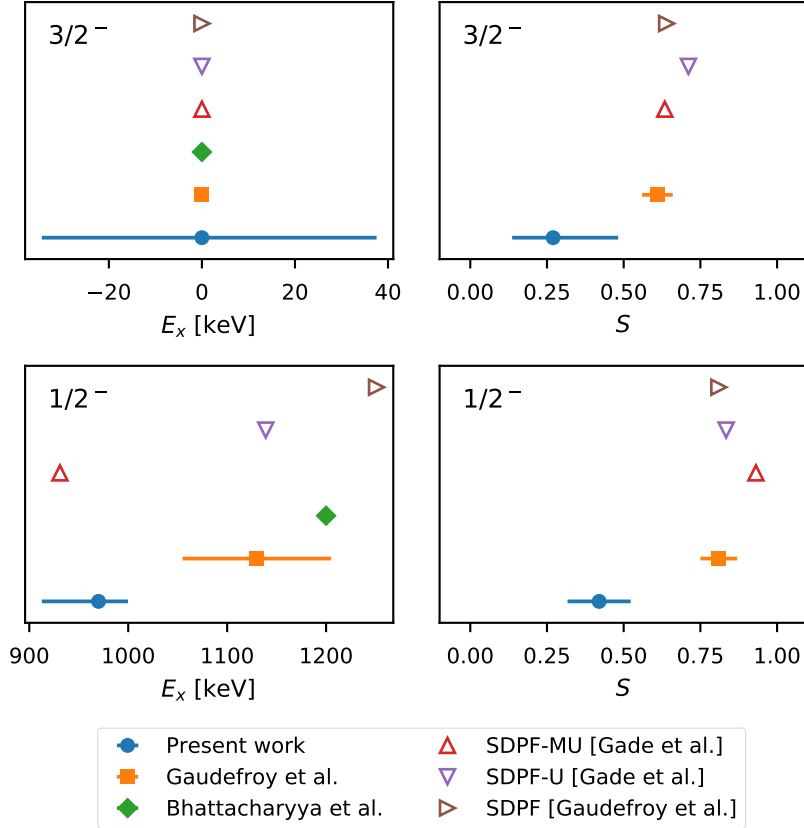


Figure 5.28: Comparison between experimental results and literature values. Filled shapes indicate experimentally measured values, while empty shapes indicate shell model calculations.

Source	$E_x(3/2^-)$	$S(3/2^-)$	$E_x(1/2^-)$	$S(1/2^-)$
Gaudemfroy et al. [16]	0	0.61(5)	1130(75)	0.81(6)
Bhattacharyya et al. [6]	0	—	1200(6)	—
SPDF [18]	0	0.64	1251	0.81
SPDF-U [15]	0	0.711	1139	0.834
SPDF-MU [15]	0	0.634	931	0.861

Table 5.7: Literature values of the measured excitation energies and spectroscopic factors. The SDPF, SDPF-U, and SDPF-MU values are from shell model calculations performed by the authors of the referenced papers.

a smaller contribution from this lowest-lying $1/2^-$ state and, therefore, a larger relative contribution from higher-energy $1/2^-$ states. If this single-particle energy rises without a change in the $2p_{3/2}$ single-particle energy, then the spin-orbit splitting of the $2p$ states will increase.

Finally, the excitation energies reconstructed using the literature values of ΔE_C and S_n , shown as $E_{\text{Ar}}^{\text{CM}}$ in Table 5.2, are systematically lower than expected. The values in the column E_x , calculated by taking the resonance energy corresponding to the ground state as the value of $\Delta E_C - S_n$, appear to be much more realistic. This may indicate that the Coulomb shift calculated by Wang et al. [55] was larger than the true value, which has not yet been measured experimentally.

5.4.2 Statistical significance

Of the four resonances described above, the only one that is statistically significant at the 10 % level is the $1/2^-$ resonance corresponding to the first excited state of the ^{47}Ar nucleus. This resonance was the most likely to be observed since, as a $J = 1/2$ state, it is expected to be broad compared to the higher- J resonances. The identification of the structure around 2.680 MeV/u as the ground state resonance is more tenuous, however, since this structure was not found to be statistically significant. Finally, there appear to be two $1/2^+$ resonances at $E_{\text{res}}^{\text{CM}} = 2.990 \text{ MeV/u}$ and 3.280 MeV/u , which correspond to center-of-mass frame excitation energies of 0.310 MeV/u and 0.600 MeV/u in ^{47}Ar . These do not match any currently known levels in ^{47}Ar . That being said, there is a $1/2^+$ state in ^{41}Ar at $E_{\text{CM}} = 1.88 \text{ MeV/u}$ [47], and one was also found in ^{45}Ar at 1.750 MeV/u [33], although these energies are substantially higher than the energies reported above. Thus, it may be possible that these resonances correspond to previously unobserved $1/2^+$ states in ^{47}Ar that were not accessible in the previous (d, p) measurements. These states would also be difficult to generate in a shell model calculation as it would require a valence space containing the full sd and pf shells for both protons and neutrons, which would be very computationally intensive. Alternatively, these resonances could also correspond to $T_<$ states in the compound nucleus, in which case the true spectroscopic factors should be reduced by a factor of $2T_0 + 1 = 11$ with respect to the values reported in Table 5.2, which assumed a $T_>$ state.

A natural question about these results would be why the ground state resonance was not clearly observed when the first excited state resonance was observed at a statistically significant level. There are a few possible explanations for this. First, the ground state resonance is expected to be quite narrow as it

corresponds to a $3/2^-$ state. The DSIGMAIV calculation predicted that this resonance should have a total width of $15(10)$ keV, which is smaller than the energy binning used above and much smaller than the FWHM energy resolution of the detector, which was found to be 46.4 keV/u in Section 5.3.8. This implies that the resonance would be visible in at most 1-2 bins. Second, previous measurements using single-neutron transfer reactions [15, 16] have found that the spectroscopic factor for transfer into the ground state is approximately 20 % smaller than for transfer into the first excited state. This implies that the ground state resonance should have a smaller amplitude than the resonance corresponding to the first excited state, which is already small. That being said, the results described above suggest that with better statistics and the improved resolution that would be possible if the beam track could be reconstructed, the ground state resonance should be observable with the AT-TPC.

CHAPTER 6

CONCLUSION

6.1 Summary

Studies of nuclei near the $N = 28$ shell closure can provide new insights into the structure of exotic nuclei and the evolution of the shell model far from stability. To this end, an experiment was performed at the National Superconducting Cyclotron Laboratory (NSCL) to measure resonant proton scattering on ^{46}Ar , an $N = 28$ nucleus. This measurement was performed using the Active-Target Time Projection Chamber (AT-TPC), a new detector built at the NSCL for experiments with low-energy, low-intensity radioactive beams.

Since the AT-TPC outputs uncalibrated three-dimensional particle tracks for each recorded reaction, a track reconstruction and analysis method had to be devised for this data. As described in Chapter 3, the data were calibrated with simple linear transformations and then processed with an algorithm based on the Hough transform to remove noise. Finally, a Monte Carlo algorithm was used to fit the tracks with a model that includes contributions from the Lorentz force and the loss of energy to the gas that fills the detector's active volume. The location of each reaction vertex was determined by this fit, and the vertex locations were combined with energy loss information to reconstruct the ^{46}Ar vertex energy for each scattering event. This energy and the scattering angle determined by the fit were then used to produce excitation functions.

After normalizing the excitation functions to units of cross section, they were compared to a simulation done with the R matrix code DSIGMAIV. The cross sections were of approximately the same order of magnitude as the data, but the shapes of the distributions did not match well. We determined that this was due to shortcomings in the simulation of the detector's acceptance, so another analysis method was devised (Section 5.3.10). This analysis revealed four possible resonances in the excitation function, one of which was statistically significant. The significant resonance corresponded to the first excited $1/2^-$ state in ^{47}Ar , and the other three resonances corresponded to the ground state of ^{47}Ar and two $1/2^+$ states that are either previously unobserved levels in ^{47}Ar or $T_<$ states in the compound nucleus.

6.2 Future outlook

As would be expected in a commissioning experiment, this measurement exposed a large and varied collection of hardware problems, software bugs, analysis complications, and oversights in experimental design that will need to be addressed in the future. Fortunately, many of these problems have already been fixed or are in the process of being addressed.

Several of the largest problems we encountered in this experiment were caused by the large dynamic range needed to resolve tracks left by both the heavy, highly ionizing ^{46}Ar beam particle and the light scattered protons with $Z = 1$. To see the proton tracks, a large potential difference had to be applied between the Micromegas mesh and the pads. This greatly over-amplified the beam tracks, causing an unexpected saturation effect in the electronics that rendered these tracks unusable. This also created the large baseline fluctuations described in Section 3.1. In future experiments, these problems will be addressed with a programmable isolation circuit that will replace the simple circuit that is currently installed between the AsAd boards and the sensor plane. This programmable circuit will allow individual pads to be biased to either a high or a low voltage, permitting the creation of a low-bias region for the beam tracks. A prototype of this board was recently built and successfully tested, and a full complement of these boards is now in the process of being procured.

Many of our remaining problems were caused by the trigger used during the experiment, which greatly limited the angular and energy acceptance of the detector. This has been addressed in part by creating a simulation of the trigger electronics (Section 4.1.3) that can be used before future experiments to find appropriate trigger settings. In addition, some changes have recently been made to the CoBo firmware to make the multiplicity trigger threshold setting more intuitive. These efforts, combined with the availability of a true global multiplicity trigger from the now-available MuTAnT board, should make triggering much more predictable in future experiments.

In addition to improving the trigger, having the full MuTAnT board fixes the DAQ system alignment issues described in Sections 5.3.1 and 5.3.2. In future experiments, all CoBos will share a synchronized global clock that can also be output to the VME DAQ system, allowing events to be merged much more reliably by time stamp. This will also remove the ± 1 time bucket uncertainty in z caused by the lack of clock synchronization.

The last big problem we faced was the low experimental statistics. Somewhat ironically, one of the

largest limitations on the number of usable events was the high instantaneous beam rate injected into the detector. This caused a substantial proportion ($\geq 30\%$) of events to be rejected due to pileup. This could be addressed by accepting a lower beam rate, if possible. Additionally, the statistics for proton-scattering experiments could be improved by filling the AT-TPC with pure hydrogen gas (H_2) instead of isobutane (C_4H_{10}). This would eliminate the possibility of carbon scattering and increase the density of proton scattering centers by a factor of 5 as compared to the same amount of isobutane gas. To make this feasible even with the lower gain of pure hydrogen gas, a thick-GEM device has recently been simulated, constructed, and installed in AT-TPC just in front of the Micromegas (see [46] for details). This provides an additional degree of amplification that makes experiments in pure hydrogen and helium gas possible.

Notwithstanding the problems we encountered, as a commissioning experiment, this measurement was largely a success. Although the resolution and statistics were not as good as anticipated, isobaric analog resonances were visible in the recorded data, proving the feasibility of performing this type of experiment with the AT-TPC in the future. Having addressed many of the limitations of this experiment, future measurements should proceed much more smoothly and produce high-quality data.

BIBLIOGRAPHY

BIBLIOGRAPHY

- [1] S. Anvar, P. Baron, B. Blank, J. Chavas, E. Delagnes, F. Druillolle, P. Hellmuth, L. Nalpas, J. L. Pedroza, J. Pibernat, E. Pollacco, A. Rebii, and N. Usher, “AGET, the GET front-end ASIC, for the readout of the time projection chambers used in nuclear physic experiments”, IEEE Nucl. Sci. Conf. R., 745–749 (2012) DOI:10.1109/NSSMIC.2011.6154095.
- [2] M. Baranger, “A definition of the single-nucleon potential”, Nucl. Phys. A **149**, 225–240 (1970) DOI:10.1016/0375-9474(70)90692-5.
- [3] P. Baron and E. Delagnes, *AGET, a Front End ASIC for Active Time Projection Chamber: Data Sheet*, 2013.
- [4] S. Beceiro-Novo, T. Ahn, D. Bazin, and W. Mittig, “Active targets for the study of nuclei far from stability”, Prog. Part. Nucl. Phys. **84**, 124–165 (2015) DOI:10.1016/j.ppnp.2015.06.003.
- [5] D. Bertsimas and J. Tsitsiklis, “Simulated annealing”, Stat. Sci. **8**, 10–15 (1993) DOI:10.1214/ss/1177011077.
- [6] S. Bhattacharyya, M. Rejmund, A. Navin, E. Caurier, F. Nowacki, A. Poves, R. Chapman, D. O’Donnell, M. Gelin, A. Hodsdon, X. Liang, W. Mittig, G. Mukherjee, F. Rejmund, M. Rousseau, P. Roussel-Chomaz, K. M. Spohr, and C. Theisen, “Structure of neutron-rich ar isotopes beyond N=28”, Phys. Rev. Lett. **101**, 032501 (2008) DOI:10.1103/PhysRevLett.101.032501.
- [7] E. C. Bilpuch, in Isobaric spin in nuclear physics: proceedings of the conference on isobaric spin in nuclear physics, edited by D. Robson and J. D. Fox (1966), p. 235.
- [8] C. M. Bishop, *Neural networks for pattern recognition* (Clarendon Press, Oxford, 1995).
- [9] B. A. Brown, *Lecture notes in nuclear structure physics*, Private communication, 2011.
- [10] V. Černý, “Thermodynamical approach to the traveling salesman problem: An efficient simulation algorithm”, J. Optimiz. Theory App. **45**, 41–51 (1985) DOI:10.1007/BF00940812.
- [11] P. Descouvemont and D. Baye, “The R-matrix theory”, Rep. Prog. Phys. **73** (2010) DOI:10.1088/0034-4885/73/3/036301.
- [12] Docker, <https://www.docker.com/>.
- [13] R. O. Duda and P. E. Hart, “Use of the Hough transformation to detect lines and curves in pictures.”, Commun. ACM **15** (1972) DOI:10.1145/361237.361242.
- [14] R. Frühwirth, “Application of Kalman filtering to track and vertex fitting”, Nucl. Instrum. Meth. A **262**, 444–450 (1987) DOI:10.1016/0168-9002(87)90887-4.
- [15] A. Gade, J. A. Tostevin, V. Bader, T. Baugher, D. Bazin, J. S. Berryman, B. A. Brown, C. A. Diget, T. Glasmacher, D. J. Hartley, E. Lunderberg, S. R. Stroberg, F. Recchia, A. Ratkiewicz, D. Weisshaar,

- and K. Wimmer, "Single-particle structure at N=29: The structure of ^{47}Ar and first spectroscopy of ^{45}S ", Phys. Rev. C **93**, 054315 (2016) DOI:10.1103/PhysRevC.93.054315.
- [16] L. Gaudefroy, O. Sorlin, D. Beaumel, Y. Blumenfeld, Z. Dombrádi, S. Fortier, S. Franchoo, M. Gélin, J. Gibelin, S. Grévy, F. Hammache, F. Ibrahim, K. W. Kemper, K. L. Kratz, S. M. Lukyanov, C. Monrozeau, L. Nalpas, F. Nowacki, A. N. Ostrowski, T. Otsuka, Y. E. Penionzhkevich, J. Piekarewicz, E. C. Pollacco, P. Roussel-Chomaz, E. Rich, J. A. Scarpaci, M. G. St. Laurent, D. Sohler, M. Stanoiu, T. Suzuki, E. Tryggestad, and D. Verney, "Reduction of the spin-orbit splittings at the N=28 shell closure", Phys. Rev. Lett. **97**, 092501 (2006) DOI:10.1103/PhysRevLett.97.092501.
 - [17] L. Gaudefroy, O. Sorlin, D. Beaumel, Y. Blumenfeld, Z. Dombrádi, S. Fortier, S. Franchoo, M. Gélin, J. Gibelin, S. Grévy, F. Hammache, F. Ibrahim, K. W. Kemper, K. L. Kratz, S. M. Lukyanov, C. Monrozeau, L. Nalpas, F. Nowacki, A. N. Ostrowski, T. Otsuka, Y. E. Penionzhkevich, J. Piekarewicz, E. C. Pollacco, P. Roussel-Chomaz, E. Rich, J. A. Scarpaci, M. G. St. Laurent, D. Sohler, M. Stanoiu, T. Suzuki, E. Tryggestad, and D. Verney, "Gaudefroy et al. Reply", Phys. Rev. Lett. **99**, 099202 (2007) DOI:10.1103/PhysRevLett.99.099202.
 - [18] L. Gaudefroy, O. Sorlin, D. Beaumel, Y. Blumenfeld, Z. Dombrádi, S. Fortier, S. Franchoo, M. Gélin, J. Gibelin, S. Grévy, F. Hammaehe, F. Ibrahim, K. Kemper, K. L. Kratz, S. M. Lukyanov, C. Monrozeau, L. Nalpas, F. Nowacki, A. N. Ostrowski, Y. E. Penionzhkevich, E. Pollacco, P. Roussel-Chomaz, E. Rieh, J. A. Scarpaci, M. G. St Laurent, T. Rauscher, D. Sohler, M. Stanoiu, E. Tryggestad, and D. Verney, "Study of the N = 28 shell closure in the Ar isotopic chain: A SPIRAL experiment for nuclear astrophysics", Eur. Phys. J. A **27**, 309–314 (2006) DOI:10.1140/epja/i2006-08-047-0.
 - [19] Y. Giomataris, P. Rebougeard, J. Robert, and G. Charpak, "MICROMEGAS: a high-granularity position sensitive gaseous detector for high particle flux environments", Nucl. Instrum. Meth. A **376**, 29–35 (1996) DOI:10.1016/0168-9002(96)00175-1.
 - [20] H. L. Harney, "Determination of spectroscopic factors from elastic proton scattering through the isobaric analogue resonances", Nucl. Phys. A **119**, 591–608 (1968) DOI:10.1016/0375-9474(68)90261-3.
 - [21] I. Heinze, "Development of a Hough Transformation Track Finder for Time Projection Chambers", Ph.D. (University of Hamburg, 2013).
 - [22] P. E. Hodgson, *Nuclear reactions and nuclear structure* (Oxford University Press, London, 1971).
 - [23] J. Illingworth and J. Kittler, "The Adaptive Hough Transform", IEEE T. Pattern. Anal. **PAMI-9**, 690–698 (1987) DOI:10.1109/TPAMI.1987.4767964.
 - [24] F. James and M. Roos, "Minuit: A System for Function Minimization and Analysis of the Parameter Errors and Correlations", Comput. Phys. Commun. **10**, 343–367 (1975) DOI:10.1016/0010-4655(75)90039-9.
 - [25] E. Jones, T. Oliphant, P. Peterson, et al., *SciPy: Open source scientific tools for Python*, <http://www.scipy.org>.

- [26] S. Kirkpatrick, C. D. Gelatt Jr., and M. P. Vecchi, “Optimization by Simulated Annealing”, *Science* **220**, 671–680 (1983) DOI:10.1126/science.220.4598.671.
- [27] G. F. Knoll, *Radiation detection and measurement*, 4th ed. (John Wiley & Sons, Hoboken, NJ, 2010).
- [28] T. G. Kolda, R. M. Lewis, and V. Torczon, “Optimization by direct search: New perspectives on some classical and modern methods”, *SIAM Rev.* **45**, 385–482 (2003) DOI:10.1137/S0036144502428893.
- [29] A. J. Koning and J. P. Delaroche, “Local and global nucleon optical models from 1 keV to 200 MeV”, *Nucl. Phys. A* **713**, 231–310 (2003) DOI:10.1016/S0375-9474(02)01321-0.
- [30] R. R. Labbe, *Kalman and Bayesian Filters in Python* (2015), <https://github.com/rablabbe/Kalman-and-Bayesian-Filters-in-Python/tree/360eccb>.
- [31] S. M. Lea, *Mathematics for Physicists* (Brooks/Cole – Thomson Learning, Belmont, CA, 2004).
- [32] T. Lohse and W. Witzeling, “The Time Projection Chamber”, in *Instrumentation in High Energy Physics*, edited by F. Sauli (World Scientific, Singapore, 1992) Chap. 2, pp. 82–156.
- [33] F. Lu, J. Lee, M. B. Tsang, D. Bazin, D. Coupland, V. Henzl, D. Henzlova, M. Kilburn, W. G. Lynch, A. M. Rogers, A. Sanetullaev, Z. Y. Sun, M. Youngs, R. J. Charity, L. G. Sobotka, M. Famiano, S. Hudan, M. Horoi, and Y. L. Ye, “Neutron-hole states in ^{45}Ar from $^1\text{H}(^{46}\text{Ar}, \text{d})^{45}\text{Ar}$ reactions”, *Phys. Rev. C* **88**, 017604 (2013) DOI:10.1103/PhysRevC.88.017604.
- [34] F. Marti, P. Miller, D. Poe, M. Steiner, J. Stetson, and X. Wu, “Commissioning of the Coupled Cyclotron Facility at NSCL”, in *Cyclotrons and Their Applications 2001*, Sixteenth International Conference (2001).
- [35] K. I. M. McKinnon, “Convergence of the Nelder–Mead Simplex Method to a Nonstationary Point”, *SIAM J. Optimiz.* **9**, 148–158 (1998) DOI:10.1137/S1052623496303482.
- [36] D. J. Morrissey, B. M. Sherrill, M. Steiner, A. Stoltz, and I. Wiedenhoever, “Commissioning the A1900 projectile fragment separator”, *Nucl. Instrum. Meth. B* **204**, 90–96 (2003) DOI:10.1016/S0168-583X(02)01895-5.
- [37] K. P. Murphy, *Machine learning: a probabilistic perspective* (MIT Press, Cambridge, MA, 2012).
- [38] National Nuclear Data Center, *NuDat 2 database*, <http://www.nndc.bnl.gov/nudat2/>.
- [39] J. A. Nelder and R. Mead, “A simplex method for function minimization”, *Comput. J.* **7**, 308–313 (1965) DOI:10.1093/comjnl/7.4.308.
- [40] F. Nowacki and A. Poves, “New effective interaction for $0\hbar\omega$ shell-model calculations in the $sd - pf$ valence space”, *Phys. Rev. C* **79**, 014310 (2009) DOI:10.1103/PhysRevC.79.014310.
- [41] S. Nummela, P. Baumann, E. Caurier, P. Dessagne, A. Jokinen, A. Knipper, G. Le Scornet, C. Miehé, F. Nowacki, M. Oinonen, Z. Radivojevic, M. Ramdhane, G. Walter, and J. Äystö, “Spectroscopy of

- $^{34,35}\text{Si}$ by β decay: $sd - fp$ shell gap and single-particle states”, Phys. Rev. C **63**, 044316 (2001) DOI:10.1103/PhysRevC.63.044316.
- [42] D. R. Nygren, “The Time Projection Chamber — A New 4pi Detector for Charged Particles”, in Proceedings of the 1974 pep summer study (1974), pp. 58–78, <http://lss.fnal.gov/conf/C740805/p58.pdf>.
 - [43] F. Pedregosa, G. Varoquaux, A. Gramfort, V. Michel, B. Thirion, O. Grisel, M. Blondel, P. Prettenhofer, R. Weiss, V. Dubourg, J. Vanderplas, A. Passos, D. Cournapeau, M. Brucher, M. Perrot, and E. Duchesnay, “Scikit-learn: machine learning in Python”, J. Mach. Learn. Res. **12**, 2825–2830 (2011).
 - [44] E. Pollacco, S. Anvar, H. Baba, P. Baron, D. Bazin, C. Belkhiria, B. Blank, J. Chavas, P. Chomaz, E. Delagnes, F. Druillole, P. Hellmuth, C. Huss, E. Galyaev, B. Lynch, W. Mittig, T. Murakami, L. Nalpas, J.-L. Pedroza, R. Raabe, J. Pibernat, B. Raine, A. Rebii, A. Taketani, F. Saillant, D. Suzuki, N. Usher, and G. Wittwer, “GET: A Generic Electronic System for TPCs for Nuclear Physics Experiments”, Phys. Procedia **37**, 1799–1804 (2012) DOI:10.1016/j.phpro.2012.02.506.
 - [45] J. Reiter and H. L. Harney, “Isospin mixing matrix elements extracted from isobaric analog resonances”, Z. Phys. A Atom. Nucl. **337**, 121–129 (1990) DOI:10.1007/BF01294282.
 - [46] S. H. Rost, “Development of THGEM based detectors for AT-TPC applications”, M.S. (Michigan State University, 2016).
 - [47] H. L. Scott, W. Galati, J. L. Weil, and M. T. McEllistrem, “Proton-Induced Reactions on ^{40}Ar and Analogs of ^{41}Ar Levels”, Phys. Rev. **172**, 1139–1148 (1968) DOI:10.1103/PhysRev.172.1139.
 - [48] A. Signoracci and B. A. Brown, “Comment on "reduction of the spin-orbit splittings at the N=28 shell closure"”, Phys. Rev. Lett. **99**, 099201 (2007) DOI:10.1103/PhysRevLett.99.099201.
 - [49] O. Sorlin and M.-G. Porquet, “Evolution of the N = 28 shell closure: a test bench for nuclear forces”, Physica Scripta **T152**, 014003 (2013) DOI:10.1088/0031-8949/2013/T152/014003.
 - [50] D. Suzuki, M. Ford, D. Bazin, W. Mittig, W. Lynch, T. Ahn, S. Aune, E. Galyaev, A. Fritsch, J. Gilbert, F. Montes, A. Shore, J. Yurkon, J. Kolata, J. Browne, A. Howard, A. Roberts, and X. Tang, “Prototype AT-TPC: Toward a new generation active target time projection chamber for radioactive beam experiments”, Nucl. Instrum. Meth. A **691**, 39–54 (2012) DOI:10.1016/j.nima.2012.06.050.
 - [51] I. J. Thompson and F. M. Nunes, *Nuclear reactions for astrophysics: Principles, calculation, and applications of low-energy reactions* (Cambridge University Press, 2009).
 - [52] Y. Utsuno, T. Otsuka, B. A. Brown, M. Honma, T. Mizusaki, and N. Shimizu, “Shape transitions in exotic Si and S isotopes and tensor-force-driven Jahn-Teller effect”, Phys. Rev. C **86**, 051301 (2012) DOI:10.1103/PhysRevC.86.051301.
 - [53] A. C. C. Villari, D. Alt, G. Bollen, D. B. Crisp, M. Ikegami, S. W. Krause, A. Lapierre, S. M. Lidia, D. J. Morrissey, S. Nash, R. J. Rencsok, R. Ringle, S. Schwarz, R. Shane, C. Sumithrarachchi, S. J. Williams, and Q. Zhao, “Commissioning and First Accelerated Beams in the Reaccelerator (ReA3)

- of the National Superconducting Cyclotron Laboratory, MSU”, in Proceedings of IPAC2016 (2016), pp. 4–7, DOI:10.18429/JACoW-IPAC2016-TUPMR024.
- [54] M. Wang, G. Audi, F. G. Kondev, W. Huang, S. Naimi, and X. Xu, “The AME2016 atomic mass evaluation (II). Tables, graphs and references”, Chinese Phys. C **41**, 030003 (2017) DOI:10.1088/1674-1137/41/3/030003.
- [55] Z. Wang, X. Guo, and R. Xu, “Effects of level inversion on the Coulomb displacement energies of the Ar-K isobaric analog state pairs”, (2016), <http://arxiv.org/abs/1605.08171>.
- [56] G. Welch and G. Bishop, *An Introduction to the Kalman Filter*, tech. rep. (University of North Carolina at Chapel Hill, Chapel Hill, NC, 2006), http://www.cs.unc.edu/~welch/media/pdf/kalman_intro.pdf.
- [57] J. F. Ziegler, M. D. Ziegler, and J. P. Biersack, “SRIM - The stopping and range of ions in matter (2010)”, Nucl. Instrum. Meth. B. **268**, 1818–1823 (2010) DOI:10.1016/j.nimb.2010.02.091.